



Universität Stuttgart

# Collective excitations and order parameter dynamics in quantum materials

Von der Fakultät Mathematik und Physik der Universität Stuttgart zur  
Erlangung der Würde eines Doktors der Naturwissenschaften (Dr. rer. nat.)  
genehmigte Abhandlung

Vorgelegt von  
Min-Jae Kim  
aus Seoul, Südkorea

<b>Hauptberichter:</b>	Prof. Dr. Stefan Kaiser
<b>Mitberichter:</b>	Prof. Dr. Tilman Pfau
<b>Prüfungsvorsizender:</b>	Prof. Dr. Maria Daghofer

**Tag der mündlichen Prüfung:** 17. 02. 2022

4. Physikalisches Institut der Universität Stuttgart  
Max-Planck-Institut für Festkörperforschung

2022



# CONTENTS

Zusammenfassung	7
Abstract	9
Introduction	13
1. Higgs mode in superconductors	19
1.1. Higgs in physics . . . . .	19
1.2. Collective modes in superconductors . . . . .	20
1.2.1. Ginzburg-Landau phenomenological model . . . . .	21
1.2.2. Anderson-Higgs mechanism . . . . .	24
1.2.3. Anderson-pseudospin formalism . . . . .	26
1.3. Observation of the Higgs mode . . . . .	31
1.3.1. Higgs mode with CDW . . . . .	31
1.3.2. Nonadiabatic quench with a single-cycle terahertz pump pulse . . . . .	33
1.3.3. Multicycle terahertz driving with subgap frequency and third harmonic generation . . . . .	36
1.3.4. Higgs mode in $d$ -wave superconductor . . . . .	39

2.	Terahertz third harmonic generation in cuprate superconductors	43
2.1.	Third harmonic response of <i>d</i> -wave superconductors . . . . .	44
2.2.	Temperature dependence of third harmonic response . . . . .	46
2.3.	Phase evolution of third harmonics below $T_c$ . . . . .	49
2.4.	Discussion . . . . .	51
2.5.	Summary . . . . .	55
3.	Light-induced Higgs mode response in cuprate superconductors	57
3.1.	Introduction to photoexcited transient superconductivity . . .	57
3.2.	Photoexcited dynamics of terahertz third harmonic generation	64
3.2.1.	Excitation density and temperature dependence of the transient response of third harmonics . . . . .	67
3.2.2.	Light-induced quantum beats . . . . .	72
3.2.3.	Photoexcited third harmonic susceptibility response .	75
3.2.4.	Summary . . . . .	77
4.	Introduction to the excitonic insulator	79
4.1.	Excitons . . . . .	79
4.2.	Excitonic insulator . . . . .	81
4.3.	Realization of potential excitonic insulators in the solid state	85
4.4.	Promising excitonic insulator candidate : $Ta_2NiSe_5$ . . . . .	88
4.4.1.	Clues of excitonic insulator phase in $Ta_2NiSe_5$ . . . . .	91
4.4.2.	Proof of excitonic insulator phase in $Ta_2NiSe_5$ . . . . .	95
4.4.3.	Remaining questions . . . . .	98
5.	Raman spectroscopy of $Ta_2NiSe_5$	99
5.1.	$A_g$ and $B_{2g}$ low frequency modes and electronic background .	102
5.2.	Characterization of the Raman spectra . . . . .	104
5.3.	Summary . . . . .	110
6.	Collective excitations of exciton-lattice coupling in $Ta_2NiSe_5$	113
6.1.	Phononic response of the polaronic complex . . . . .	114
6.2.	Excitonic gap dynamics . . . . .	117
6.3.	Electronic response of the polaronic complex . . . . .	123

6.4. Discussion . . . . .	125
Conclusions	129
A. Experimental Methods	135
A.1. Experimental setup for THz-driven third harmonic generation	135
A.2. Experimental setup for the optical pump-THz drive measurement . . . . .	137
A.3. Sample preparation of Ta <sub>2</sub> NiSe <sub>5</sub> . . . . .	139
A.4. Raman spectroscopy of Ta <sub>2</sub> NiSe <sub>5</sub> . . . . .	140
A.5. Near-infrared pump-probe experiment . . . . .	141
A.6. Time- and angle- resolved photoemission experiment . . . . .	142
A.7. Time-domain THz spectroscopy . . . . .	143
Bibliography	145
List of Figures	169
Acknowledgements	175



# ZUSAMMENFASSUNG

Wenn ein physikalisches System in einen spontanen (kontinuierlichen) symmetriebrochenen Zustand eintritt, treten zwei orthogonale kollektive Moden als Ordnungsparameter-Oszillationen auf: die Amplituden- und die Phasenmode. Bei Supraleitern ist die Amplitudenmode die so genannte Higgs-Mode, da sie das Analogon des Higgs-Bosons in der Teilchenphysik ist, das in kondensierter Materie vorkommt. Es ist jedoch schwierig, diese Mode mit typischen spektroskopischen Instrumenten zu beobachten oder sie mit klassischen theoretischen Berechnungen zu simulieren. Dank der rasanten Entwicklung der ultraschnellen Spektroskopie in den letzten Jahrzehnten ist es möglich geworden, kollektive Phänomene durch Licht zu kontrollieren und neue vielversprechende Funktionalitäten in lichtgesteuerten Quantenmaterialien zu erzeugen. Ziel dieser Arbeit ist die Entdeckung des Higgs-Mode in Hoch- $T_c$ -Kuprat-Supraleitern. Ich charakterisiere seine Auswirkungen auf den supraleitenden Grundzustand sowie seine Eigenschaften in lichtgesteuerten Zuständen. Dazu verwende ich intensive Terahertz-Pulse, deren Energie geringer ist als die supraleitende Lücke, um die Supraleiter in einen stark nichtlinearen Zustand zu versetzen, ohne das Kondensat zu brechen. Das Ergebnis ist die Beobachtung einer stark gedämpften Higgs-Mode und eines universellen Phasensprungs der angetriebenen Higgs-Oszillation in Kuprat-Supraleitern. Dies deutet auf eine externe Kopplung von Ordnungen an die

Higgs-Mode hin.

Außerdem präsentiere ich Hinweise auf eine nicht verschwindende Paarungsamplitude oberhalb von  $T_c$ . Dies macht die Beobachtung der Higgs-Mode zu einem spektroskopischen Werkzeug, das eine neue Art der Higgs-Spektroskopie ermöglicht. Für dynamische Studien von lichtgesteuerten Zuständen, die die Higgs-Oszillationen als Sonden nutzen, zeige ich ihre transienten Eigenschaften unter Photodotierung, die die Supraleitfähigkeit schmilzt. Die daraus resultierende ultraschnelle Dynamik der Higgs-Mode zeigt paarbrechendes Verhalten, das auf eine Paarungsamplitudenantwort hinweist. Darüber hinaus wird die nichtlineare Interferenz der Pump-Photonen mit der Higgs-Mode sichtbar. Diese Studie demonstriert die Möglichkeit, die Higgs-Spektroskopie zu einer transienten Higgs-Spektroskopie von lichtgetriebenen und lichtinduzierten Zuständen zu erweitern.

Über das klassische Gebiet der Higgs-Spektroskopie in Supraleitern hinausgehend, untersuche ich auch kollektive Anregungen von  $\text{Ta}_2\text{NiSe}_5$ , einem gut charakterisierten exzitonischen Isolator Kandidaten mit einer Übergangstemperatur nahe der Raumtemperatur ( $T_c = 328 \text{ K}$ ). Ein exzitonischer Isolator ist eine kohärente elektronische Phase, die durch die Bildung eines makroskopischen Kondensats aus gebundenen Teilchen-Loch-Paaren, so genannten Exzitonen, entsteht. Die Kondensation von Exzitonen in einem Festkörper hat sich als schwer fassbarer Zustand erwiesen, der aufgrund eines gleichzeitigen strukturellen Phasenübergangs im Kandidatenmaterial viele kontroverse Ansichten hervorruft. Hier stelle ich eine entscheidende Phononmode vor, die mit Hilfe der Raman-Spektroskopie auf ein Zusammenspiel von Exzitonen- und Gitterdynamik hinweist. Mit Hilfe von ultraschnellen Experimenten entwirre ich diese Dynamik. Durch die Untersuchung von Gitter- und elektronischen Freiheitsgraden sowie von kohärenten Stromantworten unter Photoanregung zeichne ich ein Bild eines Exziton-Polaron-Komplexes, der die Dynamik der Exzitonenkondensation in  $\text{Ta}_2\text{NiSe}_5$  definiert und viele kontroverse und "widersprüchliche" experimentelle Berichte in der jüngsten Literatur auflöst.

# ABSTRACT

When a physical system enters the spontaneous (continuous) symmetry broken state, two orthogonal collective modes emerge as order parameter oscillations: the amplitude and the phase modes. For superconductors, the amplitude mode is the so called Higgs mode as it is the condensed-matter analog of a Higgs boson in particle physics. But the mode is challenging to observe intrinsically with typical spectroscopic tools as well as it is hard to simulate it by classical calculations theoretically. Due to the rapid development of ultrafast spectroscopy over the last decades, it has become possible to control collective phenomena by light and to induce novel promising functionalities in light controlled quantum materials. This thesis aims to reveal the Higgs mode in high- $T_c$  cuprate superconductors. I characterize its implications for the superconducting ground state as well as its properties in light-driven states. To do so, I use intense terahertz pulses where the energy is lower than the superconducting gap to drive the superconductors into a highly nonlinear regime without breaking the condensate. This results in the observation of a heavily damped Higgs mode and a universal jump in the phase of the driven Higgs oscillation in cuprate superconductors. That points to an external coupling of orders to the Higgs mode.

Further, I present hints for a non-vanishing pairing amplitude above  $T_c$ . This makes the observation of the Higgs mode a spectroscopic tool allowing

for a new type of Higgs Spectroscopy. For dynamical studies of light-driven states using the Higgs oscillations as probes, I show its transient properties under photodoping that melts superconductivity. The resulting ultrafast dynamics of the Higgs mode show pair-breaking behavior pointing towards a pairing amplitude response. Additionally, it reveals the nonlinear interference of the pump photons with the Higgs mode. This study demonstrates the possibility of extending the Higgs spectroscopy into a transient Higgs spectroscopy of light-driven and light-induced states.

Going beyond the classical field of Higgs spectroscopy in superconductors, I also study collective excitations of  $\text{Ta}_2\text{NiSe}_5$ , a well characterized excitonic insulator candidate with a transition temperature near room temperature ( $T_c = 328$  K). An excitonic insulator is a coherent electronic phase that results from the formation of a macroscopic condensate of bound particle-hole pairs, so called excitons. The condensation of excitons in a solid-state has proven to be an elusive state with many controversial views due to a simultaneous structural phase transition in the candidate material. Here I present a crucial phonon mode that points to an interplay of exciton and lattice dynamics by means of Raman spectroscopy. I disentangle its dynamics using ultrafast experiments. By probing lattice and electronic degrees of freedom as well as coherent current responses under photoexcitation I draw a picture of an exciton-polaron complex that defines the dynamics of the exciton condensation in  $\text{Ta}_2\text{NiSe}_5$  and that solves many controversial and “contradicting” experimental reports in the recent literature.

## List of Abbreviations

<b>1D</b>	one-dimensional
<b>2D</b>	two-dimensional
<b>ac</b>	Alternating current
<b>ARPES</b>	angle-resolved photoemission spectroscopy
<b>BCS</b>	Bardeen-Cooper-Schriffer
<b>BEC</b>	Bose-Einstein condensation
<b>CB</b>	conduction band
<b>CDW</b>	charge-density wave
<b>dc</b>	Direct current
<b>EDC</b>	electronic distribution curve
<b>EM</b>	electromagnetic

<b>FFT</b>	fast Fourier transform
<b>fs</b>	femto second
<b>IR</b>	Infrared
<b>NG</b>	Nambu-Goldstone
<b>ps</b>	pico second
<b>SSB</b>	Spontaneous symmetry breaking
<b>T<sub>c</sub></b>	transition temperature or critical temperature in superconductor
<b>THz</b>	terahertz
<b>TH</b>	third harmonic
<b>trARPES</b>	time- and angle- resolved photoemission spectroscopy
<b>UV</b>	Ultraviolet
<b>VB</b>	valence band
<b>ZnTe</b>	Zince Telluride

## Nomenclature

$c$	speed of light in vacuum
$h$	Plank constant
$k_B$	Boltzmann constant

# INTRODUCTION

In the field of condensed matter, the macroscopic properties of matter can go beyond the sum of their single particle properties. Thus they show exotic many-body effects that lead to emergent phenomena. These effects are due to quantum mechanical effects. Here, superconductivity is the most prominent example: In the presence of a strong Coulomb interaction formerly free electrons couple to so called Cooper pair that form a condensate. This process is successfully understood by the concept of quasiparticle which describes the crucial low-energy eigenstates of interacting particles being "dressed" or renormalized. The dressed electrons in a superconductor are such quasiparticles that then form Cooper pairs. The mechanism of pairing is well understood in conventional superconductors by the Bardeen-Cooper-Schrieffer (BCS) theory. The pairing glue in that case is mediated by phonons [1, 2, 3].

However, in many unconventional systems, in particular high temperature superconductivity in cuprates, the pairing mechanism remains an open question. Interacting electron systems subject to cooling may develop a long-range ordered state below a critical transition temperature  $T_c$ . To discuss a condensate, the concept of spontaneous symmetry breaking (SSB) is powerful [4]. In this idea a condensed phase has a lower symmetry than its uncondensed counterpart and is measured by an order parameter.

Identifying a suitable order parameter reflects the underlying symmetry of the system. The order parameter has a nonzero value below  $T_c$ , indicating how deep the system is in the symmetry broken phase, and a zero value above  $T_c$ . This value is associated with the broken symmetry of a system, and it is possible to pinpoint the conditions required for that symmetry to manifest.

For superconductors, typically the size of the gap  $|\Delta|$  or the superfluid density  $n_s$  are typical and insightful choices of an order parameter. Therefore measurements of the order parameter dynamics allow characterizing the nature of the phase transition. As an example, a charge-density-wave (CDW) system is a collective ground state coupling lattice distortions and charge ordering in a linear way. A direct measure of the order parameter of the CDW phase would describe the mapping of the folded band structure and allows to study the interaction of the electronic system with lattice degrees of freedom. Likewise, probing an order parameter of high- $T_c$  superconductivity is of great interest. Order parameter characteristics of the condensate and its dynamics would hint to the so far unknown pairing mechanism. The order parameter itself contains all quantum information about the condensate while its dynamics reveals external interactions and hints to the formation of the condensate.

However, it is challenging to observe the superconducting order parameter experimentally since it does not couple with typical external probes due to the lack of an electromagnetic dipole moment. Unless there are coupled interactions, e.g. CDWs or resonantly coupled phonons it is not measurable by light and magnetic field. Therefore traditional excitation spectroscopies are not suitable for investigating the Higgs mode, the amplitude mode of superconducting condensates. This methodical problem has recently been overcome using Higgs spectroscopy via ultrashort high-field THz pulses that couple to the quadrupolar moment of the Cooper pairs [5, 6]. It may sound strange that one talks about "Higgs" in condensed matter systems, however the idea of Higgs physics is indeed originated from the study of superconductivity. The Higgs boson arises as an oscillating excitation of the Higgs field, which penetrates the world.

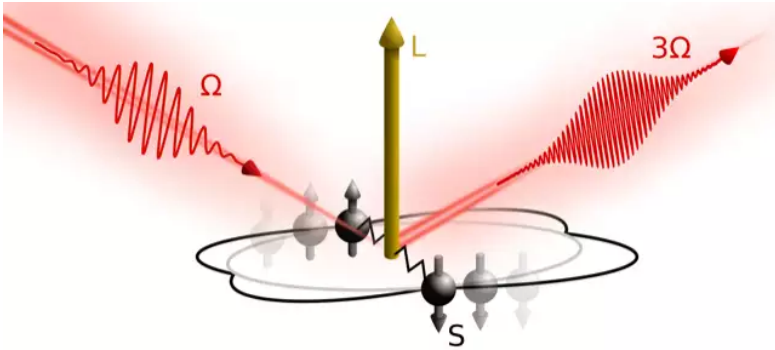


**Figure 0.1.:** The Higgs oscillations excited in a superconductor. Cooper pairs are illustrated in a dumbbell-shaped (grey). The terahertz laser pulse coming from the top left causes the Cooper pairs rotate, namely around the yellow axis with angular momentum  $L$ . It then starts to oscillate within itself as indicated by the zigzag-shaped spring in the diagram at the bottom. These are the actual Higgs oscillations. This superposition leads to characteristic symmetries of vibration, especially in high-temperature superconductors. They emit a signal at three-fold the frequency of the laser. This signal contains complete information about the quantum mechanical state of superconductivity. Figure from [7]. Copyright MPI for Solid State Research.

In analogy to coherent control over Raman-active phonons using ultrashort light pulses that is well established via impulsive stimulated Raman scattering, the Higgs oscillations can be excited by a strong laser pulse. Figure 0.1 shows a very simplified illustration of the Higgs oscillation of a complex Cooper pair that is represented by the dumbbells. The coupled electrons correspond to the weights, and the connection between them is the spring-like handle (zigzag shape in Figure 0.1). They oscillate against or with each other representing the Higgs oscillations. These oscillations then emit a signal that provides the complete information about this collective quantum state and the dynamics of the condensate (like symmetry and frequency of the oscillation and even its angular momentum). This and couplings to these oscillations may help unlock the mystery of the pairing mechanism, particularly the one of high-temperature superconductivity.

To study Higgs mode in high- $T_c$  superconductors, here I am going to show Higgs spectroscopy in cuprate superconductors and map out the Higgs mode properties and its interactions. Further I extend the method of Higgs spectroscopy for transient states of matter using Higgs oscillations as a probe for light-induced dynamics in superconductors. As proof of concept measurement I aim to trace the pair-breaking dynamics under photo-doping a high- $T_c$  cuprate. Further I test the prediction that Higgs spectroscopy may detect other types of condensates. Here I focus on a condensate of excitons, forming a so called excitonic insulator which is one of the intensively studying quantum materials these days.

Excitons are quasiparticles of a bound electron and a hole. Therefore, excitons are bosonic quasiparticles and can potentially form a condensate. This system is very close to a superconductor, but in contrast to Cooper pair, excitons do not have a charge, thus forming an insulator. Also, usually free excitons are not stable in a solid state. The possible excitonic condensation emerges in a system where the binding energy of an exciton  $E_b$  exceeds the energy gap  $E_G$ , due to the unstable insulating ground state against the formation of excitons [8, 9, 10, 11]. The interest in these systems is due to the high densities of electrons and holes in crystals. Their low masses permit the observation of condensate at room temperatures or even higher.

Moreover, the phase transition bears similarities with BCS and Bose-Einstein condensation (BEC). However, probing the condensate state is far more challenging due to the charge neutrality of the exciton. What is missing as experimental fingerprint so far is the obvious macroscopic manifestations of quantum coherence such as dissipationless transport (Meissner effect) as present in a superconductor which is a charged system. Therefore there has been a complete lack of experimental findings pointing to its existence making an excitonic insulator an extremely elusive phase of matter. Since the past 20 years, new and more precise experimental methods allowed for more sophisticated experimental designs to observe “smoking gun” signatures of the exotic phase in optically and transport properties. In order to probe an order parameter of excitonic insulators Higgs spectroscopy would be an ideal tool for investigations of coherent order. To excite the

Higgs mode of the condensate one needs ultrashort light pulse comparable to the excitonic gap size. Thus the excitonic gap requires few-femtosecond laser pulses.

However, so far pure electronic Higgs mode remains to be proven. Instead, recently a hybrid phonon-amplitude Higgs mode [12] and phonon-phase mode [13] were observed in a promising excitonic insulator candidate  $\text{Ta}_2\text{NiSe}_5$ . This material shows an insulating transition above room temperature and does not exhibit any CDW transition as competing orders, making it an ideal material for investigating the excitonic insulating phase. Discussed scenarios are that the lattice seems to stabilize the excitonic coherent even without forming a CDW. Thus the key question to be answered is, if indeed the lattice stabilizes an excitonic state while the phase transition remains excitonic driven, or if the phase transition is simply or partly lattice driven.

To gain insight into these questions, we are going to perform a series of experiments to trace multiple channels. To get the dynamics of the static system, we measure Raman scattering and follow a crucial phonon mode which represents a strong electron-lattice coupling. This coupled state can be assigned to the hybrid Higgs-phonon mode found in earlier measurements probing nonequilibrium-driven states in the material. To disentangle this coupling, I am going to excite coherent phonons to look for the photoexcited phononic response. Then I will study the transient electronic band dynamics and transient conductivity in the terahertz range for the photoexcited electronic response. From this, I try to prove the existence of an exciton-phonon complex that could explain the lattice coupled dynamics of the excitonic condensate.

## **The structure of this thesis**

In this thesis the structure is divided by mainly two quantum materials, high- $T_c$  cuprate superconductors and an excitonic insulator. Chapter 1 introduces the Higgs amplitude mode in superconductors starting from the general question: what is Higgs in condensed matter physics up to the recent observations of the Higgs mode in conventional and unconventional super-

conductors. Chapter 2 describes the characterization of the actively driven Higgs mode performed by intense-THz pulse multicycle drive experiments in cuprate superconductors. Chapter 3 shows the extension of Higgs spectroscopy to experiment with photoexcited superconductivity probing transient Higgs mode. Moving on to the second system, the excitonic insulator, I start to present the basics of exciton formation and potential condensation in a solid state material. Subsequently I introduce the principal material, the potential excitonic insulator  $\text{Ta}_2\text{NiSe}_5$  that may host the elusive state of an excitonic condensate as described in Chapter 4. Chapter 5 presents the result of static Raman spectroscopy that reveals a crucial soft phonon mode that describes a lattice coupled dynamics while Chapter 6 illustrates the nonequilibrium phononic and electronic state of the material in a nonequilibrium driven phase and describes the existence of a polaron-exciton complex as a novel concept. All the experimental methods are described in Appendix.

# HIGGS MODE IN SUPERCONDUCTORS

## 1.1. Higgs in physics

The ‘Higgs’ is well known in particle physics with a Higgs boson which is the source of mass in subatomic particles, making the universe as we know it possible. Experimentally the Higgs boson was captured inside the Large Hadron Collider in Europe and got more fame by announcing the Nobel Prize won by Peter Higgs and Francois Englert in Physics in 2013 [14, 15]. In fact, the Higgs mechanism originated in condensed matter physics.

Anderson and Nambu were among the first physicists to recognize analogies between superconductivity and particle physics [16, 17]. At that time, in early sixties, particle physicists believed that the gauge bosons in Yang-Mills type theories-such as photons in electromagnetism-are necessarily massless. That means massless particles do not correspond to anything we see. Nambu noticed firstly the analogy from the Badeen-Cooper-Schrieffer (BCS) theory of superconductivity to formulate a particle physics model. According to

the BCS model, superconductivity occurs when the ground state of a metal has a lower symmetry than the solid itself (at sufficiently low temperatures), and when the metal is in this state, electrons condense together to form bound states (Cooper pairs). Nambu described that the BCS-like theory could be used to create mass terms for massless elementary particles out of their interactions [18]. These are called "Nambu-Goldstone (NG)" particles. According to the NG theorem, a spontaneous symmetry breaking (SSB) of a continuous symmetry necessitates the emergence of a gapless collective mode, so-called NG mode. For the case of broken translational symmetry, the NG mode is an acoustic phonon and a magnon for spin systems. For superconductors one usually refers to the phase mode or simply the NG mode, a collective mode that quantizes spatial and time fluctuations of the superconducting phase. Anderson suggested in the next year that the NG massless mode can combine with the massless gauge field modes to produce a physical massive vector field [19] as what happens in superconductivity.

Higgs took up Nambu's suggestion and explained how the massless boson is eliminated by the SSB of gauge symmetry, resulting in a massive vector boson and a massive scalar boson which is now known as the Higgs particle. In superconductivity, there is also a possibility of the Higgs particle. It is not an actual particle but an Anderson-Bogoliubov collective mode in the pair channel [20]. As we will see, the case of the superconductor is rather special due to the Anderson-Higgs mechanism. In the superconducting phase, there is an additional mode mode that describes the fluctuation of the amplitude of the superconducting order parameter. This mode is called the Higgs mode. For more detailed discussions on the Higgs boson discovery in high-energy physics and collective Higgs states in superconductors studies, see reviews [21, 22, 23].

## 1.2. Collective modes in superconductors

The observation of the Higgs mode is challenging since it cannot be linearly coupled to the light in a pure superconductor. There was a very first ob-

servation of the Higgs mode in superconductors in  $2H\text{-NbSe}_2$ , a transition metal dichalcogenide in which superconductivity coexists with charge density waves (CDW) [24, 25]. The Higgs mode peak was observed next to the amplitude mode of the CDW by the Raman experiment. Recently, the Higgs mode is expected to couple to the light nonlinearly in a pure superconductor following by Ginzburg-Landau theory and Anderson-Higgs mechanism. This section will introduce the nonlinear light-Higgs coupling in a two-photon process in description and two experimental methods to observe the Higgs mode using a high-field THz pulse.

### 1.2.1. Ginzburg-Landau phenomenological model

An analogy of the superconductivity and Higgs model can be viewed as a relativistic version of the Ginzburg-Landau (GL) theory i.e. a low-energy effective theory of superconductors [26, 27]. The Higgs mode is expected to exist in any system with the spontaneous symmetry breaking (SSB) of the continuous symmetry. In any situation involving second-order phase transitions, some parameter, so-called the order parameter, arises different from zero in the ordered phase and equals zero in the disordered phase (random state). This is a description of the process for SSB, but not an explanation of the underlying causes. There are many examples for SSB, such as the broken translational symmetry in crystals and broken spin rotational symmetry in magnets. Since the transition to a superconducting state is a second order phase transition. The GL model quantifies the phenomena related to superconductivity. For this reason, it does not justify certain choices made within its model, beyond the appeal to consistency and agreement with the experiment. Starting from the general expansion of Landau's free energy about the critical temperature-the lowest order expansion that accommodates the phenomena-in the absence of other interactions, the free energy density can be written as

$$f(\psi) = f_0 + \alpha|\psi|^2 + \frac{\beta}{2}|\psi|^4, \quad (1.1)$$

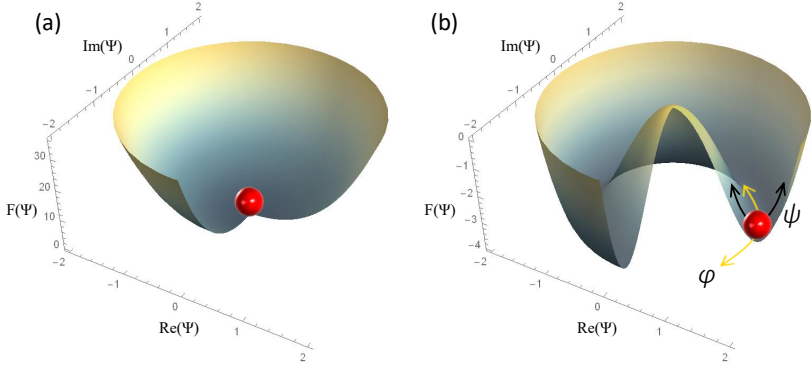


**Figure 1.1.:** An effective potential in the form of a ‘Mexican hat’. (a) Normal state: Continuous symmetry (b) the SSB state. In classical, a ball rolls to a certain point in the potential and selects a direction, with the broken chiral symmetry.

where  $f$  represents the free energy density of a ‘normal’ metal (i.e. the metal in the ‘normal’, as opposed to superconducting state) and  $\alpha$ ,  $\beta$  are phenomenological constants.  $\psi$  is a condensate wave function, representing the collection of superconducting electrons (e.g., as opposed to one or two elementary particles) since the GL model focuses on a collective description of the phenomena. For the theory to be stable, it is required that  $\beta > 0$ . The global  $U(1)$  gauge symmetry means that the free energy is invariant under a constant phase shift  $\psi \rightarrow \psi e^{i\phi(r)}$ . The ground state is extracted by the minimum of the potential as given by

$$|\psi_0| = \begin{cases} 0 & \alpha \geq 0 \\ \sqrt{\frac{-\alpha}{\beta}} & \alpha < 0 \end{cases} \quad (1.2)$$

The upper case indicates the normal state, where the potential has a bowl shape and the ground state is at the origin having the same  $U(1)$  symmetry as the potential (Figure 1.1 (a)). On the other hand, the lower case reveals that  $\Psi = 0$  is not a ground state anymore. Here the free energy is represented by a Mexican hat shaped potential with a circle of new minima of radius  $|\psi_0|$  (Figure 1.1 (b)).

Since the normalized complex field denotes the condensate density,  $|\psi|^2 = n_s$ , it corresponds to the complex order parameter with 0 above  $T_c$  and nonzero below  $T_c$ . The absolute value of the order parameter  $|\psi_0|$ , a radius in the Mexican hat potential, is the size of the gap  $\Delta$  in the system. In this case, the ground state is selected to a definite phase, which can spontaneously be treated as a thermodynamic variable. Now the collective modes are intrinsically driven by quantum fluctuations without any external perturbations. A fluctuation of radial direction with a finite potential energy and tangent direction varying the phase  $\phi$  corresponds to the Higgs amplitude mode (black arrow in Figure 1.1 (b)) and the NG phase mode (yellow arrow in Figure 1.1 (b)), respectively.

As the radial component of the potential directly indicates the gap of the superconducting system, the Higgs mode is regarded as a gapped mode or massive mode with the frequency of  $\omega_H = 2\Delta$  by the microscopic BCS mean-field theory [17, 28, 29, 30, 20, 31]. On the other hand, the NG phase mode is a massless mode since it does not cost energy to vary the overall phase. However, there is an energy penalty for local spatial variations of the phase. This leads to the so-called *phase stiffness* or *rigidity*: the ability of storing energy when an external force induces distortions or winding of the phase. The phase stiffness is responsible for the supercurrent flow in superconductors and superfluidity in  $^3\text{He}$ , described by

$$v_s = \frac{\hbar}{m} \nabla \phi. \quad (1.3)$$

The phase variation, therefore, corresponds to the condensate of the system. It seems very similar between superconductivity and superfluidity, however there is a difference in observing collective modes. A superconductor is a charged system which can couple to a gauge field e.g. an electromagnetic (EM) wave or a magnetic field. The massless phase mode is absorbed into the longitudinal component of the EM field and is lifted to high energy in the scale of the plasma frequency (Anderson-Higgs mechanism). As a result, the Higgs mode becomes stable against decaying to the phase mode in superconductors. Comparably, the Higgs-equivalent amplitude mode in

the Bose-Einstein Condensation e.g.  $^3\text{He}$  system is not observable due to its charge neutrality which prevents coupling to the gauge field. The details are shown in below.

### 1.2.2. Anderson-Higgs mechanism

Now we discuss how we can observe the amplitude mode in the SSB system. The Higgs mode does not couple to the EM field in usual situations, which is why the Higgs mode has not been detected for a long time. The non-linear coupling of Higgs to the light can be understood by the GL theory in a phenomenological point of view. To the general form of the Landau's free energy model of Eq. (1.1), the gauge covariant derivative linking wavefunction  $\psi$  to the EM field is added, using the Schrödinger equation coupled to the EM field [32, 33, 34, 35, 36]. The final form of the free energy density is given by

$$f(\psi) = f_0 + a|\psi(r)|^2 + \frac{b}{2|\psi(r)|^4} + 1/2m^*|(-i\nabla - e^*\mathbf{A})\psi(r)|^2, \quad (1.4)$$

where  $a = a_0(T - T_c)$ ,  $a_0$  and  $b$  are some constants,  $m^*$  and  $e^*$  are a effective mass and an effective charge of the Cooper pair condensate, respectively.  $\mathbf{A}$  is a vector potential that represents the external light field  $\mathbf{E}(t) = -\partial\mathbf{A}(t)/\partial t$ .

The free-energy density of Eq. (1.4) is invariant under the global  $U(1)$  phase rotation  $\psi \rightarrow \psi e^{i\phi(r)}$  and more generally under the gauge transformation  $\psi \rightarrow \psi e^{ie^*\chi(r)}$ , with  $\mathbf{A} \rightarrow \mathbf{A} + \nabla\chi(r)$  for an arbitrary scalar field  $\chi(r)$ . In addition, the GL free-energy density is invariant under particle-hole transformation  $\psi \rightarrow \psi^\dagger(r)$ . The presence of the particle-hole symmetry (including the time derivative terms in action) is crucial for decoupling the Higgs amplitude mode from the NG phase mode [37, 23, 38]. In other words, the Higgs mode appears in a system if the fermion energy dispersion is particle-hole symmetric [37, 39, 38, 40]. If a system violate the particle-hole symmetry for reasons such as intrinsic orders or perturbation from the outside, the amplitude mode starts decaying (Figure 1.2 (a)). In electrically neutral

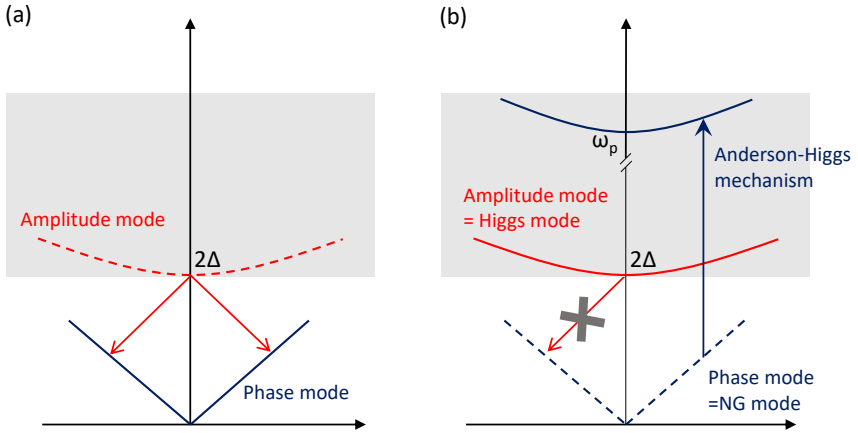


**Figure 1.2.:** A schematic fluctuation spectrum of SSB. (a) Due to the Anderson–Higgs mechanism, the NG mode acquires an energy gap in the order of the plasma frequency  $\omega_p$ , whereas the Higgs mode remains in low energy with an energy gap  $2\Delta$ , above which the quasiparticle excitation continuum overlaps.

systems, such as superfluid ultracold atoms, the amplitude mode rapidly decays into the energetically lower phase mode. Therefore, the phase mode (Bogoliubov mode in  $^3\text{He}$ ) is always stable while the Higgs amplitude mode in the neutral case is not. On the other hand, the Higgs mode is stable in a superconductor. The massless phase mode is coupled to a gauge field in such a charged case. Then the phase mode elevates to the higher energy at the plasma frequency. Therefore, the Higgs amplitude mode cannot decay and is stable even though the particle-hole symmetry is not protected (Figure 1.2 (b)). This is the famous the Anderson-Higgs mechanism [17, 16, 19, 41, 42, 43], that will be described. In particle physics, this mechanism explains the mass generation of the  $W^\pm$  and  $Z$  gauge bosons of the weak interaction and led to the postulation of the Higgs boson in the standard model and the final observation at the LHC in CERN in 2012 [14, 15].

Intuitively when a photon comes into a superconductor, it absorbs a phase mode of the system and reveals the longitudinal component of the field. In this process, the photon vanishes exponentially with a finite penetration

depth in the superconductor. This describes Meissner effect in superconductor: the expulsion of a magnetic field from a superconductor during its transition to the superconducting state when it is cooled below the critical temperature. On the other hand, therefore, the neutral SSB system does not reveal the Meissner effect.

So far, we have discussed the Higgs mode and its resonance with the EM wave based on the time-dependent GL theory Eq. (1.4). However, the characteristic frequency  $\omega_H$  of the Higgs mode cannot be determined within GL theory. As shown in Figure 1.2, the Higgs mode is degenerate with the lower bound of the quasi-particle excitation continuum ( $\omega_H = 2\Delta$ , grey-shaded). Since the Higgs mode lies at the same energy scale as the quasi-particle excitations [31, 44], it can easily decay into individual quasi-particles. Moreover, the quasi-particle excitation lifetime is longer than the time scale of the order-parameter variation in clean superconductors. In other words, one needs to consider the quasi-particle excitations in the dynamics of the order parameter, which is necessarily entangled with those of quasi-particles.

The low-energy effective theory of the Higgs mode does not seem to be expressed only in terms of  $\psi$  but may involve fermionic degrees of freedom [45]. The questions that arise are if the Higgs resonance discussed here would still survive or not after the relaxation to quasi-particles (pair-breaking process), and if it survives, then how we can distinguish the collective Higgs mode from individual quasi-particle excitations, since they are energetically degenerate. To fulfill this question, the Anderson pseudospin formalism are introduced.

### 1.2.3. Anderson-pseudospin formalism

The Anderson pseudospin formalism [17] is a reformulation of the BCS Hamiltonian [3, 2] and gives a microscopic perspective of the Higgs amplitude mode dynamically responding to EM fields. It maps the occupation of Cooper pairs ( $\mathbf{k} \uparrow, -\mathbf{k} \downarrow$ ) to pseudospin states such that an up-spin will provide an intuitive pictorial interpretation of the superconducting state and its excitations, as we will see in the following. We start from the pairing

Hamiltonian for an  $s$ -wave superconductor

$$H = \sum_{k\sigma} \epsilon_k c_{k\sigma}^\dagger c_{k\sigma} - \sum_{kk' \in \mathcal{W}} V_{kk'} c_{k\uparrow}^\dagger c_{-k\downarrow}^\dagger c_{-k'\downarrow} c_{k'\uparrow}, \quad (1.5)$$

where  $\epsilon_k$  is the band dispersion measured from the Fermi energy  $\epsilon_F$ , where  $\epsilon_k = \xi_k - \epsilon_F$  is the electron dispersion  $\xi_k$  measured relatively to the Fermi energy  $\epsilon_F$ . Here, the second sum runs over all  $k$  such that the energy is smaller than some cutoff energy  $\epsilon_c$ , i.e.  $\mathcal{W} = \{\mathbf{k} \mid |\epsilon_k| < \epsilon_c\}$ . The cutoff energy is given by the Debye energy for phonon-mediated superconductivity.  $V_{kk'}$  is the attractive pairing interaction. Since it is difficult to solve correlations in the system arising from interactions between the electrons, one can approximate a model by a non-interacting counterpart to make it easier. One can perform a mean-field approximation

$$c_{k\uparrow}^\dagger c_{-k\downarrow}^\dagger c_{-k'\downarrow} c_{k'\uparrow} \approx \langle c_{k\uparrow}^\dagger c_{-k\downarrow}^\dagger \rangle c_{-k'\downarrow} c_{k'\uparrow} + \langle c_{-k'\downarrow} c_{k'\uparrow} \rangle c_{k\uparrow}^\dagger c_{-k\downarrow}^\dagger + \langle c_{k\uparrow}^\dagger c_{-k\downarrow}^\dagger \rangle \langle c_{-k'\downarrow} c_{k'\uparrow} \rangle, \quad (1.6)$$

where the product of two creation and annihilation operators are replaced by their expectation value. We define the superconducting gap function

$$\Delta_k = \sum_{k'} V_{kk'} \langle c_{-k'\downarrow} c_{k'\uparrow} \rangle \quad (1.7)$$

which serves as the order parameter in the BCS theory. Neglecting the constant term, one obtains the general mean-field BCS Hamiltonian

$$H = \sum_{k\sigma} \epsilon_k c_{k\sigma}^\dagger c_{k\sigma} - \sum_k \Delta_k c_{k\uparrow}^\dagger c_{-k\downarrow}^\dagger - \sum_k \Delta_k^* c_{-k\downarrow} c_{k\uparrow}. \quad (1.8)$$

We will introduce the Nambu-Gorkov basis to transform the BCS Hamiltonian to the matrix form. First, we rewrite the kinetic terms (the first term of Eq. 1.8) of the Hamiltonian. We assume that the dispersion is parity symmetric,

i.e.  $\epsilon_{-k} = \epsilon_k$ , and we find

$$H_{\text{kin}} = \sum_k \epsilon_k \left( c_{k\uparrow}^\dagger c_{k\uparrow} + c_{k\downarrow}^\dagger c_{k\downarrow} \right) = \sum_k \left( \epsilon_k c_{k\uparrow}^\dagger c_{k\uparrow} - \epsilon_k c_{-k\downarrow} c_{-k\downarrow}^\dagger \right). \quad (1.9)$$

With this, the full BCS Hamiltonian reads

$$\begin{aligned} H &= \sum_k \left( \epsilon_k c_{k\uparrow}^\dagger c_{k\uparrow} - \epsilon_k c_{-k\downarrow} c_{-k\downarrow}^\dagger - \Delta_k c_{k\uparrow}^\dagger c_{-k\downarrow}^\dagger - \Delta_k^* c_{-k\downarrow} c_{k\uparrow} \right) \\ &= \sum_k \begin{pmatrix} c_{k\uparrow}^\dagger & c_{-k\downarrow} \end{pmatrix} \begin{pmatrix} \epsilon_k & -\Delta_k \\ -\Delta_k^* & -\epsilon_k \end{pmatrix} \begin{pmatrix} c_{k\uparrow} \\ c_{-k\downarrow}^\dagger \end{pmatrix} \\ &= \sum_k \Psi_k^\dagger \begin{pmatrix} \epsilon_k & -\Delta_k \\ -\Delta_k^* & -\epsilon_k \end{pmatrix} \Psi_k, \end{aligned} \quad (1.10)$$

where we define the Nambu-Gorkov spinor for convenience

$$\Psi_k^\dagger = \left( c_{k\uparrow}^\dagger, c_{-k\downarrow} \right), \quad \Psi_k = \begin{pmatrix} c_{k\uparrow} \\ c_{-k\downarrow}^\dagger \end{pmatrix}. \quad (1.11)$$

We express the matrix with the three terms of the kinetic energy  $\epsilon_k$  and the energy gap is splitted in its real and imaginary part  $\Delta_k = \Delta'_k + i\Delta''_k$ . The matrix can be expressed by the pauli spin matrices,

$$\tau_x \equiv \begin{pmatrix} 0 & 1 \\ 1 & 0 \end{pmatrix} \quad \tau_y \equiv \begin{pmatrix} 0 & -i \\ i & 0 \end{pmatrix} \quad \tau_z \equiv \begin{pmatrix} 1 & 0 \\ 0 & -1 \end{pmatrix}. \quad (1.12)$$

The BCS Hamiltonian turns to

$$\begin{aligned} H &= \sum_k \Psi_k^\dagger \left[ \epsilon_k \begin{pmatrix} 1 & 0 \\ 0 & -1 \end{pmatrix} - \Delta'_k \begin{pmatrix} 0 & 1 \\ 1 & 0 \end{pmatrix} + \Delta''_k \begin{pmatrix} 0 & -i \\ i & 0 \end{pmatrix} \right] \Psi_k \\ &= \sum_k \Psi_k^\dagger \left[ \epsilon_k \tau_z - \Delta'_k \tau_x + \Delta''_k \tau_y \right] \Psi_k. \end{aligned} \quad (1.13)$$

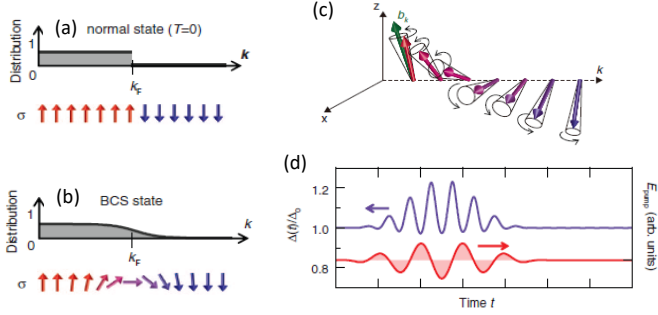


**Figure 1.3.:** Anderson's pseudospin model and simulation with Bloch equation [6]. (a and b) Schematics of the electron distribution represented by Anderson's pseudospins for the normal state at  $T = 0$  and for the BCS state, respectively. (c) A schematic picture of the pseudospin precession. (d) Simulation of the Bloch equation showing the temporal evolution of the order parameter in an electric field. Figure from [6]

Next, we define the Anderson's pseudospin

$$\sigma_k = \frac{1}{2} \Psi_k^\dagger \cdot \tau \cdot \Psi_k. \quad (1.14)$$

The pseudospin satisfies the usual commutation relations for angular momentum,  $[\sigma_k^j, \sigma_k^k] = i \varepsilon_{jkl} \sigma_k^l$ . With this, the pairing Hamiltonian is recast in the form

$$H_{\text{pair}} = 2 \sum_k \mathbf{b}_k \cdot \sigma_k, \quad (1.15)$$

which can be regarded as a spin system in an effective magnetic field

$$\mathbf{b}_k^\top = (-2\Delta'_k, \quad 2\Delta''_k, \quad 2\epsilon_k). \quad (1.16)$$

We can see that the  $z$ -component of the pseudomagnetic field represents the occupation of pair states ( $\mathbf{k} \uparrow, -\mathbf{k} \downarrow$ ) as seen the third term of energy dispersion  $\epsilon_k$ .

At the equilibrium,  $\Delta_k = 0$ , the pseudomagnetic field changes sign at the  $k_F$

with "Down" below  $k_F$  and "Up" above  $k_F$ . The Anderson's pseudospin points to opposite to the pseudomagnetic field to minimize their energy, leading to the pseudospin state of Figure 1.3 (a). In the BCS superconducting state, the pseudomagnetic field acquires a complex order parameter  $\Delta_k = \Delta'_k + \Delta''_k$ , therefore it exhibits smooth pseudospin canting by the rotation through the  $x$ - (and  $y$ - for complex order parameter) plane near  $k = k_F$  as shown in Figure 1.3 (b). Now we add additional time-dependent interaction terms to the Pseudospin Hamiltonian to show a coupling to external fields. We also undergo the time evolution to the pseudospin formalism with the equation of motion

$$\frac{\partial}{\partial t} \sigma_k(t) = \frac{1}{\hbar} b_k(t) \times \sigma_k(t), \quad (1.17)$$

where the pseudomagnetic field  $b_k(t) = (-\Delta'(t), -\Delta''(t), 1/2[\epsilon_{(k+A(t))} + \epsilon_{(k-A(t))}])$  which represents the coupling to the EM field  $\mathbf{A}(t)$ . The coherent collective precession of the pseudospins (Figure 1.3 (c)) manifests itself macroscopically as the order parameter oscillation, and the change of the order parameter in turn affects the pseudomagnetic field. Since the  $z$ -component of the  $b_k$  is well coupled to the EM field we can find the terms of  $\mathbf{A}(t)$  in  $b_k^z$  written as

$$\delta \Delta(t) \propto \frac{1}{|2\omega - 2\Delta|^{1/2}} \cos(2\omega t - \phi) \quad (1.18)$$

with  $\phi$  being a phase shift that depends on  $\omega$ . We can expect the divergence of the amplitude at  $2\omega = 2\Delta$  revealing the resonance of the induced pseudospin precession ( $2\omega$ ) to the collective amplitude mode (Higgs mode) of the order parameter ( $2\Delta$ ). Taken from the London equation the nonlinear current density  $j_{NL}$  can be introduced as

$$j_{NL}(t) \propto \frac{e^2 \Delta}{U} \mathbf{A}(t) \delta \Delta(t) \quad (1.19)$$

where the variation of the order parameter  $\delta \Delta(t)$ ;  $2\omega$  driven by the external ac field  $\mathbf{A}(t)$ . We therefore obtain the third harmonic current ( $3\omega$ ) from the

system. In general, however, the BCS mean field treatment (in the clean limit) as we have described so far suggests that the Higgs-mode contribution to the third harmonic (TH) is subdominant as compared with that of individual quasiparticle excitations. As shown previously (Figure 1.2), the energy scales of the Higgs mode and the quasiparticle pair excitations are degenerated at the same energy range. The competition between the two contributions is complicated. To solve the problem, there is a growing understanding from recent studies, that if one considers effects beyond the BCS mean-field theory in the clean limit, the light-Higgs coupling strength drastically changes. It has been shown that the Higgs mode can contribute to the TH with an order of magnitude comparable to quasiparticles when the calculation includes phonon retardation effects [46, 47, 48, 49, 50]. Another possibility is to depart from the clean limit and consider the effect of disorders or impurity scattering. In the dirty regime the magnitude of the Higgs mode contribution to the TH can exceed by far that of quasiparticles [51, 52, 53, 54, 55]. For more insights accounting for the collective modes in superconductor, see refs [22, 56].

The first experimental fingerprint was observed indirectly by Raman experiments in the superconductor NbSe<sub>2</sub>. It was attributed to the renormalized Higgs mode coupling to the CDW which can easily couple to the light. In the following section, we will overview the recent progress on experimental observations of the Higgs mode in superconductors from a CDW-coexisting superconductors to the nonlinear light-Higgs coupling in a pure *s*-wave superconductor.

## 1.3. Observation of the Higgs mode

### 1.3.1. Higgs mode with CDW

The first observation of the Higgs mode in superconductors was performed by a Raman experiment, in the system of 2H-NbSe<sub>2</sub>, a transition metal dichalcogenide in which superconductivity coexists with CDW. A new peak was observed below  $T_c$  that was distinct from the amplitude mode associated

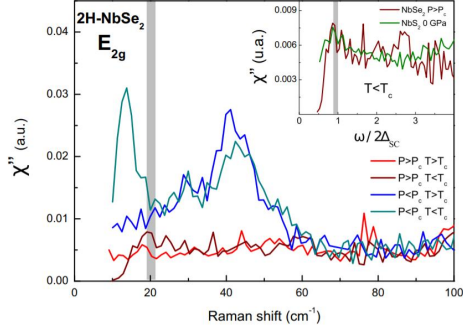


**Figure 1.4.:** Raman spectra in  $E_{2g}$  symmetry of  $2\text{H-NbSe}_2$  measured at various temperatures and pressures. Under the ambient pressure ( $P < P_c$ ) and in the superconducting phase ( $T < T_c$ ) (green), a sharp peak identified as the Higgs mode appears below the superconducting gap  $2\Delta \sim 20\text{cm}^{-1}$  marked by the gray vertical line. In the CDW phase ( $T > T_c$ ) (blue), only the CDW amplitude mode is observed around  $40\text{cm}^{-1}$ . Under the pressure ( $P > P_c$ ) where CDW collapses, only a pair breaking peak is discerned at  $T < T_c$  (brown), and no peak is identified at  $T > T_c$  (red). (Inset) Raman spectra in the superconducting state without CDW in  $2\text{H-NbSe}_2$  (above 4 GPa) and non-CDW-coexisting  $\text{NbS}_2$  (0 GPa), both of which show only the pair breaking peak. Frequency is normalized by  $2\Delta$ . Figure from [57]

with the CDW order [24, 25]. When it was measured for the first time, the new peak was regarded as a pair breaking peak. However it was identified as the collective amplitude mode of the superconducting order (i.e. the Higgs mode) [30, 20].

Recent Raman experiments clearly demonstrated that the spectral weight shift from the CDW amplitude mode (amplitudon) to the superconducting amplitude mode upon entering the superconducting phase [58]. Furthermore, the Raman experiment under hydrostatic pressure revealed that the CDW order is suppressed and concomitantly the Raman peak identified as the Higgs mode disappeared, leaving only the Cooper pair breaking peak [57, 59] (Figure 1.4). These studies indicate that the existence of CDW plays an important role on the observability of the Higgs mode in the Raman

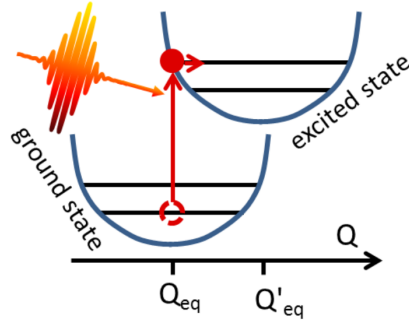


**Figure 1.5.:** Excitation mechanisms for coherent phonons. In a displacive process the laser pulse excites electrons from bands with bonding to bands with antibonding character. In the excited state the equilibrium positions of the atoms are consequently shifted. If this shift occurs on a time scale, which is shorter than phonon's oscillation period, the phonon starts to oscillate. Figure from [61].

spectrum. Theoretically, the coupling of the superconducting order to the coexisting CDW order may result in the Higgs-mode energy pushed down below the superconducting gap  $2\Delta$ .

A long-standing issue is whether the Higgs mode can be observed in superconductors without CDW order. A direct excitation of the Higgs mode has been believed to be possible only in nonequilibrium experiments by the quench dynamics [60]. Thanks to the development of ultrafast pump-probe spectroscopy techniques in the low-energy THz frequency range, one can observe the Higgs amplitude mode oscillations without attaining the CDW order.

### 1.3.2. Nonadiabatic quench with a single-cycle terahertz pump pulse

One way to excite the Higgs mode is a nonadiabatic quench of the superconducting state. It is similar to an impulsive Raman process. This process requires short laser pulses whose lengths are shorter than the timescale defined by the gap of the phonon. Under the photoexcitation, the equilibrium potential position shifts up to the excited state and the lattice energy

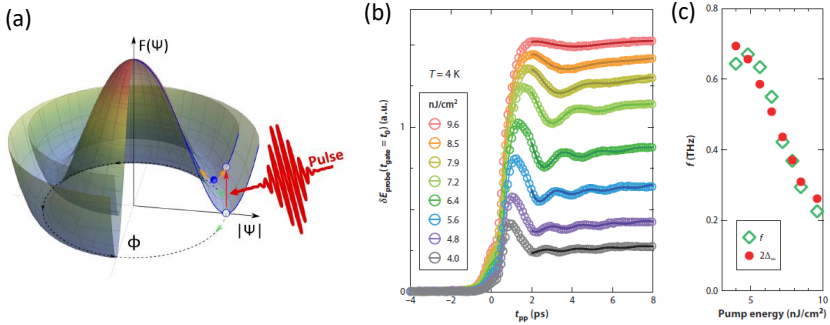


**Figure 1.6.:** The schematic of the Higgs mode excitation and the resulted oscillation of quasiparticles in NbN induced by a monocycle THz pump [5]. (a) A laser pulse changes the free energy landscape nonadiabatically. The order parameter cannot follow if the pulse is much shorter than the period of the Higgs mode (red vertical arrow) and the order parameter therefore starts to oscillate around the new equilibrium position (position of solid blue ball). (b) The temporal evolution of the change of the probe electric field  $\delta E_{\text{probe}}$ , as a function of the pump-probe delay time  $t_{\text{pp}}$  at various pump intensities. The solid curves represent the results fitted by a damped oscillation with a power-law decay. (c) The oscillation frequency  $f$  obtained from the fits and the asymptotic gap energy  $2\Delta_{\infty}$  as a function of the pump intensity. Figure from [5].

becomes higher out of the ground state 1.5. Afterwards, the electronic state starts to oscillate towards the new minimum energy state. Characteristic for this excitation mechanism is a  $\cos(\omega t)$  dependence since the oscillation starts at maximum displacement. The frequency  $\omega$  is equivalent to Raman active phonons. More descriptions about excitation mechanisms for coherent phonons can be found in [62].

Following this mechanism, the Higgs amplitude mode can be observed by the quenching process. When a THz pump arrives at a superconductor it excites quasiparticles and changes the free energy landscape of the system, shrinking the Mexican-hat potential towards zero free energy (the top of the hat) as seen in Figure 1.6 (a). Since the optical pulse length is much shorter than the response time of the amplitude mode, the order parameter cannot

follow immediately and stands out of the lowest energy state. Subsequently, the order parameter rolls down towards the new minimum of the excited landscape and it oscillates with the frequency of the Higgs amplitude mode as described in the following equation [45],

$$\frac{|\Delta(t)|}{\Delta_\infty} \simeq 1 + a \frac{\cos(2\Delta_\infty t + \phi)}{\sqrt{\Delta_\infty t}} \quad (1.20)$$

where  $\Delta$  is the long-time asymptotic superconducting gap,  $a$  is some constant, and  $\phi$  is a phase shift. In principle, the pumping light should not exceed the superconducting gap energy avoiding a full suppression of the order parameter and excitation of other collective modes such as phonons. Therefore, to ensure the nonadiabatic excitation, it is necessary to use a short pump pulse with its photon energy resonant to the BCS gap which is typically located in the THz frequency range [63]. With the recent development of THz technology, such an intense and monocycle-like THz pulse has become available, making it possible to investigate the THz nonlinear response in a variety of materials. With using the intense THz pump-THz probe spectroscopy, the ultrafast pair breaking and the subsequent quasiparticle dynamics can be investigated. The first observation of the Higgs mode excitation was shown in the  $s$ -wave superconductor  $\text{Nb}_{1-x}\text{Ti}_x\text{N}$  [5]. Figure 1.6 (b) exhibits the experimental result of the quenched superconducting order parameter. At the  $t_{\text{pp}}=0$ , THz pump pulse quenches the system nonadiabatically by the quasiparticle injection, resulting in clear oscillations afterwards. The fits of the oscillations show the frequency given by the asymptotic value of the superconducting gap (Figure 1.6 (c)). The study also exhibits the transient optical conductivity, which represents the superfluid density modulations as well, see ref. [5]. One issue we should consider is the decay of the Higgs mode. In the clean limit BCS superconductor it is expected that the Higgs mode has a much longer lifetime than the oscillation period. It is shortened and turns into an overdamped mode due to the energy dispersion of the Higgs mode where the quasiparticle continuum is overlapped. It represents that the Higgs mode oscillates the longest time at small  $q$ . In the following section, another method to observe the higgs mode will be introduced.

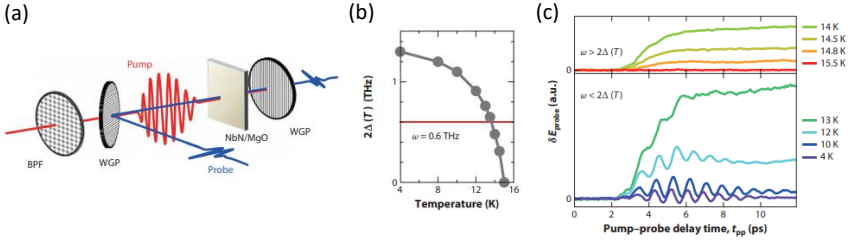


**Figure 1.7.:** Forced Higgs oscillation and third harmonic generation from a superconducting NbN film under the multicycle THz pump. (a) Schematic setup for the multicycle THz pump and THz probe spectroscopy. (b) Temperature dependence of the superconducting gap energy. Horizontal line indicates the center frequency of the pump pulse,  $\omega = 0.6$  THz. (c) The change in the transmitted probe THz electric field  $\delta E_{\text{probe}}$  as a function of the pump-probe delay time  $t_{\text{pp}}$  at the temperature range  $\omega > 2\Delta(T)$  (upper) and  $\omega < 2\Delta(T)$  (lower). Increase of  $\delta E_{\text{probe}}$  corresponds to the reduction of the order parameter. Figure from [6]

### 1.3.3. Multicycle terahertz driving with subgap frequency and third harmonic generation

While the quenches of superconductors showed the intrinsic Higgs oscillations, here driven or enforced Higgs oscillations will be presented. The Anderson-pseudospin formalism (see 1.2.3) shows that the quadratic coupling to the condensate of a multi-cycle light pulse  $A(t)$  with frequency  $\omega$  induces oscillations of the energy gap  $\delta\Delta(t)$  with twice the driving frequency  $2\omega$  (Eq.(1.18)). This nonlinear coupling induces a higher-order current  $j_{NL}$ , where the TH component arises (Eq.(1.19)). If the effective  $2\omega$  driving field is tuned to the energy of the Higgs mode  $2\Delta$  of the system, a resonance occurs in the gap oscillation. The resonance feature indicates the Higgs mode existence. However, in current technologies there is no tunable THz laser available in the required energy range. Therefore, one cannot sweep the driving frequency to apply the resonant energy to the Higgs mode. Instead, experiments are performed with fixed driving frequency. To find the resonance, the energy of the Higgs mode  $2\Delta(T)$  is tuned by varying the temperature  $T$ .

For *s*-wave superconductors, it was shown that driven Higgs oscillations resonate with the energy of the Higgs mode, representing the TH [6]. For a preceded experiment, a multicycle THz pump - single cycle THz probe measurements were performed (Figure 1.7 (a)). The driving field is fixed at 0.6 THz and the energy of the Higgs mode  $2\Delta(T)$  is changed by sweeping the temperature  $T$  (Figure 1.7 (b)). Figure 1.7 (c) shows  $\delta E_{probe}$  with  $t_{pp}$  at  $T = 14$  to 15.5K, at which  $\omega$  is greater than  $2\Delta(T)$ . In this temperature range, the probe electric field gradually increased as a function of  $t_{pp}$  to reach an asymptotic value, which indicates a reduction of the order parameter resulting from quasiparticle excitations [64]. By contrast, at temperatures below 13 K where  $2\Delta(T)$  exceeded the pump THz field  $\omega$ , the long-term reduction of the order parameter became less prominent as temperature decreased, because the quasiparticle excitation is suppressed. They found that an oscillatory signal emerges with a frequency of 1.2 THz ( $= 2\omega$ ) during the pump pulse irradiation, which indicates that the order parameter oscillates with twice the frequency of the driving field. The  $2\omega$  oscillation of the order parameter was physically captured in terms of the precession of Anderson's pseudospins [17].

Now the observation of the resonance between Higgs and the driving field can be realized by the self-transmission measurement with high-field THz multicycle pulse (figure 1.8 (a)). Importantly, the TH was shown to be resonantly enhanced when the condition  $2\omega=2\Delta$  is satisfied as discussed in Eq. (1.18). Below  $T_c$  the TH component is observed by the transmitted subgap THz pulse in the time-domain and frequency-domain respectively (Figure 1.8 (b) and (c)). The intensity at  $3\omega$  as a function of the pump electric field strength, depicted in Figure 1.8 (d) on a log-log scale. The intensity obeys  $|E_{pump}^6|$  dependence, endorsing that the signal arises from the third harmonic generation. TH would be the most intense when the resonant condition  $2\omega = 2\Delta$  is satisfied. The amplitude of the TH shows that it is peaked at the resonant condition as varying the temperature (Figure 1.8 (e)).

In the context of superconductors, it has been theoretically pointed out that not only the Higgs mode but also charge-density fluctuations (CDFs) can

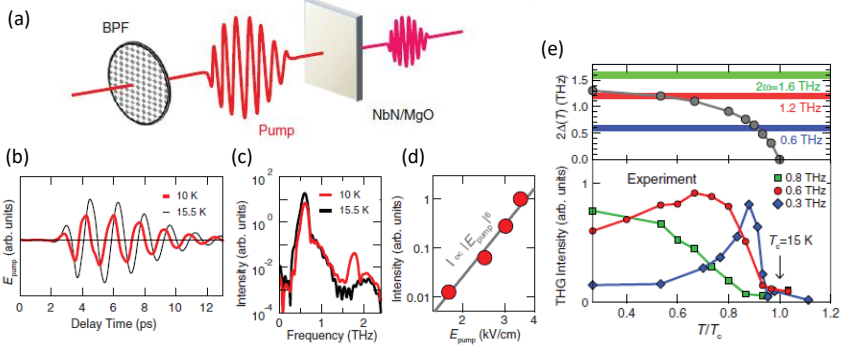


**Figure 1.8:** Third harmonic generation in THz transmission spectroscopy (a) A schematic of the nonlinear THz transmission experiment. (b and c) Waveforms and power spectra of the transmitted pump THz pulses below (10 K) and above (15.5 K)  $T_c = 15$  K, respectively. (d) Power spectra of the transmitted pump THz pulse at various temperatures. Temperature dependence of the TH intensity. (e) Temperature dependence of the order parameter  $2\Delta(T)$  compared with twice the pump frequencies,  $2\omega$  (horizontal lines) (Top). Measured temperature dependence of the TH intensities at  $\omega = 0.3, 0.6$ , and  $0.8$  THz (Bottom). Figure from [6]

contribute to the TH signal [65, 50, 66, 67]. Theoreticians argued that, in a clean superconductor, the CDF contribution to the TH is much larger than the Higgs contribution. At the same time, it was predicted that the TH from the quasiarticle term should exhibit polarization dependence with respect to the crystal axis while the Higgs term is totally isotropic in a square lattice [65]. In these experiments, the TH intensity was independent to the incident polarization angle with respect to the crystal orientation [6]. Such a totally isotropic nature of TH cannot be well accounted for by the CDF term. In most recent theoretical studies, impurity scattering in dirty superconductors can enhance the Higgs signal due to a paramagnetic coupling of light to the condensate [51, 68, 52, 53, 69, 55]. Therefore, the experimental result on NbN superconductor may indicate that the system is in the dirty regime which represents the Higgs contribution dominant TH.

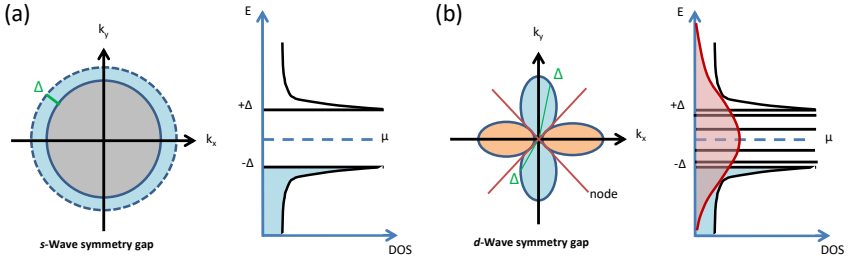


**Figure 1.9.:** The sketch of order parameter symmetry in (a) conventional superconductors (*s*-wave superconductor), (b) high- $T_c$  cuprates (*d*-wave superconductor). Right panels of each figures represent the Density of state of an *s*-wave superconductor and *d*-wave superconductor respectively. The red shaded area represents a quasi-particle continuum at nodes in the *d*-wave symmetry system.

### 1.3.4. Higgs mode in *d*-wave superconductor

Motivated by the pioneering works of the Higgs spectroscopy in *s*-wave superconductor NbN, the unconventional superconductor has been taken to the

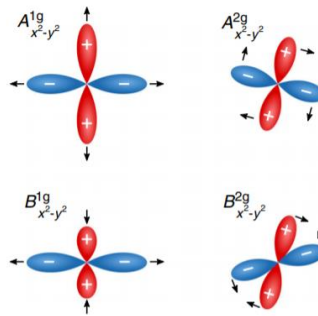


**Figure 1.10.:** Possible condensate oscillation symmetries for a  $d_{x^2-y^2}$ -wave superconductor with point group symmetry  $D_{4h}$  of the underlying lattice. The arrows indicate the motion of the lobes as a function of time. The notation of the gap symmetry in the subscript stresses the initial state, from which the oscillations of the condensate are excited. Figure from [70]

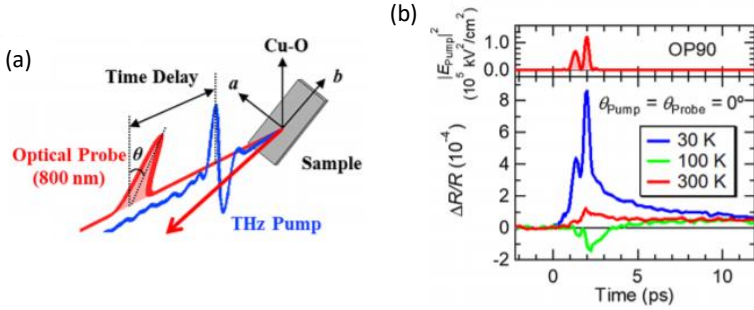


**Figure 1.11.:** (a) A geometry for the THz pump-optical probe measurements on the optimally doped Bi2212 thin film (b) THz pulse-induced transient reflectivity change  $\Delta R/R$  at  $\theta_{probe} = 0^\circ$  as a function of the delay time at typical temperatures. The top panel shows the waveform of the squared THz field. Figure from [73]

stage. In all of superconductor history, cuprates have received the most attention among the high- $T_c$  superconductors. Unlike the momentum-independent gap state of the  $s$ -wave superconductor (Figure 1.9 (a)), cuprates have a  $d$ -wave gap, where the sign of the superconducting gap changes crossing the Fermi surface (Figure 1.9 (b)). Due to its  $d$ -wave gap symmetry, which results in a gapless quasiparticle spectrum, the Higgs mode in  $d$ -wave superconductor is expected to be heavily damped and to decay much faster than the  $s$ -wave oscillations.

Moreover, theoretical works have shown a finite momentum transfer and quench symmetry for an identification of the resulting Higgs oscillations in  $d$ -wave gap symmetry. As shown in Figure 1.10, additional Higgs modes ( $A_{2g}/B_{1g}$ ) with lower energies are expected, representing oscillations of the gap in different symmetry channels [71, 72, 70].

Experimentally, the Higgs mode was observed in a  $d$ -wave superconductor  $\text{Bi}_2\text{Sr}_2\text{CaCu}_2\text{O}_{8+x}$  (Bi2212) [73, 74], by THz pump-optical probe measurement (Figure 1.11 (a)). The optical reflectivity shows an oscillatory signal following the squared THz electric field, markedly enhanced below  $T_c$  (Figure 1.11 (b)). The observed oscillatory signal corresponds to the  $2\omega$  modulation of the order parameter as observed in an  $s$ -wave NbN superconductor under

the subgap multicycle THz-pump irradiation. This transient signal is suggested as a THz-pump-induced optical Kerr effect, namely the third-order nonlinear effect induced by the intense THz-pump pulse. The THz Kerr signal is further decomposed into  $A_{1g}$  and  $B_{1g}$  symmetry components from polarization-resolved measurements. From the comparison with the BCS calculation of the nonlinear susceptibility, the  $A_{1g}$  component was assigned to be the  $d$ -wave Higgs-mode contribution. However, the precise physical origin of the dominance of the Higgs-mode contribution to the THz Kerr effect has not been revealed. It may be a general property of nonlinear susceptibilities in the superconducting state at THz frequencies.

Like in  $s$ -wave NbN superconductor under the subgap multicycle THz-pump irradiation, one can expect the TH signal from high- $T_c$  cuprates. Furthermore, phase-resolved periodically driving the Higgs oscillation would reveal resonance and coupling to other modes as well. The following chapter shows studies of the TH signal from high- $T_c$  cuprate superconductors.



# TERAHERTZ THIRD HARMONIC GENERATION IN CUPRATE SUPERCONDUCTORS

While both free and driven Higgs oscillations have been demonstrated in *s*-wave superconductors, the Higgs mode of *d*-wave superconductors is more complex. The continuous variation of the gap  $\Delta$ , between 0 and  $\Delta^{max}$  along different directions of the Brillouin zone leads to strong dephasing of the mode (Figure 1.9 (b)). This is compounded by the existence of quasiparticle excitations at arbitrarily low energies, which provide rapid decay channels and significantly damp the mode [75]. THz pump optical probe experiments on  $\text{Bi}_2\text{Sr}_2\text{CaCu}_2\text{O}_{8+x}$  (Bi2212) single crystals presented the first experimental evidence for an isotropic Higgs response of *d*-wave superconductors as introduced in the section 1.3.4. However, due to the strong decaying of the Higgs oscillations an unambiguous free oscillating Higgs response could not be observed. A clear proof of a Higgs oscillation and the oscillation phase would reveal useful information about damping

and resonance coupling to other modes. Here, the Higgs amplitude mode of several cuprate thin films are shown with using phase-resolved terahertz (THz) third harmonic (TH) generation. Results of this chapter are published in Ref. [76].

## 2.1. Third harmonic response of $d$ -wave superconductors

Probing the Higgs mode can be accomplished by using a multicycle, carrier-envelope phase-stable THz source with narrow bandwidth and high electric field strength, which is provided by the TELBE superradiant undulator source at HZDR [77]. Using this facility, we investigated the TH response of optimally-doped  $\text{La}_{1.84}\text{Sr}_{0.16}\text{CuO}_4$  ( $T_c = 45$  K),  $\text{DyBa}_2\text{Cu}_3\text{O}_{7-x}$  ( $T_c = 90$  K),  $\text{YBa}_2\text{Cu}_3\text{O}_{7-x}$  ( $T_c = 88$  K), and overdoped  $\text{Bi}_2\text{Sr}_2\text{CaCu}_2\text{O}_{8+x}$  ( $T_c = 65$  K) thin films (see the sample properties in Appendix A.1). Our experiment was performed with 0.7 THz driving frequency, with an electric field reaching  $\sim 50$  kV/cm.

To illustrate the TH response of  $d$ -wave superconductors, first we show the THz transmission through LSCO(OP45). As seen in Figure 2.1 (a)-(d), while the residual fundamental harmonic (FH) dominates the THz transmission above  $T_c$ , a large amplitude of TH component becomes visible below  $T_c$ . Moreover, the FH transmission ( $I_{FH}$ ) monotonically decreases with decreasing temperature as shown in Figure 2.1 (e). In comparison, TH intensity ( $I_{TH}$ ) exhibits a maximum below  $T_c$ .

In the context of superconductors, the nonlinear Meissner effect [78, 79], charge density fluctuations (CDF) [65], and Higgs oscillations have been previously reported or discussed to give rise to TH. Unlike what is observed in this study, the nonlinear Meissner effect manifests as a narrow peak around  $T_c$  in the 3<sup>rd</sup> order nonlinear current. It is often discussed in terms of nonlinear Josephson current and might be probing the phase response of weakly connected superconducting islands [23]. On the other hand, studies on  $s$ -wave superconductors have suggested an anisotropic response from CDF, while TH from the fully symmetric ( $A_{1g}$ ) Higgs oscillation is expected

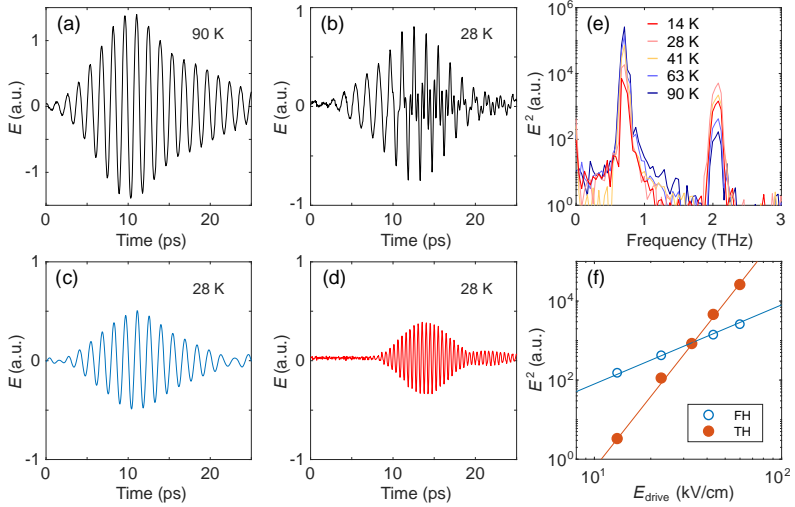


**Figure 2.1:** TH from driven Higgs oscillation in LSCO(OP45). (a,b) THz field transmitted through LSCO(OP45) at 90 K and 28 K. A 2.1 THz bandpass filter is placed after the sample to suppress the 0.7 THz transmission (see Appendix A.1). (c,d) 0.7 THz fundamental harmonic (FH) and 2.1 THz third harmonic (TH) extracted from b using 1.4 THz FFT low pass and high pass filters. (e) FFT power spectrum of the transmitted field at selected temperatures across  $T_c = 45$  K. f, Transmitted FH and TH power versus incoming FH field at 28 K. Solid lines are guides-to-the-eye with a slope of 2 and 6. Figure from [76].

to be isotropic [73, 74, 65, 80, 70].

To distinguish between CDF and the  $A_{1g}$  Higgs response, we performed TH polarization dependence measurements. An isotropic response is found to dominate (Figure 2.2 (a),(c)). In addition, we performed THz pump optical probe measurements similar to refs. [73, 74]. An  $|\vec{A}(\omega)|^2$  response to the  $\vec{A}(\omega)$  driving field is also seen in the condensate's optical reflectivity (Figure 2.2 (b)). These results are consistent with a driven Higgs response to the multicycle THz pulse and its role in TH below  $T_c$ . Finally, to ensure that the Higgs oscillation stays in the perturbative excitation regime, we performed fluence dependence measurements. An excellent agreement with the expected  $I_{TH} \propto I_{FH}^3$  dependence is observed (Figure 2.1 (f)).

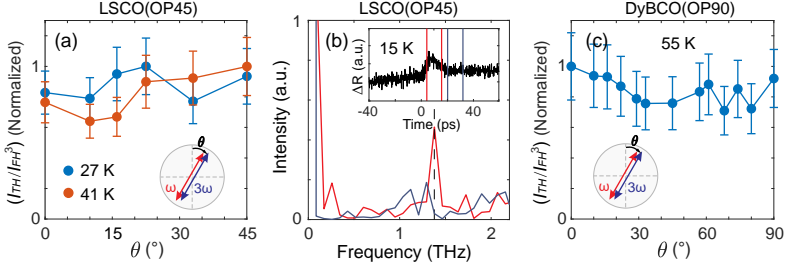


**Figure 2.2.:** Signature of the driven Higgs oscillations in transient response and polarization dependence. (a) TH intensity normalized by the parallel transmitted FH power ( $I_{TH}/I_{FH}^3$ ) for LSCO(OP45) as a function of  $\theta$ , the angle from the Cu-O bond direction. The TH from the Higgs oscillation is expected to be isotropic, while the TH from charge density fluctuation (CDF) is expected to be anisotropic. (b) Transient reflectivity of LSCO(OP45) measured with an 80 fs optical pulse while pumped with a 0.7 THz multicycle THz pulse. The change in reflectivity,  $\Delta R$ , as a function of delay between the pump pulse and the probe pulse is shown in the inset. Main figure shows the FFT power spectrum of the relevant time intervals marked in the inset.  $\Delta R$  exhibits a 1.4 THz (black dashed line) modulation while the pump pulse is on (red line) due to the  $|\vec{A}(\omega)|^2$  coupling of the condensate to the THz drive. The 1.4 THz peak becomes indistinguishable after the pump pulse is gone (blue line). (c) Polarization dependent TH response for DyBCO(OP90). Figure from [76].

## 2.2. Temperature dependence of third harmonic response

To look for potential resonance of the Higgs oscillation at  $2\omega = 2\Delta(T)$ , we performed detailed temperature dependence measurements as shown in Figure 2.3(a)-(c). In LSCO(OP45) we observe a peak in  $I_{TH}$  near  $0.6 T_c$  as well as a smaller peak around  $0.9 T_c$ . DyBCO(OP90) exhibits a similar peak in  $I_{TH}$  near  $0.6 T_c$ . In comparison, YBCO(OP88) exhibits a sharp peak in  $I_{TH}$  near  $0.9 T_c$  and a hump around  $T_c$ .

A careful examination of the transmitted  $I_{FH}$  reveals that the main peak in  $I_{TH}$  originates from the competition between a growing nonlinear response of the Higgs oscillation and an increasing screening of the driving field as temperature decreases. Figure 2.4 shows the residual FH intensity ( $I_{FH}$ ) transmitted through the sample as a function of temperature.  $I_{FH}$  mono-

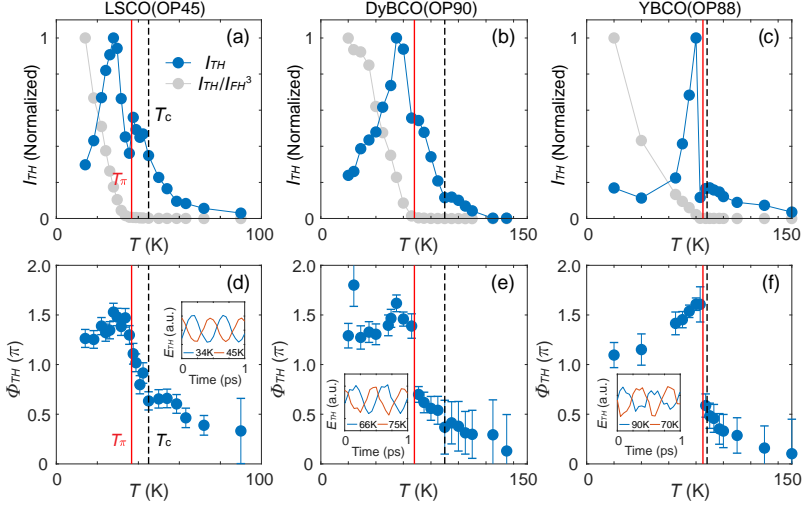


**Figure 2.3.:** Temperature dependence of TH intensity ( $I_{TH}$ ) and relative phase ( $\phi_{TH}$ ) from optimally-doped cuprates. (a-c) Temperature dependence of TH intensity,  $I_{TH}$  (blue), and normalized TH intensity,  $I_{TH}/I_{FH}^3$  (grey), in LSCO(OP45), DyBCO(OP90) and YBCO(OP88). (d-f) Temperature dependence of the relative phase between the TH response and the FH drive, extracted from waveforms such as those in Figure 2.1 (c, d). Inset shows representative TH waveforms across the  $\phi$  phase jump temperature ( $T_\phi$ ). The dotted line (black) denotes  $T_c$  and the solid line (red) denotes  $T_\phi$ . Figure from [76].

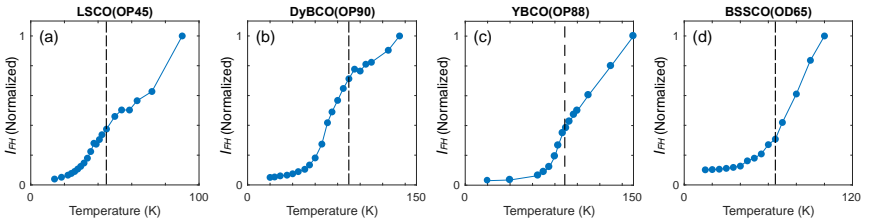


**Figure 2.4.:** Temperature dependence of 0.7 THz FH transmission ( $I_{FH}$ ). The 0.7 THz transmission for (a) LSCO(OP45), (b) DyBCO(OP90), and (c) YBCO(OP88) are obtained from residual FH intensity in the TH experiment. For (d) BSSCO(OD65), FH transmission is estimated from an independent London penetration depth measurement. Figure from [76].

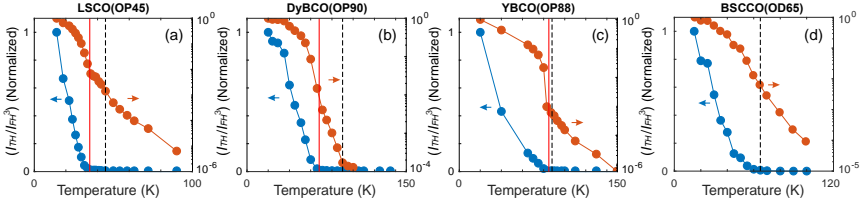


**Figure 2.5.:** Temperature dependence of  $I_{TH}/I_{FH}^3$  on linear scale (blue, left axis) and log scale (orange, right axis). Black dotted line denotes  $T_c$ , red solid line denotes  $T_\pi$ . Figure from [76].

tonically increases with temperature due to the decreasing screening effect of the superconducting condensate. For BSCCO(OD65), the transmitted FH intensity is very weak, resulting in low signal-to-noise ratio. Therefore, an independent London penetration depth measurement is performed on BSCCO(OD65) to extract the transmission coefficient at 0.7 THz. Taking the transmitted FH intensity as an estimate for the electric field inside the superconducting thin film and assuming  $I_{TH} \propto I_{FH}^3$ , we can correct for the screening effect and extract the intrinsic nonlinear response of the Higgs oscillation provided that the FH field inside the superconducting thin film is constant in temperature. This is given by  $I_{TH}/I_{FH}^3$  as shown in Figure 2.5. The absence of a resonance-like peak near  $T_c$ , in contrast to the TH generation from *s*-wave superconductors, is consistent with a heavily damped Higgs mode in *d*-wave superconductors. Note that the dip in  $I_{TH}(T)$  marked at  $T_\pi$  in LSCO(OP45) (Figure 2.3) translates into a kink in the normalized TH (red lines in Figure 2.5). An even stronger kink is seen YBCO(OP88), while in DyBCO(OP90) it is less obvious.

Therefore, the main peak is not a resonance feature. In fact, for optimally-doped cuprates, we expect  $\Delta(T=0) \gtrsim 20\text{meV}$  and a steep onset of  $\Delta$  at  $T_c$ . Thus, the resonance condition  $2\omega = 2\Delta(T)$  is expected to be satisfied immediately below  $T_c$  for  $\omega = 0.7\text{ THz}$  ( $\sim 3\text{ meV}$ ) with the superconducting gap  $\Delta$  is small. In this situation where the system is driven by a continuous and homogeneous ac electric field, a forced oscillation of a harmonic oscillator

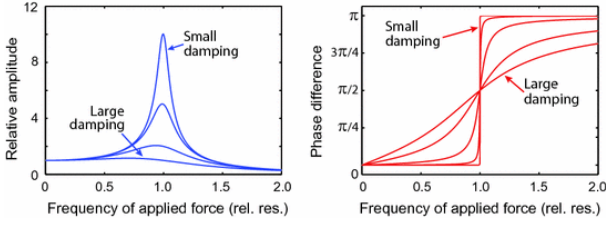


**Figure 2.6.:** The amplitude (left) and the phase difference (right) of a forced oscillation as a function of the frequency of the applied force. Figure from [81].

is equivalent to the TH amplitude behavior. Figure 2.6 shows schematically how the amplitude and phase vary with the frequency of the applied force. At the resonance condition where the frequency of applied force is 1, the relative amplitude shows prominent peak (Figure 2.6 (a)). On the other hand, an overdamped condition denoted as large damping the amplitude becomes broad. Indeed, as the Higgs mode of  $d$ -wave systems is heavily damped, a resonance peak in  $I_{TH}$  is expected to be significantly broadened. The resonance feature can be realized by the phase difference as well. Even in the absence of the peak feature in the amplitude change in the case of large damping, the phase difference shows almost  $\pi$  (Figure 2.6 (b)).

This motivates us to investigate the phase of the driven Higgs oscillation, which is expected to exhibit a prominent change across resonance even in the presence of strong damping.

### 2.3. Phase evolution of third harmonics below $T_c$

In order to extract the relative phase ( $\phi_{TH}$ ) of the TH with respect to the FH signal, we first take the raw FH and TH waveforms from the raw transmitted waveforms using 1.4 THz fast Fourier transform (FFT) low pass and high pass filters. For example, a few extracted FH waveforms from LSCO(OP45) are shown in Figure 2.7 (a). Due to the inductive response of superconductors below  $T_c$ , the FH wave experiences a phase shift across  $T_c$  on transmission through the superconducting thin film. As a first step, we apply a time shift

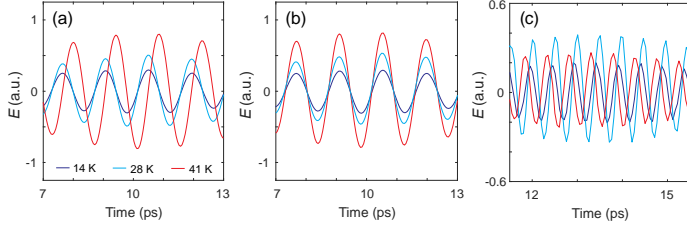


**Figure 2.7.:** Procedure for extracting the relative phase between TH response and FH drive. (a) Raw FH waveforms at a few representative temperatures below  $T_c$  in LSCO(OP45). (b) FH waveforms aligned on top of each other after being shifted in time. (c) TH waveforms at the same temperatures as applied to the FH waveforms. Figure from [76].

$\delta t$  to the FH waveform at each temperature, so that their phases are all aligned with the lowest temperature waveform (Figure 2.7 (b)). Then, we apply the same time shift  $\delta t$  to the corresponding TH waveform at each temperature. The resulting TH waveforms are shown in Figure 2.7 (c). Any phase shift between the TH waveforms in Figure 2.7 (c) has to intrinsically come from the Higgs oscillation itself because the phase shift in the FH drive has already been accounted for. To extract this relative TH phase, we fitted the waveforms in Figure 2.7 (c) to a Gaussian-enveloped sinusoidal function,  $E_{TH}(t) = A \exp(-(t - t_0)^2 / c^2) \sin(\omega(t - t_0) - \Phi)$ , where only  $A$ ,  $c$ ,  $\Phi$  are free fitting parameters.  $\Phi$  is the relative TH phase with respect to the FH drive.

In Figure 2.3 (d)-(f), the extracted TH phase ( $\phi_{TH}$ ) is represented. Despite dissimilar features in  $I_{TH}$ , all three samples exhibit a similar response in  $\phi_{TH}$ . In particular, an abrupt phase jump with amount of  $\pi$  happens at a temperature  $T_\pi < T_c$ . In YBCO(88),  $T_\pi$  is in the range where  $2\omega = 2\Delta(T)$  is expected to be satisfied. However, such a sharp phase jump is again inconsistent with the resonance of a heavily damped collective mode. In LSCO(OP45) and DyBCO(OP90),  $T_\pi$  is significantly lower than  $T_c$ . In light of these, we do not attribute the universal phase jump to the  $2\omega = 2\Delta(T)$  Higgs resonance. A more striking evidence for such an interpretation comes from the direction of the phase jump. Since the low-temperature

regime corresponds to driving below resonance  $2\omega < 2\Delta(T)$  and the high-temperature regime to driving above resonance  $2\omega > 2\Delta(T)$ , a resonance-like phase jump should evolve positively with temperature whereas the observed  $\phi_{TH}$  jumps negatively with temperature.

## 2.4. Discussion

To obtain an intuitive understanding of the phase response, we look at a driven coupled harmonic oscillators model. Whereas isolated oscillators exhibit a maximum in their amplitude and a positive phase jump  $\lesssim \pi$  across resonance [45], the coupled oscillators system develops an anti-resonance in addition to resonances. This manifests as a minimum in the amplitude of the driven oscillator, simultaneous with a phase jump in the negative direction (Figure 2.8 (a)). However, due to the experimental limitations, it is difficult sweeping the driving frequency of the high-field THz source. Therefore we can vary the resonance condition by changing the superconducting gap  $\Delta_{SC}$ . To more closely model our experiment, we fix the driving frequency but allow the energetics of the oscillators to depend on temperature (Figure 2.8 (b)). By choosing their resonance frequencies as  $\Delta(T)$  and  $\delta\Delta(T)$  ( $\delta < 1$ ), where  $\Delta(T) = \sqrt{n_s(T)}$  ( $n_s$  is the experimentally measured superfluid density in LSCO(OP45)), the model recaptures the essential features of LSCO(OP45). A classical Fresnel analysis of the thin film effects also excludes the possibility of the phase jump coming from linear shifts in  $\phi_{FH}(T)$  and  $\phi_{TH}(T)$ .

Our toy model suggests that the coupled mode is underdamped and has an energy scale comparable to the Higgs mode. Moreover, the energy of this mode and/or its coupling to the Higgs mode depends on temperature. Within these constraints, potential candidates for the coupled collective mode include paramagnons, collective charge fluctuations of the incipient charge density wave (CDW) order, or phonons. In particular, coupling between the Higgs mode and CDW excitations has been observed in NbSe<sub>2</sub> and 2H-TaS<sub>2</sub> superconductors [20, 59]. In cuprates, charge order exhibits a similar energy scale as the superconducting gap [82]. Evidence for the

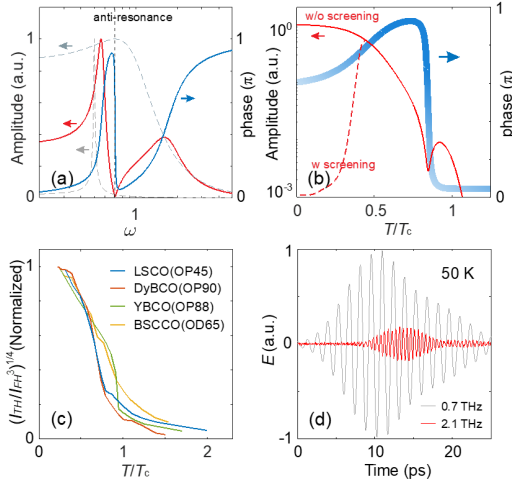


**Figure 2.8.:** Driven coupled oscillators model and finite TH above  $T_c$ . (a) the dotted lines depict the amplitude response of a critically damped harmonic oscillator and an underdamped harmonic oscillator as the driving frequency  $\omega$  is varied. When these two oscillators are coupled, the coupled system retains two resonances but also develops an anti-resonance (vertical dotted line), the amplitude (solid red line) of the driven oscillator goes through a minimum while its phase (solid blue line) jumps negatively with the driving frequency. (b) assuming the driving frequency is fixed as in our experiment, but that the resonance frequency of the two oscillators varies with temperature as  $\Delta(T)$  and  $\delta\Delta(T)$  ( $\delta < 1$ ), the response of the coupled oscillators system is shown as a function of  $T$ . The anti-resonance in (a) is recaptured: the amplitude of the Higgs oscillation (thin red line) goes through a minimum while its phase (thick blue line) jumps negatively with  $T$ . Dotted line illustrate the effect of screening, which is to reduce the driving force and hence the amplitude at lower  $T$ . (c) Temperature dependence of  $(I_{TH}/I_{FH}^3)^{1/4}$ , which remains finite above  $T_c$ .  $(I_{TH}/I_{FH}^3)^{1/4}$  is theoretically predicted to be  $\propto \Delta$  away from resonance. (d) FH and TH components extracted from the transmitted waveform from LSCO(OP45) at 50K  $> T_c$ . Figure from [76].

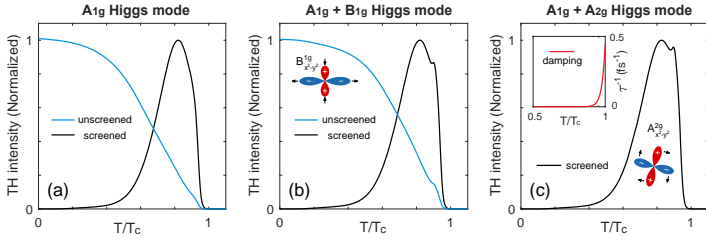


**Figure 2.9.:** Extended Anderson pseudospin model incorporating an (a)  $A_{1g}$ , (b)  $A_{1g} + B_{1g}$ , and (c)  $A_{1g} + A_{2g}$  drive of the complex order parameter  $\Delta$  in the pseudomagnetic field. The inset in (c) shows the temperature-dependent damping function assumed for the model. The drawings in (b,c) illustrate the  $B_{1g}$  and  $A_{2g}$  Higgs modes of the  $d$ -wave order parameter. Figure from [76].

incipient charge order in a wide range of the phase diagram has also been reported [83]. On the other hand, paramagnons are strongly renormalized in the superconducting state into a sharp underdamped resonance mode in a similar energy window as the superconducting gap [84]. They are prominent candidates for mediating Cooper pairing in high- $T_c$  superconductors. Last but not least, strong electron-phonon coupling may also contribute a phononic character to the superconducting order parameter [69], leading to new amplitude mode(s) in the Higgs response [85]. Other exotic but potential candidates include the Bardasis-Schrieffer mode [86, 87] and the non- $A_{1g}$  Higgs mode of the  $d$ -wave superconducting order parameter. The symmetry of these modes is described as  $A_{2g}$ ,  $B_{1g}$ ,  $B_{2g}$  (Figure 1.10). More details of these symmetrical modes can be found in [71, 70]. According to theoretical predictions, the resonance energy of the  $A_{2g}$  and  $B_{1g}$  Higgs mode is less than the  $A_{1g}$  Higgs mode. They might be potential candidate for the new collective mode. The TH response from the driven Higgs oscillation can be modeled by the Anderson pseudospin model. However, a coupling between the  $A_{1g}$  and non- $A_{1g}$  Higgs mode within the Anderson pseudospin model is not straightforward. Therefore, we illustrate below the TH response of an independently driven oscillation of the  $A_{2g}/B_{1g}$  Higgs mode. The detailed model description can be found in [88].

Future doping and magnetic field dependence studies may shed light

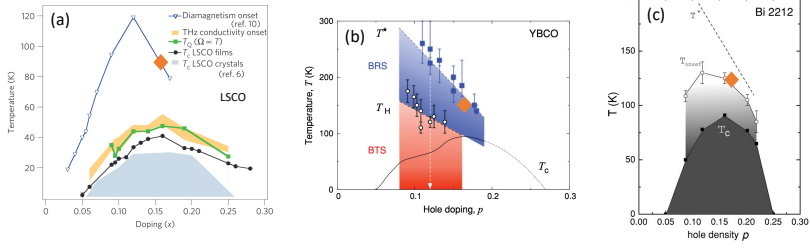


**Figure 2.10.:** Temperature-versus-doping phase diagram of cuprate superconductors (a) LSCO [89], (b) YBCO [90] and (c) Bi2212 [91]. Here, a marked temperature (in orange diamond) expresses the highest temperature where the TH signal exists to compare to the cuprate phasediagram. Showing up the signal up to the pseudogap temperature range above  $T_c$  indicates a possible nonzero pairing amplitude.

on the identity of the coupled mode. While the identity of the coupled mode demands further scrutiny, our experiment also reveals a non-vanishing Higgs-like response above  $T_c$  in all samples. In Figure 2.8 (c), we plot the temperature dependence of  $(I_{TH}/I_{FH}^3)^{1/4}$ , which is theoretically predicted to be  $\propto \Delta$  away from resonance [45]. Indeed,  $(I_{TH}/I_{FH}^3)^{1/4}$  exhibits an order parameter-like temperature dependence below  $T_c$ . Surprisingly, it remains nonzero up to  $T > 1.5T_c$ .

This is more clearly illustrated by the transmitted TH waveform from LSCO(OP45) at  $T = 50K > T_c$  (Figure 2.8 (d)). At the similar temperature regime above  $T_c$ , the superconducting fluctuations has been reported as shown  $T^*$  in the phase diagram of the equivalent cuprate samples of Figure 2.10. The fluctuations can be detected by Nernst experiment detecting a transverse thermoelectric response of a liquid of superconducting vortices. The Nernst signal has a tail deep in the normal state due to superconducting fluctuations. To compare the nonlinearly driven THz signal obtained here with the Nernst signal  $T^*$ , the measured finite TH temperature is marked (diamond) in the phase diagram for LSCO (Figure 2.10 (a)) and YBCO (Figure 2.10 (b)) and Bi2212 (Figure 2.10 (c)). Remarkably, in LSCO, the finite TH temperature of the optimally doped state  $x = 0.16$  is slightly higher than  $T^*$ . In YBCO and Bi2212, the measured TH temperature was

not exceeded than  $T^*$  but still much higher than  $T_c$ . The Nernst signal has provided a disappearance of the Meissner effect at  $T_c$  caused by the loss of long-range coherence, rather than the vanishing of the pair condensate [92].

Our observation may indicate the loss of global phase coherence and preformed Cooper pairs in cuprates, or the intense THz field might enforce phase coherence above  $T_c$  [69]. The pseudogap phase, potentially arising from an underlying CDW order, may also play a role in TH above  $T_c$  [93, 40, 94], to which preformed Cooper pairs and CDF may both contribute.

## 2.5. Summary

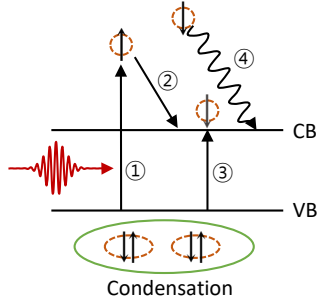
By investigating the nonlinear response of the THz-driven Higgs oscillation in cuprate thin films, we uncovered evidence for a collective mode that is coupled to the superconducting order parameter. In latest experiments we have found that the coupling of the external mode to the Higgs mode can be described within a generalized Fano model. A detailed doping and magnetic field dependent series of Higgs spectroscopy in LSCO and a microscopic model point to phonon mediated CDW fluctuations in the cuprates as origin of the coupled mode [95]. Besides, we have shown a potential nonzero pairing amplitude above  $T_c$ . A deeper understanding of these observations, which may shed light on the microscopic origin of Cooper pairing, requires more detailed theoretical modelling as well as doping and field dependence studies in the future. A driving frequency dependence study may also help distinguish the different scenarios for the closing or filling of the  $d$ -wave gap close to  $T_c$ . In addition, our technique may also serve as a probe for nonequilibrium superconductivity [96, 97]. A first proof of principle experiment on photoexcited LSCO will be discussed in the following chapter. With so many interesting prospects, we see a bright future for phase-resolved spectroscopy of collective modes in superconductors and beyond [98, 12, 99].



# LIGHT-INDUCED HIGGS MODE RESPONSE IN CUPRATE SUPERCONDUCTORS

## 3.1. Introduction to photoexcited transient superconductivity

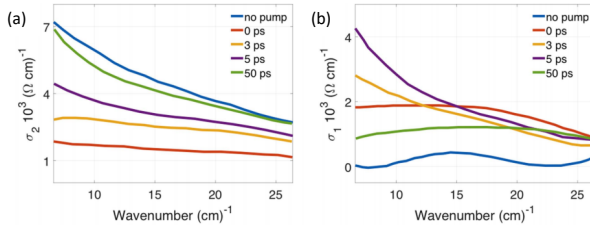
Early ultrafast experiments in high- $T_c$  cuprate superconductors performed optical control of the superconducting state using short laser pulses in the visible (VIS) to near-infrared (NIR) ( $\sim$ eV) regime. Since the superconducting gap is in the energy range of  $\sim$ meV, such experiments result in above gap excitation, and therefore melt the superconducting state with forming hot incoherent quasiparticles [100]. As shown in Figure 3.1 the excited electrons from the condensate state possess a large amount of excess kinetic energy (①). These highly excited quasiparticles thermalize among themselves through electron-electron scattering (②). This leads to a quasiparticle avalanche in which each initially excited particle impacts a subsequent quasiparticle excitation into the conduction band (③). Further energy relaxation



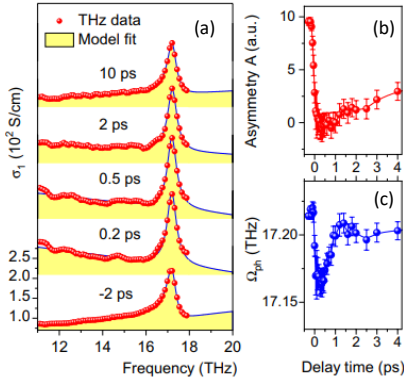
**Figure 3.1.:** Schematic representation of ultrafast nonequilibrium process in a superconductor. ① A light pulse (red) whose frequency is larger than the superconducting gap excites the Cooper pair condensate and gives rise to excess quasiparticle density. ② The excited hot quasiparticles thermalize via electron-electron scattering. ③ excited quasiparticles can knock off the other quasiparticles with causing a quasiparticle avalanche. ④ Further scattering is caused by electron-phonon thermalization.

occurs by electron-phonon scattering (④).

The first experiments could trace the relaxation dynamics back into the Cooper-pair condensate, and were able to distinguish it from the relaxation of hot electrons back into the pseudogap state [104, 105, 106, 107]. A direct

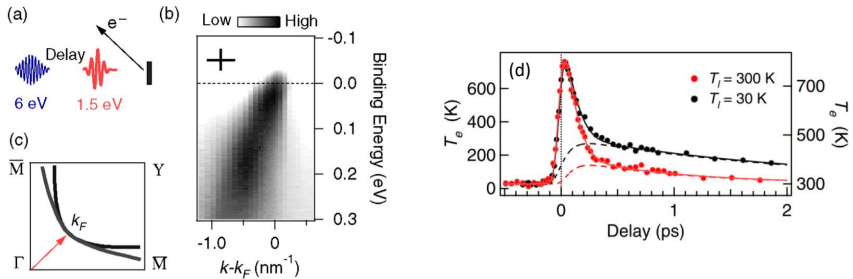


**Figure 3.2.:** Transient THz optical conductivity of underdoped YBCO at equilibrium (blue line) and after photo-excitation. Photo-doping above the gap breaks the superconducting condensate. The divergent inductive response (a)  $\sigma_2$  due to the Meissner effect breaks down right at photo-excitation (red line, 0 ps time delay). The ohmic response (b)  $\sigma_1$  shows the fill-in of the superconducting gap on a 5 ps timescale (purple line) before the system relaxes back into the superconducting state [101, 102, 103].



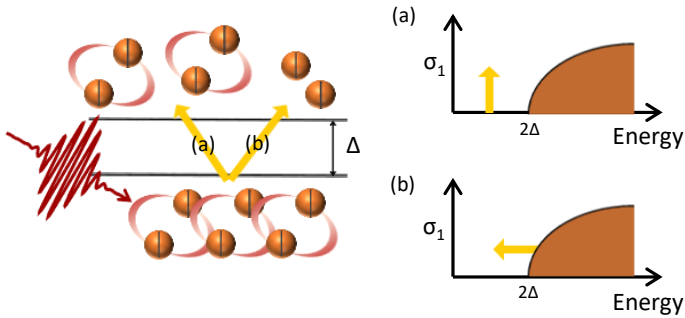
**Figure 3.3.:** Transient apex oxygen mode at 17.2 THz of optimally doped YBCO. (a) The line-shape analysis of the apex oxygen mode at 17.2 THz. The time-evolution of the two relevant parameters, the asymmetry parameter (b) and the mode central frequency (c). Figure from [108].

observation of transient superconducting state can be realized by using the time-resolved terahertz (THz) spectroscopy. This experiment provides a complex optical conductivity with real  $\sigma_1$  and imaginary  $\sigma_2$  terms. In superconducting state, the  $\sigma_2$  shows the divergent inductive response  $\sigma_2 \sim 1/\omega$  due to the Meissner effect (Figure 3.2 (a)) and the  $\sigma_1$  reveals the superconducting gap  $\sigma_1 \rightarrow 0$  (Figure 3.2 (b)). If a pump pulse arrives, a prompt destruction of the superconducting Meissner phase is observed as shown a loss of the divergent inductive response in (Figure 3.2 (a)). At the same time, the real part of the conductivity shows the fill-in of the superconducting gap. Within about 5 ps of the excitation, a broad nonequilibrium spectral weight distribution develops into a metallic-like 'Drude' feature (Figure 3.2 (b)) [102]. Moreover, advanced ultra-broadband THz conductivity showed the dynamics of the superconducting optical gap and specific infrared (IR)-active *c*-axis phonons in optimally doped YBCO [108]. Figure 3.3 (a) exhibits the pump-induced dynamics of the *c*-axis apex oxygen phonon in the mid-infrared range. While the phonon mode is highly asymmetric in the superconducting equilibrium state, it becomes symmetric under the photoexcitation. It is



**Figure 3.4.:** TrARPES experiment for cuprate superconductor. (a) Sketch of the trARPES experiment. An infrared pulse excites the sample while a delayed ultra violet (UV) pulse generates the photoelectrons. (b) Photoelectrons intensity map acquired along the nodal direction. (c) bonding and antibonding Fermi surfaces of underdoped Bi2212 in the reciprocal space. The arrow marks the nodal vector  $k_F$ . (d) Temporal evolution of electronic temperature in the superconducting phase at lower temperature (black, left axis) and in the normal state at high temperature (red, right axis). The solid and dashed lines are numerical simulations of the hot electron and hot phonon temperature, respectively. Figure from [109].

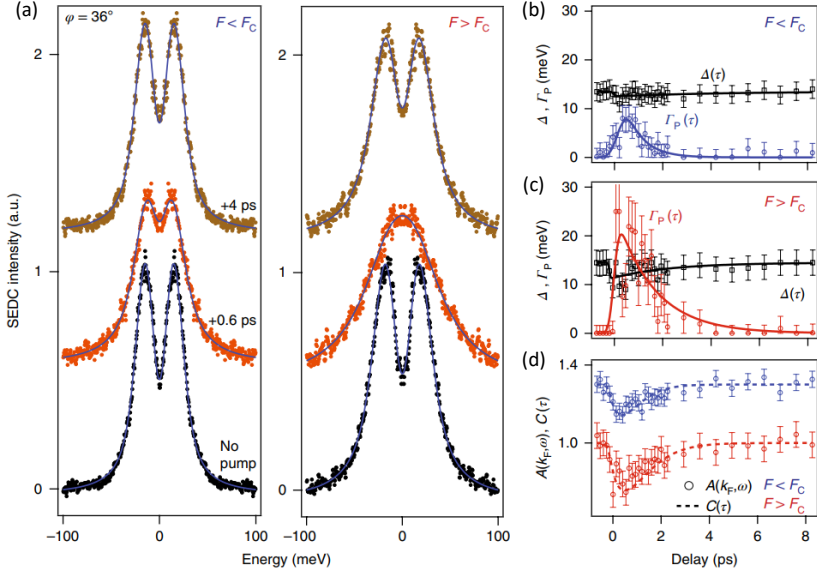
clearly seen in extracted asymmetry factor and eigenfrequency of the apex mode dynamics shown in Figure 3.3 (b,c). The experiment revealed that the apex phonon mode is strongly affected by superconductivity. Similar conclusions for the photoexcited superconductivity could also be drawn from the time- and angle- resolved photoemission spectroscopy (trARPES) measurement which probes the transient electronic band structure dynamics. Figure 3.4 represents the dynamics of photoexcited electrons in optimally doped  $\text{Bi}_2\text{Sr}_2\text{CaCu}_2\text{O}_{8+\delta}$  (Bi2212) [109]. As shown in Figure 3.4 (a), an infrared pulse excites the sample while a delayed ultra violet (UV) pulse generates the photoelectrons. At the equilibrium superconducting state the



**Figure 3.5.:** Different processes governing the excitation dynamics of photo-excited quasiparticles in superconductor. Excitation above superconducting gap resulting either (a) loss of phase coherence or (b) Cooper pair-breaking.

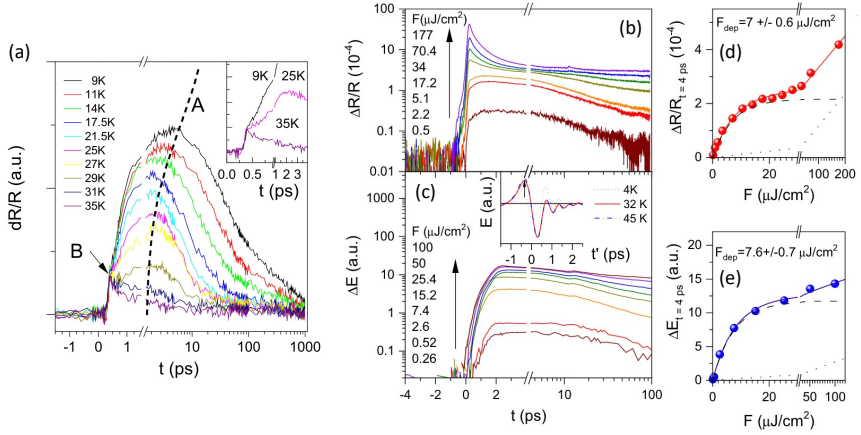
electronic band crosses the Fermi level along the nodal direction (Figure 3.4 (b)), when the crossing wave vector  $k_F$  is depicted in the first Brillouin zone of the system (Figure 3.4 (c)). Figure 3.4 (d) displays the temporal evolution of electronic temperature when the sample is originally in the superconducting phase ( $T_l = 30K$ ) and in the metallic phase ( $T_l = 300K$ ). Hot electrons thermalize in less than 50 fs and dissipate their energy on two distinct time scales, 110 fs and 2 ps. These are attributed to the generation and subsequent decay of nonequilibrium phonons, respectively. This indicates a phonon coupled dynamics. Coupling phonons to the electronic bath can interact even indirectly with the macroscopic condensate. These bosons can be considered as a possible source of the excess phase fluctuations that give a finite lifetime to the Cooper pairs [110, 111]. Likewise, ARPES studies of cuprate superconductors uncovered the filling in the gap due to the pair-breaking interactions as increasing temperature, rather than the simple BCS-like gap closing with increasing temperature [112, 113]. In photoexcited cuprate superconductors, we can expect either filling of the gap without losing the phase coherence (Figure 3.5 (a)) or closing the gap with pair-breaking (Figure 3.5 (b)).

Recent trARPES experiment revealed the dynamics of the phase coherence in Bi2212 [110]. Figure 3.6 (a) shows the superconducting gap along the



**Figure 3.6.:** Temporal evolution of the spectral function of underdoped Bi2212. (a) symmetrized energy distribution curves (SEDC) at  $k = k_F$ , off-nodal cut. (b,c) Ultra-fast dynamics of  $\Delta$  and the pair-breaking term,  $\gamma_p$ , resulting from the global analysis of the SEDCs and momentum energy distribution curves. Pump excitation fluences are defined as  $F < F_c$  (b) and  $F > F_c$  (c). The solid lines are a phenomenological fit to a bi-exponential function convolved with a Gaussian accounting for the temporal resolution. (d) Temporal evolution of the amplitude of the spectral function at  $k = k_F$  and of the phenomenological function  $C(\tau)$ . Figure from [110].

off-nodal cut at a state of the two different excitation fluences,  $F < F_c$  and  $F > F_c$ , where  $F_c$  is a critical fluence. For both fluences employed, the global fit approach of the symmetrized energy distribution curves (SEDC) provides an accurate and reliable determination of the temporal evolution of  $\Delta$  and  $\Gamma_p$  denoting the superconducting amplitude and the pair-breaking scattering rate, respectively (Figure 3.6 (b),(c)). The gap amplitude  $\Delta$  does not show a significant reduction for any excitation fluences. However, spectral weight is completely filled inside the gap as seen the higher pump fluence case in



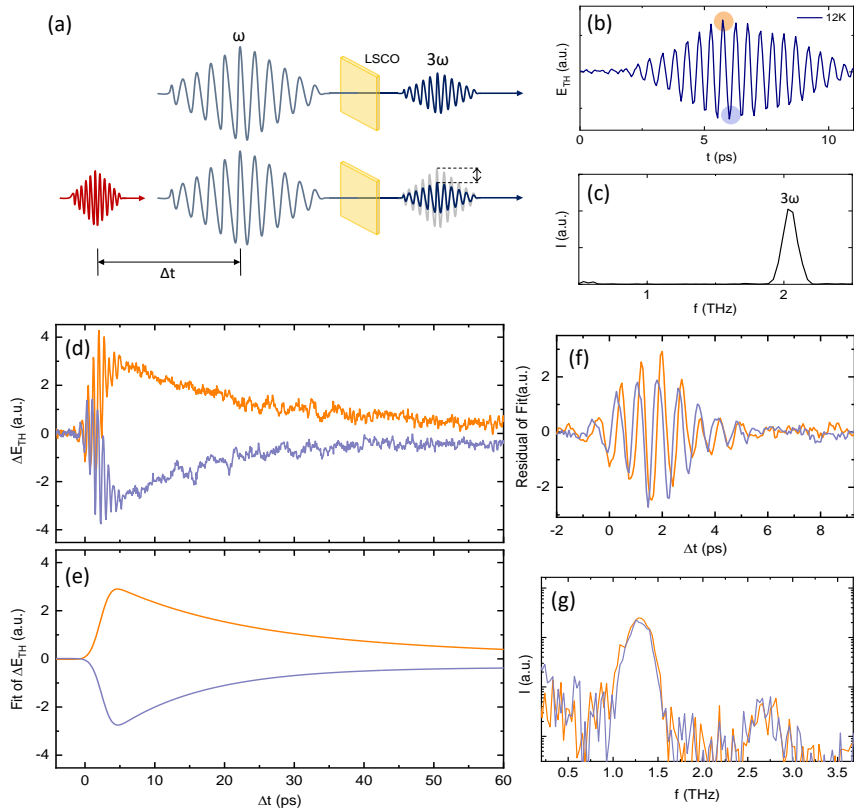
**Figure 3.7.:** Photoinduced dynamics of LSCO via linear optical probes. (a) Photoinduced change in reflectivity  $\Delta R/R$  in  $\text{La}_{1.9}\text{Sr}_{0.1}\text{CuO}_4$  single crystal ( $T_c = 30\text{K}$ ) recorded in the low excitation density limit. Two distinct components (A and B) are observed when probing dynamics with near-infrared pulses (see also inset) [114]. Excitation density dependence of dynamics in  $\text{La}_{1.84}\text{Sr}_{0.16}\text{CuO}_4$  thin film ( $T_c = 31\text{K}$ ) at 4K, excited by 50 fs near-infrared (800nm) pulses. The dynamics are probed in two different experimental configurations: (b) by recording changes in reflectivity at 800nm and (c) by probing changes in THz conductivity. (d) the excitation dependence of reflectivity change at 4 ps after photo-excitation (e) The corresponding amplitudes of the change in the electric field at a fixed time delay (see inset to c) at the time delays at 4ps [115].

Figure 3.6 (a). This is represented by the temporal evolution of  $\Gamma_p$  which is the leading term that drives the dynamics (Figure 3.6 (c)). It shows the prominent enhancement as triggered by the pump excitation. The result exhibits the complete melting of the superconducting condensate without affecting the pairing strength, suggesting the dominant role of phase coherence in the superconducting-to-normal state phase transition. Similarly, the quasiparticle dynamics of a superconducting state in cuprates was investigated via photo-induced transient THz reflectivity [116]. The result was described in terms of a two-component response (Figure 3.7 (a)): a slow relaxation component A and a fast relaxation component B. While the A

component is dominant below  $T_c$ , the B component appears above  $T_c$ . The latter component has been made with the so-called "pseudo-gap temperatures", suggesting its origin in the response of the competing order, like, e.g. charge stripes or charge density wave. On the other hand, the component A can be clearly linked to the dynamics of the superconducting condensate. This pump-probe dynamics was also explored in terms of excitation density dependence. As seen in Figure 3.7 (b), the comparable transient reflectivity was investigated as a function of excitation density in  $\text{La}_{1.84}\text{Sr}_{0.16}\text{CuO}_4$  (LSCO). Only for high excitation densities at the saturating regime, where superconductivity becomes strongly suppressed, the difference between the two responses becomes obvious, representing the fast relaxation clearer. The fast component is absent in the THz response due to the nature of the THz response in a superconductor, which is governed by the change of the phase of the transmitted THz electric field. Details beyond the scope of this introduction with regard to light-induced superconductivity can be found in reviews [103, 117, 111].

### 3.2. Photoexcited dynamics of terahertz third harmonic generation

Although the intense studies on the optical control of superconductivity, these techniques so far performed a spectroscopy of the superconducting gap and the excitation spectrum. A direct probe of the condensate is missing. Such probes recently became possible via non-linear THz spectroscopy within the framework of Higgs-spectroscopy, as discussed in Chapters 1,2. A high-field multicycle THz pulse of frequency  $\omega$  below the superconducting gap allows a forced drive of Higgs oscillations in a superconductor. The characteristic TH generation signal at frequency  $3\omega$  that probes the pairing amplitude of the superconducting condensate. In this section, the photoexcited superconductivity will be investigated and therefore we extend the THz driven nonlinear TH experiment on cuprate superconductor (Chapter 2) [76] to a pump-drive experiment as sketched in Figure 3.8 (a). We initially generate



**Figure 3.8.:** Photoinduced dynamics of LSCO via nonlinear THz probe. (a) Scheme of TH generation in LSCO at equilibrium (above) and optical pump-induced transient dynamics of TH driving, with a time delayed ( $\Delta t$ ) 800nm pulse (below). (b) Generated TH field at equilibrium below  $T_c$  separated with  $3\omega$  physical band pass filter and high pass numerical filter. (c) FFT amplitude of (b) shows clear  $3\omega$  component. (d) Pump-probe dynamics of maximum (minimum) peak position of the TH field of (b) in orange (violet). (e) Incoherent background dynamics of the TH amplitude described by an exponential fit. (f) Coherent oscillatory dynamics of the TH amplitude extracted from the residual of the exponential fit. (g) FFT of (f) representing two modes at  $2\omega$  and  $4\omega$ .

the TH field without optical excitation as previously shown in Chapter 2 [76]. By using a high-field multicycle THz drive  $E_{THz}(\omega)$  at  $\omega = 0.7THz$  (2.5meV) far below the superconducting gap as driving pulse generates the TH field  $E_{THz}(3\omega)$  at  $\omega = 2.1THz$  in a superconducting  $La_{2-x}Sr_xCuO_4$  thin film at 12K ( $T_c = 44K$ ,  $\Delta^{max} = 34meV$  [118]). The measured and digitally filtered TH signal is seen in time-domain (Figure 3.8 (b)) and in frequency domain (Figure 3.8 (c)). Now we excite the superconductor with a femtosecond optical pump pulse (1.55 eV) and probe the TH signal as an imprint of the triggered nonequilibrium superconductivity. The transient dynamics are scanned by varying the pump-drive time delay  $\Delta t$ . Here, two experimental protocols are possible: a two-dimensional (2D) scan can collect THz difference scans at a series of pump-probe delay, or a one-dimensional (1D) pump scan moving one delay line while holding the other fixed. For experimental details, see Appendix A.2. These two methods are complementary. Firstly, the 2D scan offers the complete data set of the dynamics in a broad THz range but probing absolute THz signal. On the other hand, the 1D scan is suitable to observe the relative changes dominantly at a specific frequency range. The measured 1D pump scan with the pump fluence  $\sim 20\mu J/cm^2$  is shown in Figure 3.8 (d). The change of TH field  $\delta E_{TH}$  is obtained at marked positions of the TH waveform (the highest peak colored in orange and the lowest peak colored in violet in Figure 3.8 (b)). The observed  $\delta E_{TH}$  dynamics shows clear excitation-relaxation response with the recovery time  $\sim 20$  ps as we will see. At the comparable low fluence at low temperature, the linear THz probes, which is well suited to study the dynamics of photoinduced quasiparticles [116] do not show clear relaxation feature (Figure 3.7 (c)) [115]. Therefore the nonlinear TH signal is not identified as the excitation spectrum of quasiparticle. As we will show, the TH excitation amplitude itself exposes breaking of the condensate into incoherent pairs and pair-breaking processes of the superconductor. Interestingly, the TH field amplitude is enhanced under the photoexcitation showing the maximum and minimum position changes to positive and negative, respectively. This is due to the interplay with a superconducting fluctuations as we will discuss. Such non-equilibrium TH dynamics reveals a complimentary probe to the

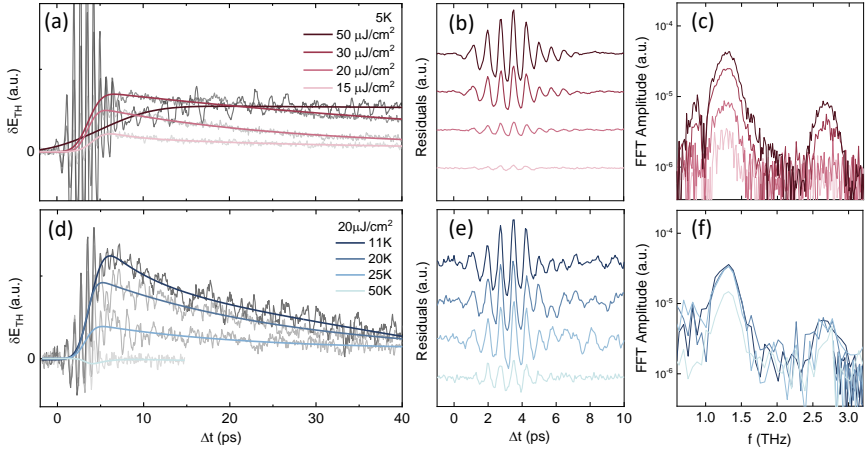


**Figure 3.9.:** 1D pump scans of TH field of LSCO as a function of excitation density (a) and temperature (d). The fits to the background excitation (TH response) are colored. (b,e) Extracted oscillatory features from the residuals of the fits. (c,f) FFT intensity of the oscillations representing two modes at  $2\omega = 1.4\text{THz}$ , and  $4\omega = 2.8\text{THz}$ .

condensate and an intrinsic superconducting fluctuations.

### 3.2.1. Excitation density and temperature dependence of the transient response of third harmonics

In a photo-doping experiment in superconductors changing the pump fluence controls the fraction of broken Cooper-pairs without appreciably increasing the lattice temperature on a picosecond time scale [115, 119, 120, 121, 110]. To understand the pairing amplitude of the photoexcited superconductivity, the pump fluence and temperature dependence of the TH response are investigated. Figure 3.9 (a,d) shows the dynamics of the positive maximum TH field  $\delta E$  under the photoexcitation as a function of excitation density and temperature respectively. To measure the excitation density dependence, we fix the temperature at 12 K and sweep an optical pump fluence from 15-50  $\mu\text{J}/\text{cm}^2$  covering the reported saturation fluence regime  $\sim 42 \mu\text{J}/\text{cm}^2$

where the superconductivity is fully suppressed [115]. For a temperature dependence we use a low pump fluence of  $20 \mu\text{J}/\text{cm}^2$  below the saturation fluence. The 800 nm pump pulse indeed suppresses superconductivity [115, 105, 110]. Even though the origin for light induced changes in the TH signal can be manifold ranging from a Higgs response [51, 68, 52, 53, 69, 55] or charge density fluctuations to induced disorder and excitation of plasmons [65, 50, 66, 67], all these features are a characteristic of the superconducting state. Therefore, a Higgs amplitude response should decrease the TH signal. However the TH signal is enhanced in our study, showing the maximum of the peak field amplitude  $\delta E_{TH}$  increases. As we will show, the TH amplitude needs to be carefully examined since it originates from the competition between a growing superconducting nonlinearity and fluctuations. A detailed experimental studies on cuprates have consistently revealed the simultaneous presence of multiple relaxation processes, implying the possibility of at least two different processes [114].

To characterize the excitation of quasiparticles across the gap and their subsequent recombination, the non-oscillatory part of the signal is fit by a nonlinear function. In analogy to previous studies on other correlated materials [122, 123, 124, 125] the fit function is adapted as

$$\delta E_{TH} = \left( 1 + \operatorname{erf} \left( \frac{t - t_0}{\sqrt{2}\tau_{el}} \right) \right) \left( A_1 \exp \left( -\frac{t - t_0}{\tau_1} \right) + A_2 \exp \left( -\frac{t - t_0}{\tau_2} \right) \right) + c \quad (3.1)$$

where  $t$  is the time delay,  $\tau_{el}$  is the time constant for the excitation of photo-carriers,  $\tau_1$  and  $\tau_2$  is the time constant of exponential decay and  $A_1, A_2, c, t_0$  are constants. Figure 3.10 (a,b) shows the fit curves of the TH amplitude changes to show the nonequilibrium TH dynamics as a function of excitation density and temperature, respectively. The excitation-relaxation dynamics is prominent in mostly at low-pump fluences. The extracted timescales of the fast relaxation dynamics  $\tau_{fast}$  are plotted as a function of pump-fluence and temperature in Figure 3.10 (c,d). At low pump fluences  $< 30 \mu\text{J}/\text{cm}^2$  and low temperatures  $< 20 \text{ K}$  the fast relaxation time exhibits  $\sim 20 \text{ fs}$ . In terms of long

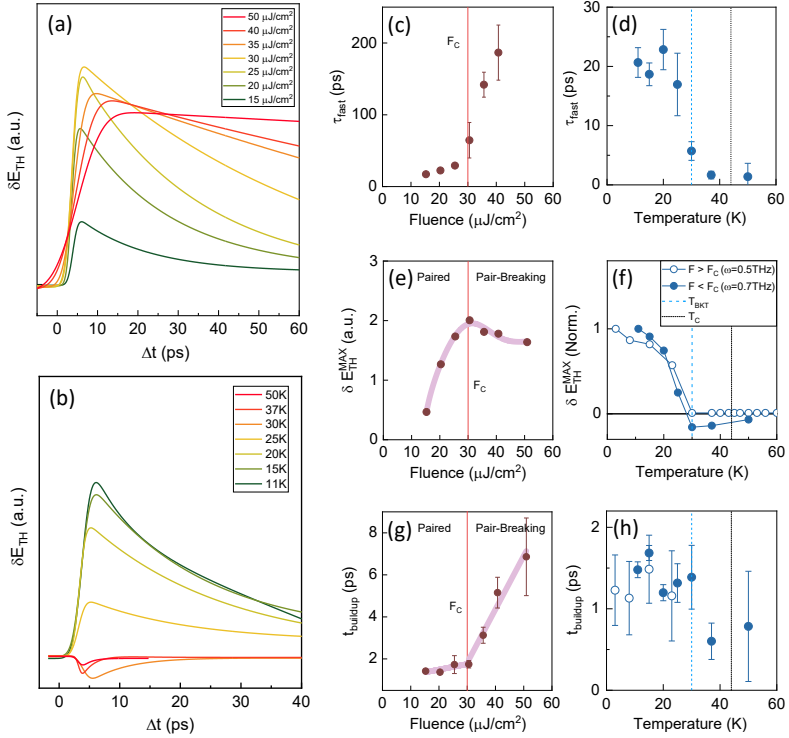


**Figure 3.10.:** Evolution of the TH changes in LSCO. Fitted incoherent background excitation as a function of temperature (a) and excitation density (b) obtained using two exponential decay fits. (c,d) Fast relaxation time  $\tau_{fast}$  of the TH signal. (e,f) The TH amplitude change maximum  $\delta E_{TH}^{MAX}$ . (g,h) The extracted buildup time  $t_{buildup}$ .

relaxation dynamics, a full recovery to the equilibrium state has not seen in the measured pump-drive  $\Delta t$  time range up to 60 ps. This longer relaxation dynamics seems due to electron-phonon thermalization that affects the TH field [126, 127]. In comparison to optical pump-THz probe experiments, the linear THz probe showed only slow relaxation feature  $\tau \gg 10$  ns [115]. This indicates that the nonlinear TH signal is not identified as an excitation spectrum of quasiparticles. The temperature-dependent relaxation time becomes much faster near  $T_c$  as increasing temperature (Figure 3.10 (d)). It

can be clearly linked to the dynamics of the superconducting condensate.

Apon increasing the pump fluence, the fast decay time  $\tau_{\text{fast}}$  increases and shows abrupt changes at  $30 \mu\text{J}/\text{cm}^2$  to few hundreds ps timescales (Figure 3.10 (c)). This fluence regime can be a critical fluence  $F_c$  where the superconductivity fully is suppressed. That is realized by the following analysis of the TH excitation amplitude and excitation build up time. Figure 3.10 (e) shows the TH amplitude changes  $\delta E_{TH}^{\text{MAX}}$  as a function of pump fluences. On increasing the pump fluence the TH amplitude increases nonlinearly indicating a superconducting response as shown in the optical pump probe and broad-band THz experiments [115]. However, above  $F_c = 30 \mu\text{J}/\text{cm}^2$ , the TH change  $\delta E_{TH}$  shows a reduction of excitation while the reflectivity changes of  $\Delta R/R$  keeps increasing linearly [115, 105, 101]. Likewise, the linear optical and THz probe showed the quasiparticle response of the broken Cooper pairs above  $F_c$ . The TH amplitude suppression at high laser fluences as observed here is typical for an amplitude response due to a depletion of the condensate and as being observed e.g. in photo-excited excitonic insulators [61]. This is in agreement with a recent trARPES study that also showed a complete melting of the superconducting condensate without affecting the pairing strength in this fluence regime [110]. Therefore probing the TH signal can be understood as a paring amplitude under the photoexcitation. This is further underlined by the timescale of a buildup of quasiparticles.

In the previous trARPES study [120], stimulated emission of Cooper pairs was investigated by trARPES experiments. They studied a buildup time  $t_{\text{buildup}}$  that is a taking time to reach the maximum excitation amplitude and figured out that photoexcited Hot quasiparticle dynamics speeds up as increasing pump fluence due to a direct breaking of Cooper pairs and a quasiparticle avalanche effect. In analogy to this study, we take time scales from the TH excitations at the maximum changes and define it as a buildup time  $t_{\text{buildup}}$  (Figure 3.10 (g,h)). Our result showed an opposite behavior that the transient TH dynamics slows down of the excitation and even the  $t_{\text{buildup}}$  abruptly increases above  $F_c$  (Figure 3.10 (g)). We interpret it as the incoherent pairs are likely not broken directly via incoming photons at  $F < F_c$  and the possible empty states for such generated quasiparticles

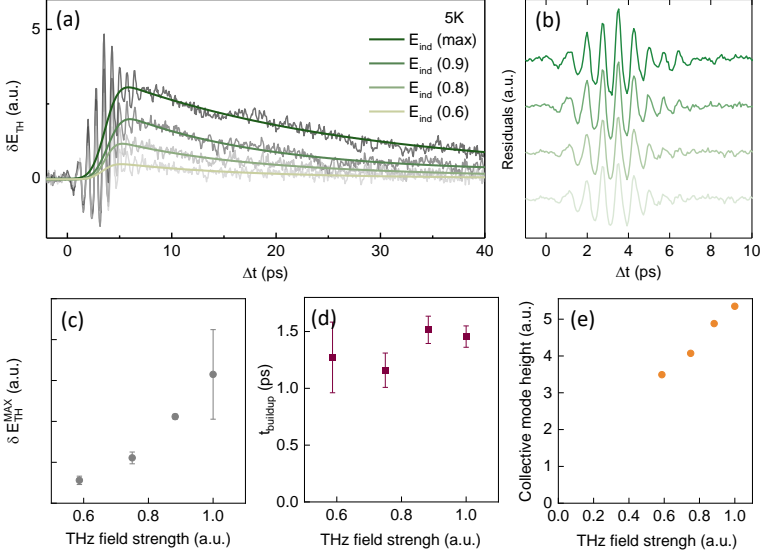


**Figure 3.11.:** THz fluence dependent TH dynamics under the photoexcitation. Optical pump pulse is fixed with  $F < F_c$  and the temperature at 5K. (a) The evolution of TH changes as a function of time delay  $\Delta t$ . (b) The extracted coherent oscillations. (c) Maximum field changes of the TH response. (d) Extracted buildup time  $t_{buildup}$  in (d) and the intensity of the coherent  $2\omega$  oscillation in (e).

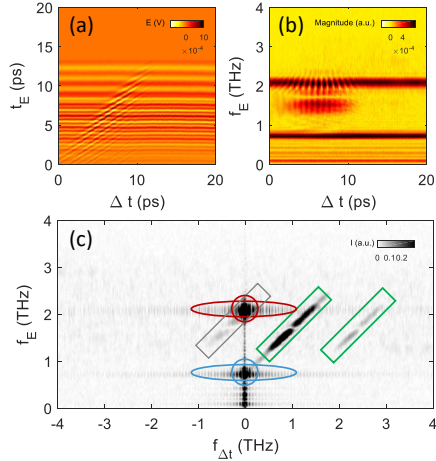
are already blocked by quasiparticles from the direct Cooper pair breaking channel at  $F > F_c$ . Thus, the dynamics of the pairing amplitude changes slows down. To compare the TH excitations under photoexcitation and THz driving field density, we performed the pump-drive experiment with fixed low pump fluence and low temperature, varying the THz field intensity (Figure 3.11 (a)). The characterized TH amplitude shows the linear pump dependency (Figure 3.11 (c)) and  $t_{buildup}$  does not show any change (Figure 3.11 (d)). In the measured THz fluence regime, the TH dynamics exhibits that the pair-breaking is not induced by the THz driving field.

Figure 3.10 (f,h) shows the temperature dependent  $\delta E_{TH}^{MAX}$  and  $t_{buildup}$ , respectively. In Figure 3.10(f), two different set of experiment are shown: a high optical pump fluence  $F > F_c$  with 0.5 THz driving field (opened circle)

and a low optical pump fluence  $F < F_c$  with 0.7 THz driving field (closed circle). In both cases,  $\delta E_{TH}^{MAX}$  decreases on increasing temperature. Also, the minimum of  $\delta E_{TH}^{MAX}$  appears around 30K in both cases. Comparably, the high pump fluence case exhibits saturation indicating no TH changes, while the lower pump fluence regime shows sign flip (clearly seen in the pump probe signal in Figure 3.10(b)). Then the peak amplitudes remain small and decrease towards zero for higher temperatures. An average heating effect due to the pump laser and thus a decrease in  $T_c$  can be ruled out to the origin of changeover feature at 30K, since it is independent to its pump fluences and THz driving field frequency. This describes a dynamical fluctuations of superconductivity setting at 30K. Interestingly, the temperature at 30K is very close to the temperature where the Berenzinskii-Kosterlitz-Thouless (BKT) theory would predict a discontinuous jump in this quantity for an isolated  $\text{CuO}_2$  plane [128]. Even though LSCO is only a quasi-two-dimensional system, but a significant fluctuations of a two-dimensional character was observed below  $T_c$  in the optical spectra [89]. It is also evident in the onset dynamics of the TH changes which speeds up suddenly above 30K indicating the fluctuating order evolution (Figure 3.10 (h)). Indeed, the temperature dependent raw TH amplitude without optical pump showed a significant peak at the same temperature 2.3 [76].

### 3.2.2. Light-induced quantum beats

Now we turn to the oscillatory feature at the early pump-drive time  $\Delta t$  as seen in all 1D pump scans. The residual of the nonlinear fit reveals the oscillations clearly (Figure 3.9 (f)) and the frequency is well matched to  $2\omega$  and  $4\omega$  (Figure 3.9 (g)). To investigate the origin of the TH modulations, we analyse the transient THz response: namely, we have performed pump-drive experiments via electro-optical sampling to enable a continuous scan in each delay time. In general, we can detect a temporal waveform of the transmitted THz electric field,  $E_{THz}$ , by varying the time delay of another optical gate pulse. In this experiment, we fixed the timing of the optical gate pulse and changed the THz pulse travelling time ( $t_E$ ). This allowed us to



**Figure 3.12.:** Transient dynamics of transmitted THz field through LSCO thin film in 2D plot. The used driving THz fluence was  $F_{THz} = 100kV/cm$  and optical pump fluence was  $F_{pump} = 20\mu J/cm^2$  (a) 2D plot of transmitted THz field  $E(t_E, \Delta t)$ . (b) a Fourier transform of (a) along the sampling axis  $t_E$ . (c) the 2D Fourier transform spectra along the both sampling axis  $t_E$  and pump pulse delay axis  $\Delta t$ . color-coded circles mark pump-probe signals which originates from the excited states, described in the main text.

obtain the full 2D spectrum of the transient dynamics of the transmitted THz field as a function of the internal THz travelling time,  $t_E$ , and the pump-drive delay time  $\Delta t$ . For details, see Appendix A.2. Figure 3.12 (a) shows this spectrum in time-domain for fluence  $F_{THz} = 100$  kV/cm of the multi-cycle THz pulse and  $F_{pump} = 20 \mu J/cm^2$  of the optical pump. The vertical pattern along  $t_E$  shows the driven fluctuations. As in usual driving experiments [76], the transmitted signal consists of a fundamental harmonic (FH) and a third harmonic (TH) generated by the superconductor. They are both clearly visible in Figure 3.12 (b) as straight horizontal lines, where the vertical axis is the FFT of the  $t_E$ , at  $f_E = 0.7$  THz and  $f_E = 2.1$  THz, respectively.

When the optical pump sets in, the transmitted field is modulated around the diagonal  $t_E = \Delta t$ , when the THz pulse coincides with the optical pump.

In Figure 3.12 (b) this feature appears as a modulation of TH along  $\Delta t$  persisting for around 10 ps, in addition to a strong transient signal at a frequency lower than  $3\omega$ , around  $f_E = 1.4$  THz. We can disentangle the different contributions in a 2D Fourier space presentation of the data with axis.

Figure 3.12 (c) shows the same response in the FFT coordinates,  $f_E$  and  $f_{\Delta t}$  respectively. This procedure allows to disentangle the information on the signal originated by different processes: namely, high-harmonic generation, transient pumped dynamics and wave mixing processes. In particular, the FH and TH generated by the THz driving field are identified by a blue and red circle, respectively. The corresponding pumped non-oscillatory dynamics discussed earlier is encoded in the signal shown by blue and red cigar shapes. Then, the response which represents the emerged photoexcited dynamics (green and grey rectangles) can be understood as a 4- and 6-wave mixing process (respectively). These signals are characterized by frequency  $f_E = f_{\Delta t \pm \omega}$  and  $f_E = f_{\Delta t \pm 3\omega}$ , respectively: the former, in particular, is responsible for a modulation of the TH signal in pump-drive delay time with a periodicity of  $2\omega$  (and  $4\omega$  at higher order). To investigate more details of the high harmonics feature, we characterize the TH modulation intensities of 1D pump scans as a function of temperature and optical pump fluence. Figure 3.13 (a) shows the temperature dependence of SH modulation intensity,  $I_{2\omega}$  (green, in log scale), alongside with the TH field intensity  $I_{TH}$  (violet, linear scale, from 2.3). From this comparison, we see that both decrease as the temperature increases and they both are detected even above  $T_c$ , but due to the difference scales the transient SH modulation is more sensitive to fluctuations above  $T_c$  than the intrinsic TH signal, which cannot be captured up to such high temperatures. Taking the second derivative of the SH intensity as a function of temperature, we observe three inflection points: the first at  $T_{BKT} = 33K < T_c$ , at which we expect Beresinskii-Kosterlitz-Thouless (BKT) fluctuations in the sample, the second at  $T_c$ , and the third at  $55K > T_c$ , at the onset of superconducting fluctuations. This is in agreement with [89], where linear THz probe allowed to have clear fluctuations up to 55K. Figure 3.13 (b) shows the pump fluence dependent SH modulation

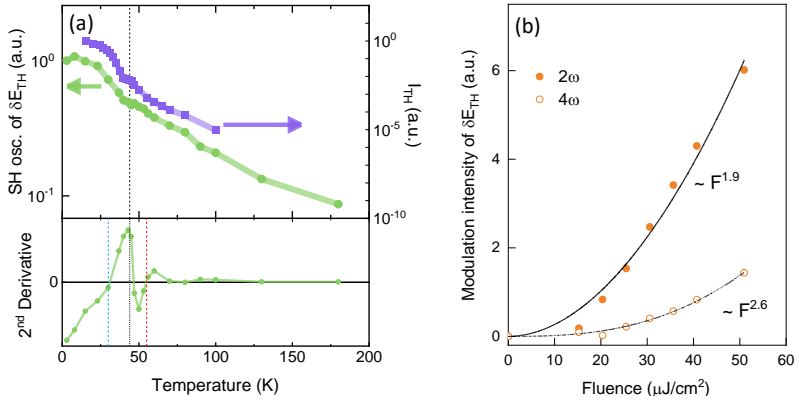


**Figure 3.13.:** Evolution of photoexcited interference feature in LSCO. Intensity of the coherent  $2\omega$  oscillation as a function of temperature (a) and excitation density in (b). (a) The optical induced SH generation is linearly plotted (green, left axis) and TH intensity without optical pump colored in purple in log-scale (right axis). Below, the second derivative versus temperature representing inflection points crossing zero. Blue, black and red dashed vertical lines point to the first sign flip temperature,  $T_c$  and the third sign flip point (superconducting fluctuation), respectively. Power laws in (b) obtained by including the zero intensity.

intensity. Including the zero data shows the nonlinear fit to the data with the factor of 1.9 and 2.6 in  $2\omega$  and  $4\omega$  component, respectively.

### 3.2.3. Photoexcited third harmonic susceptibility response

In fact, the TH amplitude needs to be carefully examined. Since, it emerges from the competition between a growing superconducting nonlinearity and screening by the thermal fluctuations. Such an effect was considered as evaluating the TH susceptibility dividing the TH field amplitude by the transmitted FH field ( $I_{TH}/I_{FH}^3$ ) [76, 74, 129].

In order to examine the features of the transient dynamics of the linear FH component and the nonlinear TH signal distinctly, we now consider a different scheme: namely, we project the data set in Figure 3.12 along the diagonal axis,  $t_E = \Delta t$  as shown in Figure 3.14 (a). This physically cor-

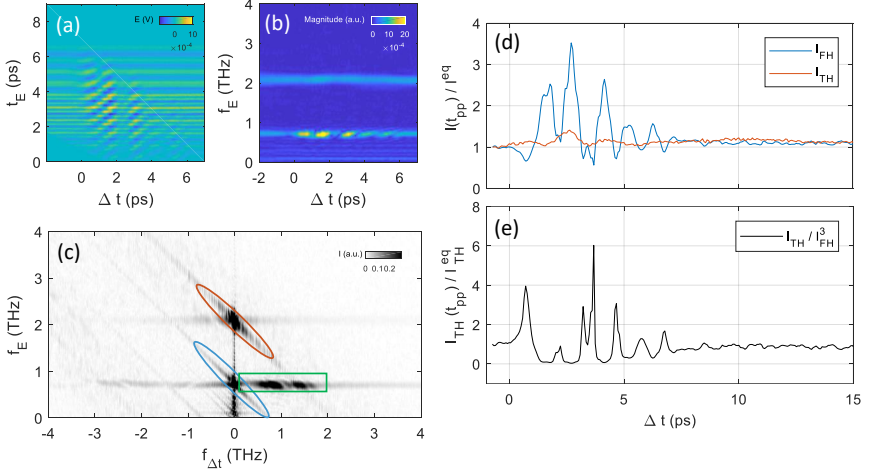


**Figure 3.14.:** Transient and normalized TH response by linear THz dynamics. (a) 2D plot of  $\Delta E (t_E, \Delta t)$  obtained by diagonalize : projection of the 2D data set along the constant  $u = t_E - \Delta t$  axis. (b) A Fourier transform of (a) along the sampling axis  $t_E$ . (c) a 2D Fourier transform spectra along the both time axes. Color-coded circles mark the excited responses in FH and TH, in blue and red cigars respectively, and coherent modulations (green rectangular) (d) Extracted normalized peak intensity of  $I_{FH}$  and  $I_{TH}$  and (e) the intrinsic TH susceptibility as a function of pump-drive time delay.

responds to collecting the response at fixed pump-drive delay, or adopting the method 2 described in ref. [130]. As shown in Figure 3.14 (b) after Fourier-transforming the gate time  $t_E$ , the FH now shows coherent modulations as a function of pump-drive delay time  $\Delta t$ . The modulations are revealed in a frequency of  $\omega$  and  $2\omega$  as clearly seen in 2D Fourier transform spectra (green rectangular in Figure 3.14 (c)). The spectral feature of background excitation-relaxation dynamics is shown in cigar-shaped (blue: TH, red: FH), which is  $45^\circ$  tilted compare to the corresponding feature in the non-projected 2D spectra (Figure 3.12 (c)). In a similar vein, the coherent modulations of the TH field with  $45^\circ$  feature projecting to the time-axis and the synchronized 2D spectra reveals the horizontal feature in the FH component indicating the TH modulations are highly dependent on the FH

modulations. The FH modulations represents the linear coupling to the local field in the frequency of the driving field ( $\omega$ ). With the transient FH and TH signal resolved in frequency at the same time delay (Figure 3.14 (d)), we evaluated the magnitude of the TH susceptibility.

As shown in Figure 3.14 (e) the TH susceptibility normalized by its equilibrium value shows clear modulations for  $\sim 8$  ps similar to the FH modulations. Remarkably, it is clear to see the fully suppressed TH susceptibility at  $\Delta t = 2$  ps. The recovery time scale  $\sim 7$  ps is much shorter than the previous melting of superconductivity experiments via probing time-resolved optical and THz [115]. However, it is in a good agreement with the gap dynamics of shown by time- and angle-resolved photoemission spectroscopy [110]. Therefore, the TH susceptibility can be identified as an intrinsic superconducting order dynamics that is supposedly suppressed under the photoexcitation.

Furthermore, the dominant feature of these coherent oscillations has not been reported in the linear THz broad band experiments. Recently, the study of light-induced supercurrents via multi-cycle THz photoexcitations in s-wave superconducto was reported [69]. They showed the nonlinear oscillating THz photocurrents with high harmonic modes and suggested that the nonequilibrium macroscopic quantum states with broken inversion symmetry are controlled via Cooper pair acceleration by THz photoexcitations.

In our study, the optical-induced coherent modulations with a side band-like component is regarded as an interference response between the nonlinear THz wave in the system and the optical pump. Combining with the transient current emergence, the coherent modulations of fundamental signal in  $\omega$  and  $2\omega$  can be emerged by the transiently driven current due to the photogenerated quasiparticles. It may confirm the quasi-monotonical increase of the sideband modulations in excitation density-dependent TH dynamics of the 1D scan (3.13 (b)).

#### 3.2.4. Summary

This chapter investigated the dynamics of nonlinearly driven THz probe response in LSCO thin film under the photoexcitation. Melting the supercon-

ductivity is captured by suppressing the evaluated TH dynamics, which is accounted for by the Higgs mode response. Moreover, we observe a coherent modulations of TH field which might be caused by the FH modulations. This new feature of coherent response of linear probe regime indicates a transient current emergence resulting in the TH modulations. The possible scenarios are the Higgs mode coupled to the linear probe regime due to a supercurrent acceleration. The time-resolved TH driving may provide a way to investigate the nonequilibrium dynamics of the superconducting order parameter with ps time resolution and applied to the light-induced superconductivity phenomena. We find the amplification and suppression of the TH signal, opening the way for a THz-eV protocol to generate higher harmonics of the THz light as a light-induced quantum beats.

# INTRODUCTION TO THE EXCITONIC INSULATOR

So far we have discussed a condensate of Cooper pairs, which means fermionic condensation usually under the Bardeen-Cooper-Schrieffer (BCS) theory. There is also possibility of bosonic condensate under Bose-Einstein condensation (BEC). Here, we focus on a new concept for a condensate of bosons, excitons (bound states of an electron and a hole).

## 4.1. Excitons

When an electron and a hole attract each other by the electrostatic Coulomb force, we call this is an exciton. That can be usually found in insulators, semiconductors. An exciton can move through the crystal and transport energy, but since an exciton is electrically neutral, it does not transport charge. One way to form an exciton is to excite a material with a photon above its bandgap energy. In this direct process, an electron is excited from the valence band to the conduction band, to which the electron can

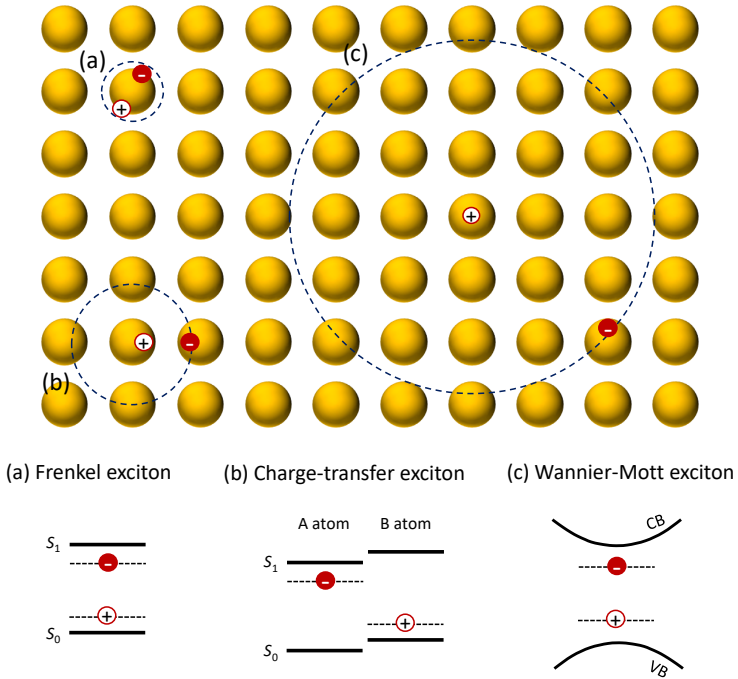


**Figure 4.1.:** Schematic of various types of exciton and corresponding simple band structure. (a) Exciton with a small radius localized strongly at a molecule in an organic crystal or an atom in an organic crystal (Frenkel exciton). (b) Exciton with a strong localization limits the charge transfer processes and diffusion of excitons (Charge-transfer exciton). (a) Exciton with a large radius stretching over many lattice constants and a center of mass slightly shifted toward the heavier hole (Wannier-Mott exciton).

bind due to the attractive Coulombic interaction. Because of the Coulomb interaction between the electron and the hole in an exciton, the internal states are analogous to those of the hydrogen atom, and some of the lower energy states lie below the conduction band by an energy equivalent to the exciton binding energy in that state [131]. Figure 4.1 shows the band models with exciton energy levels classified into three types of exciton. Depending on the value of the binding energy and the spread of the wavefunction over the lattice, excitons in condensed matter can be classified under two main types: Frenkel and Wannier-Mott excitons. Frenkel excitons correspond to the correlated electron-hole pair localized on a single lattice site with relatively high binding energy ( $\sim 1$  eV). They mostly prevail in rare-gas solids and molecular solids with small dielectric constant [132]. Wannier-Mott excitons exhibit hydrogenic electron-hole pairs delocalized over several lattice unit cells with relatively small binding energy ( $\sim$  meV). It arises usually in semiconductors with high dielectric constant [133]. There is an intermediate case between Frenkel and Wannier-Mott excitons, called charge-transfer excitons. The charge-transfer exciton delocalizes on different unit atoms with a static electric dipole moment, found in some insulating transition metal oxides [134, 135].

## 4.2. Excitonic insulator

Excitons are bosonic quasiparticles and therefore can condensate. An excitonic insulator is a novel insulating state formed by the condensation of excitons into a common ground state. It was predicted theoretically to appear in small band gap semiconductors or semimetals with a small band overlap [8, 9, 137, 11, 128, 10]. In Figure 4.2 (a), the formation of the gap of an excitonic insulator is described with the simplest illustration for excitons in a solid: the Wannier-Mott exciton picture. The excitonic insulator is mainly different from the general semiconductor in terms of the bound exciton state and the band gap of the system. In a general semiconductor, excitons are weakly bound and accordingly, the exciton level lies below the

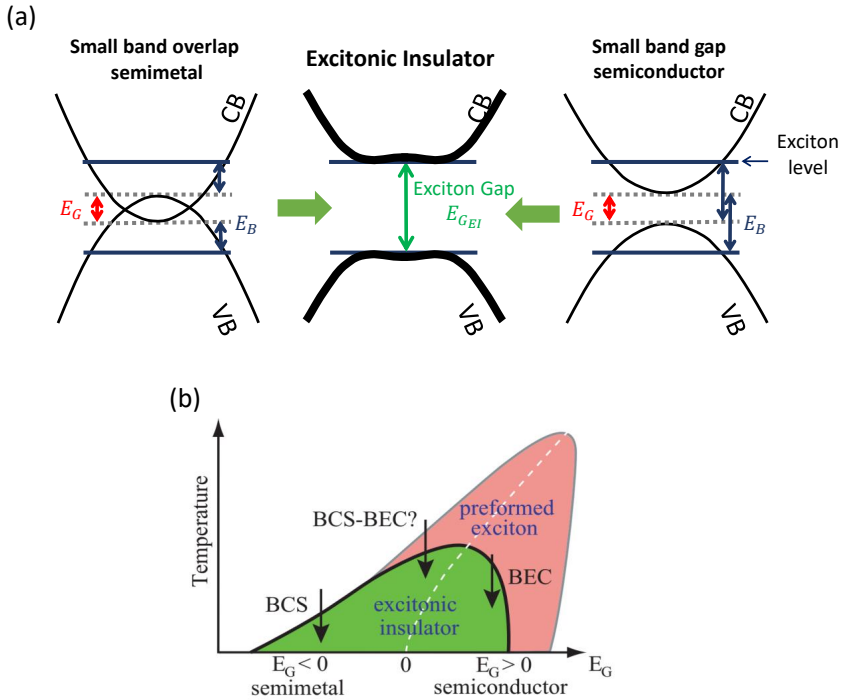


**Figure 4.2.:** Schematic of the transition into the excitonic insulator. (a) Transition into the excitonic insulator phase from the semiconducting (right) and the semimetallic state (left).  $E_G$  in semimetal indicates a negative band gap.  $E_b$  denotes the exciton binding energy. In a semiconductor, a characteristic band flattening occurs when the exciton binding energy exceeds the band gap. In contrast, in a semimetal, the transition occurs if the Coulomb interaction screening breaks down. (b) Phase diagram around the semiconductor/semimetal boundary. The dashed white line separates the semimetallic from the semiconducting phase. The green area denotes the excitonic insulator phase, whereas the red region represents the regime in which a high number of excitons are formed, but no condensation takes place. Figure from [136]

bandgap as shown in Figure 4.1.

If the binding energy of excitons exceeds the band gap, the conventional insulating ground state would be unstable against a new phase, called excitonic insulator, that originates from the formation of an exciton condensate [138]. The same can happen in a semimetal with a slight band overlap. Since the transition occurs at the zero-band gap case ( $E_G = 0$ ) as well, a phase diagram is expected, as seen in Figure 4.2 (b) [139, 140, 141, 142]. It shows that an excitonic insulator emerges at low temperatures in both a semimetal with a small band overlap and a semiconductor with a small band gap. However, the transition into the excitonic insulator has different microscopic characteristics in both regimes. On the semiconducting side non-condensed but stable excitons will start to form at high temperatures above transition temperature ( $T_c$ ) with a binding energy in the order of the band gap. In other words, a large number of excitons are pre-formed (red area in Figure 4.2 (b)), and thermally occupy all the momentum space with a probability given by Bose-Einstein distribution (or in the limit of low exciton densities by Boltzmann distribution) [141, 137]. According to Einstein's works [143], in an ideal gas of identical and non-interacting Bose particles, BEC occurs when the de Broglie wavelength exceeds the mean interparticle distance. Since excitons have integer spin, the excitonic insulating phase transition can be described as a BEC of the strongly bound excitons into their ground state [142].

$$\lambda_{dB} = \sqrt{\frac{2\pi\hbar^2}{m_{exc}}} k_B T \geq n^{-1/2}, \quad (4.1)$$

where  $m_{exc}$  is the exciton mass and  $n$  is the exciton density. This condition yields a simple expression for  $T_c$ , which holds true for a non-interacting gas without internal degrees of freedom denoted as

$$T_c = 3.3125 \frac{\hbar^2 n^{2/3}}{m_{exc} k_B}. \quad (4.2)$$

The equation shows that  $T_c$  is inversely proportional to the mass of the

particles. Since the atomic gas is massive,  $T_c$  of the BEC is in the order of hundreds of nano Kelvin (nK) [143, 144, 145]. Comparably, the exciton is small, therefore,  $T_c$  can be as high as room temperature.

In the transition from the semimetallic side, there are no preformed excitons above  $T_c$  [141]. In this case, the electrons and holes are loosely bounded due to screening of the electron-hole Coulomb interactions. As there are more and more electrons and holes, all the Coulomb forces become increasingly screened, and thus effectively weaker. This means that the exciton wave functions start to grow bigger and bigger, until they all start to overlap with each other. That is, if the spatial extension of the wave function, the condensation emerges. In this regime the excitons are formed at  $T_c$  (band gap) [142]. It is similar to superconductors where the loosely bound Cooper-type pairs emerge at  $T_c$ . In analogy to the electron-electron pair in a superconductor, the electron-hole pair in the excitonic insulator can be well described within the framework provided by BCS theory [128]. In contrast to superconductors, the excitonic insulator is not expected to manifest superfluidity and thus no Meissner effect since the condensed excitons are charge neutral. In optical conductivity measurement, unlike the superfluid  $\delta$ -function response of the superconductor: transfer the spectral weight to the zero frequency (Figure 4.3 (a)), the spectral weight moves to the exciton peak at the gap in the excitonic insulator (Figure 4.3 (b)) [147, 148].

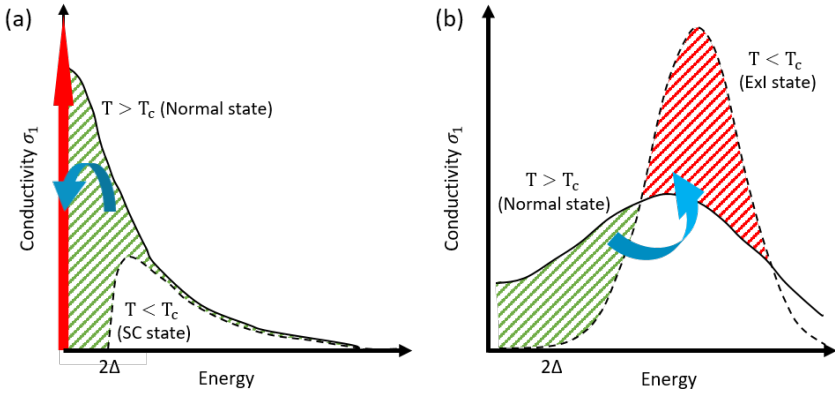


**Figure 4.3.:** The real part of the optical conductivity calculated for (a) the superconductor and (b) the excitonic insulator. The conductivity in the normal state ( $T > T_c$ ) is shown by the solid line, while the conductivity in the condensate state ( $T < T_c$ ) is shown by the dashed line. (a) For  $T \ll T_c$  the superconducting gap  $2\Delta$  is fully formed and there is no absorption below this energy. The green hatched area illustrates the spectral weight that has collapsed into the superconducting  $\delta$ -function at the origin. (b) Excitonic gap is formed with transferred the spectral weight from below an isosbetic point (green hatched area) to higher energies (red hatched area). A gap structure with an absorption peak is well established. Figure adapted from [146] and [147, 148], respectively.

### 4.3. Realization of potential excitonic insulators in the solid state

The excitonic insulator candidates were searched in (1) small band gap systems where exciton pairs can emerge with lower binding energy generating a large number of excitons, and (2) systems with a low concentration of free carriers to reduce the Coulombic screening, which interrupts the attracting force of electron and hole. The materials are suggested in the group V semimetals (Bi, Sb, As) and the divalent fcc metals (Ca, Sr, Yb) [8]. The easiest way to see the excitonic insulating phase is the resistivity measurement since, in general, a transition between metallic and insulating behaviour accompanies a significant change in resistivity. However, the referred can-

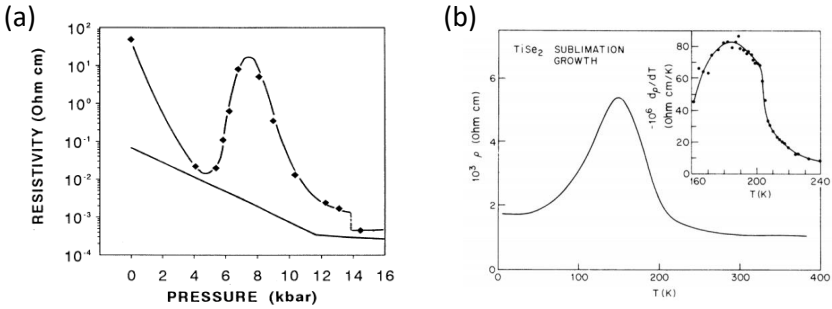


**Figure 4.4.:** Anomalous resistivity of excitonic insulator candidates. (a) Electrical resistivity of  $\text{TmSe}_{0.45}\text{Te}_{0.55}$  as a function of pressure at 300 K (lower curve) and 4.2 K (upper curve). At 300 K, a linear closing of the semiconductor gap is visible with a semiconductor-metal transition at 11.5 kbar [149]. (b) Electrical resistivity perpendicular to the  $c$ -axis for  $1T\text{-TiSe}_2$ . The inset shows  $d\rho/dT$  [150].

didates did not show a clear excitonic insulating transition as varying the gap by inducing pressure or thermal cooling [151]. Bucher and Wachter et al. found a promising candidate of the excitonic insulator in the rare-earth chalcogenide, an indirect narrow-gap semiconductor  $\text{TmSe}_{0.45}\text{Te}_{0.55}$  at ambient conditions. Applying pressure to the system, the band gap varies, and the resistivity shows a pronounced peak at around 8 kbar representing a potential excitonic insulating transition (Figure 4.4 (a)) [152, 149].

Another search direction has been among bilayer structures [153], such as 2D quantum wells in magnetic fields. One can design artificial bilayers to maximize the exciton lifetime under the photoexcitation and achieve the temporal condensation of excitons [154, 155, 156]. Likewise the low-dimensional lattice structure may enhance the Coulomb interactions, and hence increase the exciton lifetime. Researchers have found excitonic insulator candidates in layered bulk materials. The most promising candidates have been suggested in layered chalcogenide systems,  $1T\text{-TiSe}_2$  and  $\text{Ta}_2\text{NiSe}_5$ .  $1T\text{-TiSe}_2$  is well known to demonstrate a commensurate CDW [150], showing an anomalous increase of the resistivity at around  $T_c = 150\text{K}$  (Figure 4.4 (b)) [159, 160]. Above  $T_c$ ,  $1T\text{-TiSe}_2$  has an electronic

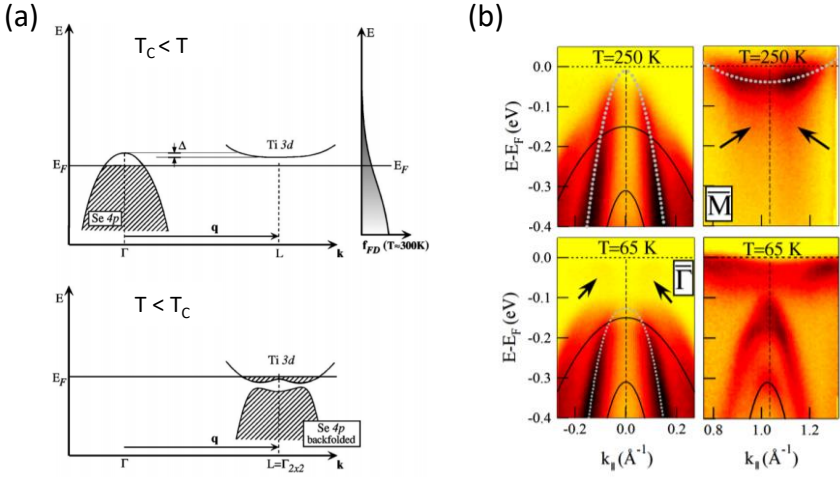


**Figure 4.5.:** Occurrence of an excitonic insulator phase in  $1T$ - $\text{TiSe}_2$ . (a) Schematic of the band structure before and after the phase transition, represented at top and bottom respectively [157]. It implies the required  $(2 \times 2 \times 2)$  reconstruction, corresponding to the spanning (not nesting) vector  $q$ .  $\Delta$  indicates the indirect gap (negative or positive) of the system. (b) Angle-resolved photoemission spectroscopy (ARPES) spectra of  $1T$ - $\text{TiSe}_2$  above and below a charge-density wave (CDW) transition temperature shown in top and bottom respectively [158]. Thick dotted lines are parabolic fits to the bands in the normal phase, and thin dotted lines guide the eye for the CDW phase.

structure near the Fermi energy comparable to that of a semiconductor, but its valence and conduction bands are slightly overlapping through an indirect gap as shown in Figure 4.5 (a) (top). Below  $T_c$ , the indirect electronic band gap becomes direct, hybridizing the valence and conduction bands as shown in Figure 4.5 (a) (bottom). A high-resolution angle-resolved photoemission study of  $1T$ - $\text{TiSe}_2$  showed that the indirect electronic band gap becomes direct, and the valence and the conduction band can hybridize (Figure 4.5 (b)). Besides, a crucial feature of the excitonic condensate, a peculiar flattening of the top of the hybridized valence band, was also captured [157, 161]. However, the origin of the phase transition in  $1T$ - $\text{TiSe}_2$  is controversial since the lattice undergoes a periodic lattice distortion. The driving force of

the phase transition can be either from the excitonic condensation and thus it can destabilize the crystal structure inducing the lattice distortion [160, 162], or the strong electron-phonon coupling based on a Jahn-Teller effect of the general dichalcogenide effect. The latter was suggested from the observation of a soft-phonon mode at the zone-boundary [163]. The origin of the phonon softening (lowering the phonon energy) is still unclear as no first-principle calculations of the phonon dispersion and electron-phonon coupling are available.

Nowadays, both couplings are rather consensually believed to contribute to the formation and stabilization of the excitonic ground state of  $1T$ - $\text{TiSe}_2$  [164]. Recently, static momentum-resolved electron energy loss experiment measured the dispersion and showed softening of the plasmon mode in the material over a similar temperature range providing compelling evidence for exciton condensation [165].

It was indeed shown that while exciton correlations play an important role, they are not the only driving force of the CDW transition in  $1T$ - $\text{TiSe}_2$ , measured by optical pump-broad band THz probe [166]. Moreover, the mixing of phonon and plasmon excitations at  $T_c$  was observed, pointing to strong evidence for electron-phonon coupling in the system [165]. As introduced, the electron-phonon interaction in the presence of the CDW obscures the pure electron-hole interaction.

In this regard, a direct bandgap semiconductor would be useful to study this exotic phase. In the 80s, the layered ternary chalcogenide  $\text{Ta}_2\text{NiSe}_5$  was developed, a direct band gap semiconductor withing a small band gap energy. On cooling,  $\text{Ta}_2\text{NiSe}_5$  reveals an anomalous resistivity change and heat capacity at 328K suspecting to an excitonic insulator. Currently,  $\text{Ta}_2\text{NiSe}_5$  system became one of the most investigated candidate as an excitonic insulator.

#### 4.4. Promissing excitonic insulator candidate : $\text{Ta}_2\text{NiSe}_5$

$\text{Ta}_2\text{NiSe}_5$  crystallizes as a quasi-1D structure of Ta-Ni-Ta chains along an  $a$ -axis (Figure 4.6 (a)). The  $ac$  planes are stacked and bound loosely by

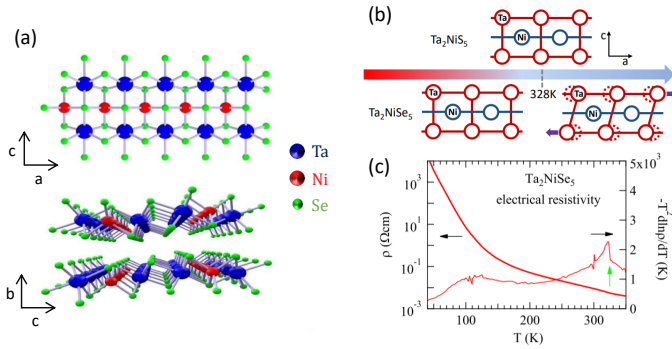


**Figure 4.6.:** (a) Crystal structure of Ta<sub>2</sub>NiSe<sub>5</sub> shown in two orientations emphasizing the layered nature stacked in *b*-direction (top) and the TaSe<sub>6</sub> and NiSe<sub>4</sub> chains along the *a*-direction (bottom). Blue, Red and green represent Ta, Ni and Se atoms respectively. (b) Sketch of the lattice distortion of the chain corresponding to the orthorhombic-to-monoclinic phase transition. (c) Electrical resistivity of Ta<sub>2</sub>NiSe<sub>5</sub> as a function of temperature. The green arrows indicate  $T_c$ . Figure from [148].

van der Waals forces in the direction of *b*. While cooling the system, the electronic resistivity shows the transition of the small band gap semiconducting state to the insulating state at 328 K (Figure 4.6 (c)). This anomaly accompanies a structural distortion from the orthorhombic to the monoclinic phase (Figure 4.6 (b)). The lattice transition corresponds closely to a  $a/2$  *a*-axis sliding between the nearest-neighbouring Ta-chains [167] (see red arrows in Figure 4.6 (b)). This slight distortion does not result in the formation of the CDW [168, 148]. This excludes a lattice distortion-mediated CDW mechanism driving the phase formation [169], suggesting it to be electronic in origin [168]. Recent experimental observations have pointed to the ground state of this material as an excitonic insulator state at the low temperature. If this material is excitonic insulator, questions are raised: what makes excitons stable and overlap sufficiently to condensate. For the first observation of excitonic insulator phase, X-ray photoemission spectroscopy (XPS) and angle-resolved photoemission spectroscopy (ARPES) measurements revealed a flattening of the valence band below  $T_c$  (328K) (Figure 4.7). That was interpreted as the formation of an additional gap [170].

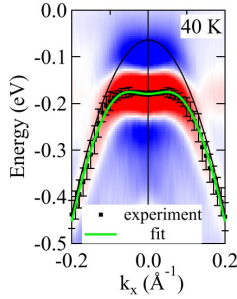


**Figure 4.7.:** A characteristic flat band dispersion [136]. Second derivative plot of the ARPES spectra along the chain direction of  $\text{Ta}_2\text{NiSe}_5$  taken at 40K.

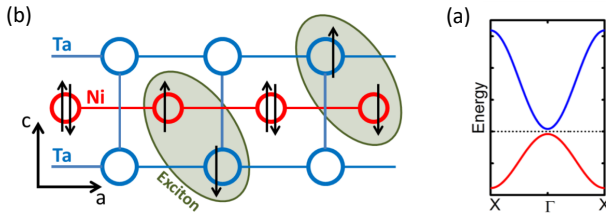


**Figure 4.8.:** Excitonic formation in real space in (a) and band structure of  $\text{Ta}_2\text{NiSe}_5$  in (b). (a) In real space an exciton is formed between an electron on the Ta chains and a hole on the Ni chain. (b) The material is a direct semiconductor with a very small band gap. The valence band is supplied by the Ni chain and the two degenerate conduction bands by the Ta chains. Figure from [171].

Excitons in the  $\text{Ta}_2\text{NiSe}_5$  are formed by a charge transfer between the Ni and Ta chains as sketched in Figure 4.8 (a). This real space separation is believed to be a reason to prevent a fast decay of electron-hole excitations and therefore stabilize the formation of excitons and open the possibility to condensate [171]. Band calculations revealed that the band structure around the Fermi level of this material [168]. A noninteracting band dispersion made by the effective three chain model represents the hybridized Ni 3d-

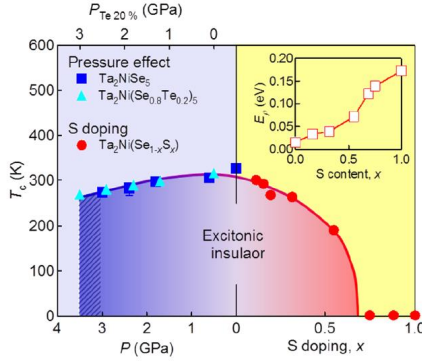


**Figure 4.9.:** Phase diagram of  $Ta_2NiSe_5$ . Applying physical pressure (or Te doping) leads to an increasing band overlap. Sulfide doping increases the (semiconducting) band gap. The inset shows that the transport activation energy at high temperatures ( $T \sim 500K$ ) increases with increasing sulfide concentration, as is expected for an increasing band gap. Figure from [148].

Se 4p valence band and the Ta 5d conduction band (Figure 4.8 (b)). Even though there can be stable excitons due to the structural separation, one can not understand how the charge-transfer excitons are overlapped sufficiently.

From theoretical calculations, electron-phonon coupling is also considered integral to realizing the excitonic insulator phase in  $Ta_2NiSe_5$  [172, 168, 85]. In the following, we will overview the recent studies of excitonic insulator phase in  $Ta_2NiSe_5$  from an additional experimental clues of excitonic insulator phase to the direct probes of a excitonic insulator condensate. Lastly, we will discuss remaining questions about the exciton-phonon coupling in this material.

#### 4.4.1. Clues of excitonic insulator phase in $Ta_2NiSe_5$

As shown an expected excitonic insulator phase diagram above (Figure 4.2), the excitonic state is thermodynamically most stable for a zero-gap semiconductor  $E_G = 0$ . To map out the entire phase diagram of  $Ta_2NiSe_5$ , the transition should also be investigated as a function of the band gap  $\Delta E$ .

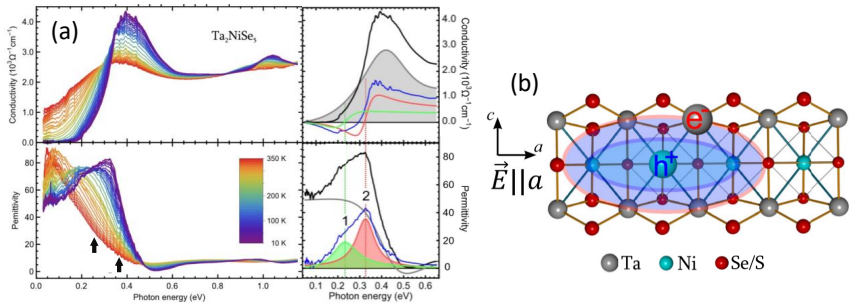


**Figure 4.10.:** (a) Optical conductivity and permittivity as function of photon energy obtained through ellipsometry. The panels on the right of (a) show a generalized Lorentzian fits on the 10K data revealing the electronic background (gray) and two Fano resonances corresponding to the exciton levels. (b) Sketch of the charge-transfer exciton with the self-localized via exciton dressing with a cloud of phonons. Figures from [147].

This is actually possible for this material by applying physical and chemical pressure [148]: The gap can be pushed towards the metallic side by applying physical pressure (or by doping the system with Tellurium) and towards the semiconducting side by doping the system with sulfide.  $T_c$  was measured by electrical transport as a function of pressure and sulfide doping. As a result (Figure 4.9), it reveals a dome-shaped, that reaches its maximum for  $\text{Ta}_2\text{NiSe}_5$  itself. Therefore the phase diagram of  $\text{Ta}_2\text{NiSe}_5$  coincides with a canonical excitonic insulator. In optical conductivity measurements, opening of an excitonic gap was shown [147]. In the left panel of Figure 4.10 (a), a broad continuum is shown with a hump-like structure around 0.3-0.4 eV at a high temperature above  $T_c$ . On cooling the temperature, the spectral weight is transferred from below an isosbestic point of 0.3 eV to higher energy that opens an optical gap. That is in agreement with the expected excitonic gap formation 4.3 (b). Below  $T_c$ , the amount of the gap size reaches  $\Delta E \sim 0.16$  eV in agreement with the ARPES study in which the effected valence band gap was estimated to 0.17 eV. The right side of the figure represents the detailed analysis of the spectra. These represent the

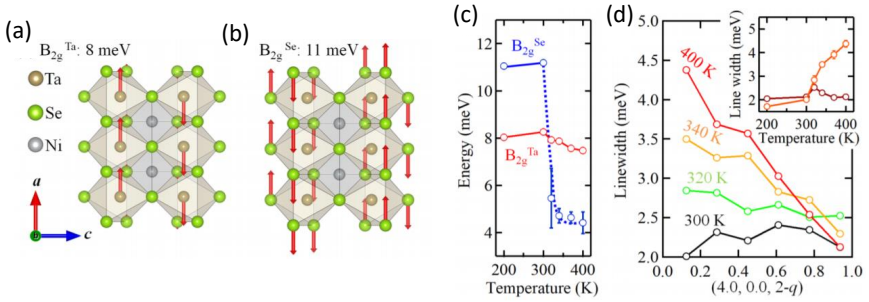


**Figure 4.11.:** Schematic of collective vibration of (a)  $B_{2g}^{Ta}$  and (b)  $B_{2g}^{Se}$  modes. (c) The energy of the corresponding  $B_{2g}$  modes as a function of temperature. (d) Linewidth dispersion of the transverse optical phonon mode at various temperatures. The inset shows the temperature dependences of the linewidth at  $q = (4.0, 0.0, 1.85)$  (orange) and  $q = (4.0, 0.0, 1.06)$  (brown). Figure from [173].

pronounced exciton resonances at 210 meV (1) and 330 meV (2), indicating that the formation of excitons is indeed driving the opening of the gap. Furthermore, since the line shape appears as strong Fano resonances, it reveals spatially extended exciton-phonon states, as illustrated in Figure 4.10 (b). The extended complexes are a key requirement for overlapping wavefunctions between the excitons with large radii and, therefore, the possibility to condense into an excitonic insulator ground state.

The existence of electron (exciton) - phonon coupling was found also in inelastic x-ray measurements [173]. They showed that the antiferroelectric displacement pattern observed in the low-temperature phase could be decomposed into two  $B_{2g}$  phonons of the high-temperature phase that, respectively, involve movements of Ta ions (Figure 4.11 (a)) and Se ions (Figure 4.11 (b)). The Se atomic motion  $B_{2g}^{Se}$  showed a significant frequency jump when approaching the phase transition from the high-temperature side (Figure 4.11 (c)). The Ta ions exhibits a strong linewidth broadening (Figure 4.11 (d)) that points to a strong electron-phonon coupling. Afterwards, Subedi suggested that a  $B_{2g}$  zone-center optical phonon instability would be the primary cause of the phase transition. The motion of the  $B_{2g}$

zone-center mode is exactly consistent to the lattice motion of the structural phase transition. An observation of a softening of the mode as the transition is approached from above would confirm the structural origin of the band gap. If none of the  $B_{2g}$  modes present in the material soften, this would imply that the transition is caused by electronic or elastic instability [174]. This can not be proved by inelastic x-ray experiments [173] (Figure 4.11) since their performed temperature range is low (400K).

Chapter 5 of this thesis presents Raman spectroscopy results in  $\text{Ta}_2\text{NiSe}_5$  to investigate the zone-center  $B_{2g}$  optical phonon mode up to the temperature, much higher than  $T_c$ , at 800K to prove the important interplay of the  $B_{2g}$  mode instability with the excitonic condensate.

The experimental results discussed so far cannot elucidate the microscopic origin of the gap of a potential excitonic insulator. For this purpose, ultrafast methods provide the possibility to gain further insight. Gap melting times observed in trARPES measurements can be used to distinguish exciton-, and lattice- driven dynamics [175, 176]. In particular, for the CDW and the excitonic order in  $1T\text{-TiSe}_2$ , the complicated interplay of electronic interactions and lattice distortions driving the phase transition have been investigated by a time-resolved ARPES [177], electron diffraction [178], and terahertz (THz) spectroscopy [166]. Time-resolved ARPES studies on  $\text{Ta}_2\text{NiSe}_5$  showed that the gap turns to an un-gapped semimetallic state for 150-300 fs after inducing an intense infrared-laser pump pulse (Figure 4.12) [179]. In that short time range, while the hot electrons are immediately excited, the lattice can not follow the excitation remaining its intrinsic crystal structure. The result exhibited a semimetallic state without excitonic contribution at the low-temperature phase of the material. Thus, the gap opening in the low-temperature monoclinic phase would primarily be caused by the excitonic effect and not by the electron-lattice coupling. Further fingerprints stem from nonequilibrium responses of the ground state of  $\text{Ta}_2\text{NiSe}_5$ , that are compatible with the melting and relaxation dynamics [180, 181, 179, 182].

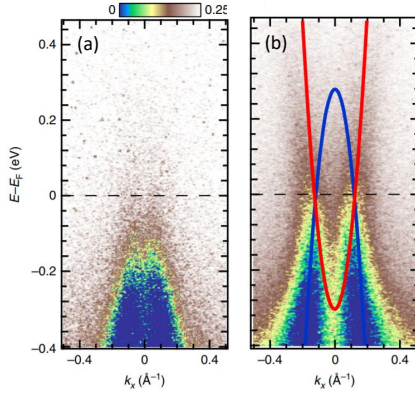


**Figure 4.12.:** tr-ARPES spectra of  $\text{Ta}_2\text{NiSe}_5$  before (a) and after (b) the optical pumping in energy-momentum ( $E - k$ ) distribution. Red and blue parabolas indicate the electron and hole bands crossing  $E_F$  in (b). Figure from [179].

#### 4.4.2. Proof of excitonic insulator phase in $\text{Ta}_2\text{NiSe}_5$

Time-resolved spectroscopies can probe the state's elementary collective excitations, namely, the amplitude and the phase mode in analogy of the Higgs amplitude mode discussed in the cuprates earlier in this thesis (see Chapter 1). Therefore, probing the amplitude mode offers the possibility to map out the transient state's order parameter as a function of temperature and excitation density. For electronically driven transitions, these measurements reveal a characteristic behavior of the electronic Higgs mode that allows distinguishing it from impulsively excited coherent phonons as described in Figure 1.5. The first proof of the excitonic condensate in the system was measured by impulsively excited coherent phonons [12]. The pump-probe response manifests the coherent phonons on top of the relaxation time scale following the excitation at 2 ps (Figure 4.13 (a)). The extracted collective modes in the frequency domain manifests 1-THz, 2-THz and 3-THz mode, respectively (Figure 4.13 (b)). The modes show different characteristics as a function of temperature and excitation density. As temperature changes, the amplitude of the 1-THz phonon mode shows a mean-field order parameter-

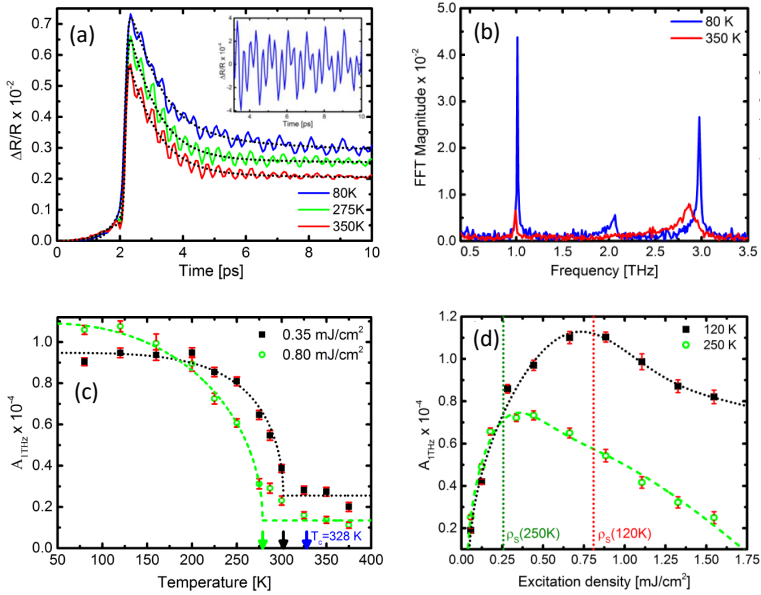


**Figure 4.13.:** (a) Time evolution of the photoinduced reflectivity changes in Ta<sub>2</sub>NiSe<sub>5</sub>. (b) extracted collective phonon modes in frequency domain. The 1-THz mode amplitude as a function of temperature (c) and excitation density (d). Figure from [12].

like behavior (Figure 4.13 (c)), while a coherent (3-THz) phonon exhibits linear dependence (Not shown here, see ref [12]). The 1-THz mode, therefore, is identified as a phonon mode coupled to the excitonic condensate and this hybrid can represent its order parameter. To underline the picture, the systematic measurement of excitonic condensation depletion behavior was performed via varying the excitation density. As seen in Figure 4.13 (d), 1-THz mode reveals that the depletion of the condensate by the pump pulses plays a minor role at the low pump power, representing the mode is not coupled to the excitation condensate. However, the amplitude starts to decrease at a specific excitation density, indicating the coupling to the depleting condensate. This behavior is again clearly distinguished from the linear power dependence of uncoupled 3-THz phonon mode.

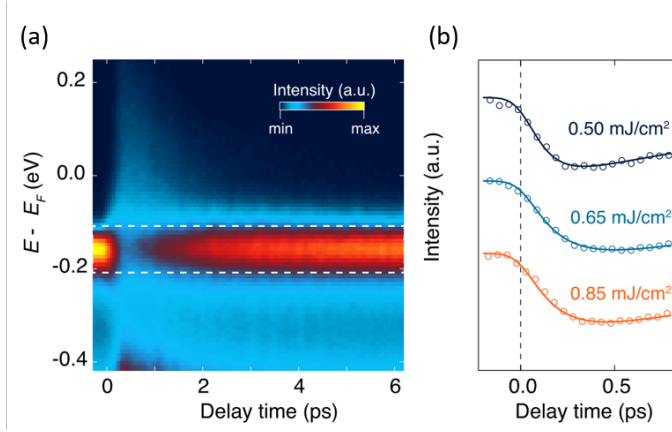


**Figure 4.14.:** Ta<sub>2</sub>NiSe<sub>5</sub> (a) Map of the photoelectron intensity at the  $\Gamma$  point as a function of energy and pump-probe delay. The data have been acquired at 14 K with a probe photon energy of 6.20 eV and an absorbed pump fluence of 0.85 mJ/cm<sup>2</sup>. (b) Excitation-density dependence rise of the photoelectron intensity response at  $\Gamma$  (dotted lines). Figure from [184].

The coherent phonons in Ta<sub>2</sub>NiSe<sub>5</sub> have been intensively studied with the other probe schemes, mid-infrared [180], white light [183] and electronic band dispersion [184, 182]. In addition to the amplitude mode of the excitonic phase, the phase mode was also investigated in this material [13]. By using ultrafast spatially-resolved, pump-probe microscopy, the propagation of the coherent modes allowed to observe the hybridization of phonon modes with the phase mode in Ta<sub>2</sub>NiSe<sub>5</sub>.

Very recently, the spontaneously formed excitons above  $T_c$  were detected by symmetry-selective ARPES [185]. They clearly evidence the existence of the preformed excitons and fully validates the occurrence of an excitonic insulator phase transition in Ta<sub>2</sub>NiSe<sub>5</sub>. The probed excitonic photoemission feature reveals the compact and highly anisotropic size of the excitons as well as their strong scattering, indicating strong exciton–phonon coupling.

### 4.4.3. Remaining questions

Despite the absence of CDW phase in this material, evidences for excitonic condensation have pointed the presence of electron-phonon coupling as introduced in this chapter. If the gap originated from electron-phonon coupling, one would expect it to close on time scales characteristic of structural distortions. As in the case in  $1T\text{-TiS}_2$  [177], trARPES measurement showed a hierarchy of time scales that indicates charge ( $\sim 50$  fs) and lattice order ( $\sim 200$  fs). In  $1T\text{-TiSe}_2$ , the collapse of atomic-scale periodic long-range order happens on a timescale as short as 20 fs. This rapid time scale thus supports exciton condensation [176]. Likewise, recently  $\text{Ta}_2\text{NiSe}_5$  was investigated by trARPES with a high time resolution setup to trace the electronic timescale [184]. Figure 4.14 (a) displays the energy distribution of the photoemission intensity around  $\Gamma$  as a function of pump-probe delay. As shown in Figure 4.14 (b), tracked spectral weight at around  $\Gamma$  (dashed line range in Figure 4.14 (a)) is suppressed under the photoexcitation. The observed response is complete within 0.3-0.4 ps. It is longer time scale than expected response of an excitonic insulator (10 - 100 fs) [186, 187]. This slow response was observed in previous trARPES [181, 182, 179] and transient optical reflectivity [12, 188]. The time scale of electronic excitation dynamics can be correlated to the phonon occupation. Since there is no separate timescales of electronic and lattice response, the electron-lattice complex state called polaronic complex is expected. With this picture, the anomalous stable excitons in the material can be understandable as well as how the small exciton radius can span to entire crystal forming condensate. Thus we suggest a strong exciton-lattice coupling called polaronic complex state in  $\text{Ta}_2\text{NiSe}_5$ . If there is a polaronic complex in the material, one would expect it to close time scales characteristic of the response. However, fingerprints of the complex state in pure electronic responses have not shown so far. In Chapter 6 we will exhibit a polaronic current feature and thus verify the existence of the polaronic complex.

# RAMAN SPECTROSCOPY OF $\text{Ta}_2\text{NiSe}_5$

Although the  $\text{Ta}_2\text{NiSe}_5$  is an up-and-coming candidate to host an excitonic insulating transition, the reason whether the structural phase transition is just happening or involved with the excitonic transition is still controversial. As shown in Figure 4.8 (b), the material is a direct band gap system where no CDW contribution is expected. The structural distortion has been questioned as possible origin of the gap of the system. By the theoretical calculations, in addition to electron-hole interactions, electron-phonon coupling is also considered integral to understanding the excitonic insulating phase in  $\text{Ta}_2\text{NiSe}_5$  [172, 168, 85]. Experimental studies have suggested an electron-phonon coupled state as discussed in Chapter 4.

If one may strictly argue that the gap opening is due to the pure electronic origin rather than the structural origin, the electronic and lattice instabilities should appear simultaneously since they have the same spatial symmetry. The observation of lattice coupling to the transition leaves the question of which electronic and structural instabilities are more important to open the

gap and to what extent.

The possible scenarios of opening the gap are 1) excitons form a condensate and then the lattice is distorted, or 2) the lattice instabilities causes the electronic instabilities due to the strong electron-phonon interaction. These two questions are intensively discussed at the moment. In particular, Mazza et al., and Watson et al., point out the loss of two mirror symmetries in the low-temperature phase are linked to a discrete symmetry breaking [189, 190]. They argued that the excitonic condensation is linearly coupled to the lattice modes leading to a hybridization of the Ta and Ni bands in the center of the Brillouin zone  $q = 0$ . Afterwards, Subedi suggested that a  $B_{2g}$  zone-center optical phonon instability would be the primary cause of the phase transition. An observation of a softening of the mode as the transition is approached from above would confirm the structural origin of the band gap. If none of the  $B_{2g}$  modes present in the material soften, this would imply that the transition is caused by electronic or elastic instability [174]. Motivated by this, we performed Raman scattering studies on  $\text{Ta}_2\text{NiSe}_5$  to probe the soft modes either of lattice or the excitonic fluctuations. The results of this section were published in [191]. To observe the  $B_{2g}$  phonon softening clearly, we heated the sample up to 800K, at far beyond the measured temperature range of inelastic x-ray study [173]. Single crystals of  $\text{Ta}_2\text{NiSe}_5$  were grown by chemical vapor transport reaction as described in [148]. Raman measurements are performed within specific excitation geometries and parameters as detailed in Appendix A.4. Figure 5.1 shows the Raman spectra of  $\text{Ta}_2\text{NiSe}_5$  in  $Y(X-\bar{Y})$  geometry as a function of temperature. The blue spectra are taken in the monoclinic phase (sketched as inset) below  $T_c$  with the probing channel of  $A_g$  symmetry. Above  $T_c$ , spectra shown in red are taken in the orthorhombic phase (sketched as inset) with probing the  $A_g$  and  $B_{2g}$  channels. The grey shaded area represents the filter effect, reducing the spectral weight below  $45\text{cm}^{-1}$  (See Appendix A.4). Starting below  $T_c$  shows clear peaks at  $101, 124, 136, 149, 180, 195\text{cm}^{-1}$  identified to  $A_g$  symmetries by the earlier studies [192, 193]. On increasing temperature, the high-frequency modes do not show strong changes up to  $T_c$  except the modes at  $124$  and  $136\text{cm}^{-1}$ , shifting to lower energy and broadening. At

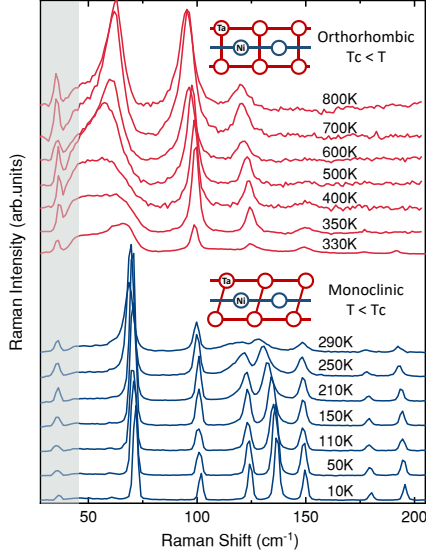


**Figure 5.1.:** Raman spectrum of  $\text{Ta}_2\text{NiSe}_5$  in the orthorhombic phase above (red) and in the monoclinic phase below (blue) the structural phase transition at  $T_c = 328\text{K}$ . At the phase transition the Ta chains perform a shear displacement with respect to the Ni chain. The corresponding crystal structures are shown as insets. Spectra are taken in (X-) geometry revealing the  $A_g$  channel below and  $A_g + B_{2g}$  channel above  $T_c$ .

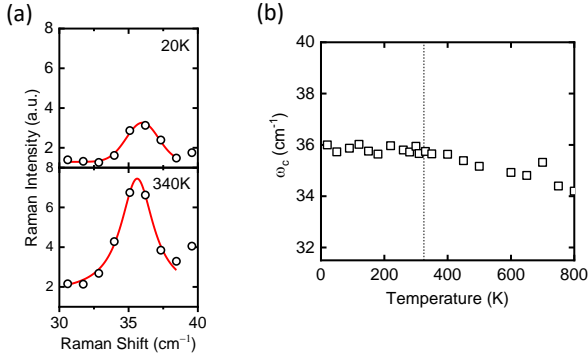


**Figure 5.2.:** (a) The  $A_g$  mode at  $36\text{cm}^{-1}$  below (top) and above (bottom)  $T_c$ . (b) Temperature dependent center of the mode changes. The dashed line marks  $T_c$ .

the same time, they decrease in amplitude. Above  $T_c$ , the  $124\text{ cm}^{-1}$  mode disappears while the  $136\text{ cm}^{-1}$  mode shows up to the highest temperature. Increasing the temperature further shows a slight redshift and broadening of the high-frequency modes. The  $101\text{ cm}^{-1}$  mode above  $T_c$  shows a similar trend. This behavior is in agreement and already known from the previous studies [193].

Here we will focus in particular on the so far unexplored low-frequency response with prominent peaks at  $36\text{cm}^{-1}$  and  $71\text{cm}^{-1}$  below  $T_c$ . The  $36\text{ cm}^{-1}$   $A_g$  mode is a peculiar mode that shows coupling to the excitonic system under strong impulsive excitation and resembles amplitude mode-like behavior [12]. However, the static Raman mode shows no change of width nor a shift in frequency as a function of temperature (Figure 5.2). This stark contrast of equilibrium and the nonequilibrium state indicates that the collective  $A_g$  mode in the nonequilibrium state is a new amplitude mode of a coupled Higgs mode which is absent in equilibrium: The quenched electronic state under the photoexcitation induces a Higgs amplitude mode and that hybridizes with a phonon as discussed in [12].

### 5.1. $A_g$ and $B_{2g}$ low frequency modes and electronic background

At the phase transition, the most remarkable phonon peak is at  $71\text{cm}^{-1}$ . Below  $T_c$ , in the monoclinic phase, shown as the blue spectra (Figure 5.1), barely any change is visible in the  $71\text{cm}^{-1}$ -mode on increasing temperature except for a small redshift on approaching  $T_c$ . Hardly noticeable but already present below  $T_c$  is an asymmetric line shape of the mode with a small spectral weight at the lower energy side of the peak. Above  $T_c$  in the orthorhombic phase, shown in the red spectra, very prominent changes happen. Across the phase transition the mode at  $71\text{cm}^{-1}$  is strongly suppressed and the unknown broad spectral feature becomes visible next to this mode. On further temperature increase in the orthorhombic phase, the broad spectral feature is most prominent between 330 and 400 K before an additional peak

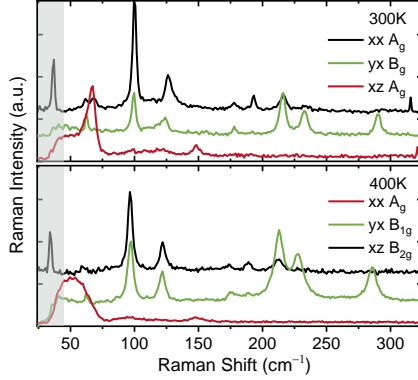


**Figure 5.3.:** Polarized Raman spectra of  $\text{Ta}_2\text{NiSe}_5$  at 300 K (top) and 400K (bottom), representing below and above  $T_c$  respectively. Below and above  $T_c$ , the spectra shows monoclinic irreducible representations  $A_g$ ,  $B_g$  and orthorhombic irreducible representations  $A_g$ ,  $B_{1g}$ ,  $B_{2g}$ , respectively.

appears on top of the broad background and becomes sharper and dominant on increasing temperature. To understand and fully characterize this spectral weight with the mode we map each symmetry channel individually (Figure 5.3). Both key features of the  $71 \text{ cm}^{-1}$ -mode and the broad spectral weight all

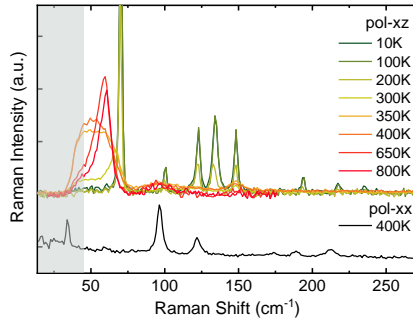


**Figure 5.4.:** Temperature-dependent Raman spectra in the (XZ) geometry probing the  $A_g$  channel below  $T_c$  and the  $B_{2g}$  channel above  $T_c$ . The  $A_g$  channel above  $T_c$  is shown for 400K in (XX) geometry.

appear only in the XZ channel. We plot the temperature dependent spectra of this channel across the whole temperature range of the study in Figure 5.4. Below  $T_c$  (green/yellow spectra), probing the  $A_g$  channel we find the sharp phonon modes at  $71\text{ cm}^{-1}$  and the high frequency modes at  $101, 124, 136, 149, 180, 195\text{ cm}^{-1}$ . On increasing temperature the  $A_g$  modes in the XZ configuration become suppressed and disappear at  $T_c$ . This is as expected for XZ probes in the  $B_{2g}$  channel above  $T_c$ . The  $A_g$  modes remain in the XX configuration at  $400\text{ K}$ , probing the  $A_g$  channel above  $T_c$  (black spectrum). In the  $B_{2g}$  channel of the XZ geometry above  $T_c$  (orange/red spectra) new small modes appear at  $96$  and  $150\text{ cm}^{-1}$ . Most prominent is the appearance of the broad background feature at temperatures up to  $400\text{ K}$  and the additional new peak around  $60\text{ cm}^{-1}$  on further temperature increase.

## 5.2. Characterization of the Raman spectra

In the following, we fit the low-energy Raman spectra with XZ geometry to characterize the interplay of the new peak at the high temperature and the background in the  $B_{2g}$  channel. All phonon modes can be fit using single Gaussian functions. However the broad spectral weight is difficult to fit since it is suppressed below  $45\text{ cm}^{-1}$  by the filter.

Figure 5.5 (a) shows the fit results using Gaussian functions. The  $A_g$  elastic phonon mode at  $70\text{ cm}^{-1}$  (green) is well described with a sharp peak below  $T_c$ . As temperature increases the broad feature (red), labeled "Background" next to the  $A_g$  mode arises. Due to the hump-like feature of the filtered spectra, we use a super-Gaussian function representing a part of the electronic background and the characterization will be discussed later. At  $400\text{ K}$ , a significant additional peak feature  $50\text{ cm}^{-1}$  emerges. As seen in the highest temperature range at  $800\text{ K}$ , it shapes up as a distinct peak feature which can be clearly identified as the  $B_{2g}$  mode.

Approaching  $T_c$  from high temperatures shows that this mode clearly softens from  $60\text{ cm}^{-1}$  to  $52\text{ cm}^{-1}$  and significantly broadens approaching  $T_c$  (Figure 5.5 (b)). Its intensity decreases and disappears at  $T_c$ . We clas-

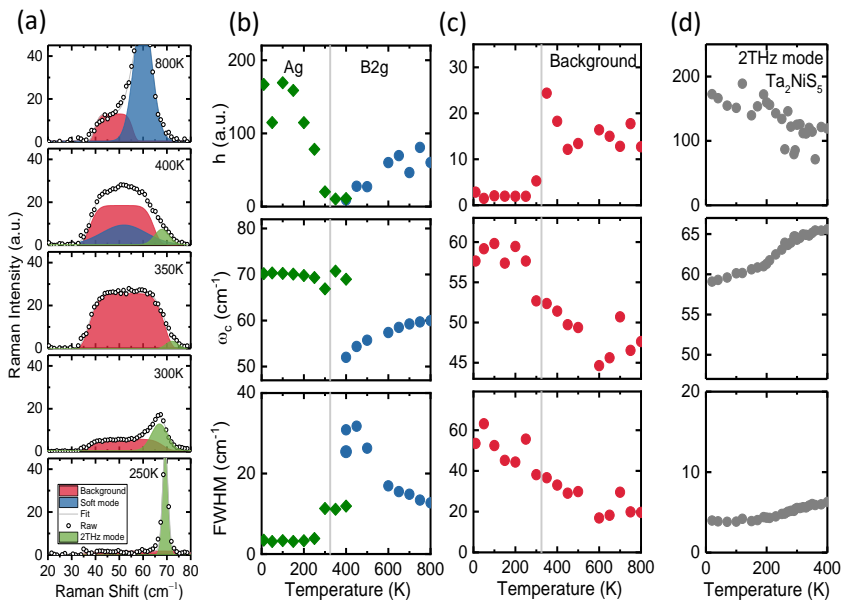


**Figure 5.5.:** (a) Temperature evolution of the low-frequency Raman dynamics of  $\text{Ta}_2\text{NiSe}_5$  with Gaussian fits in the (XZ) channel. Exemplary spectra and extracted parameters of amplitude center frequency and width of the different modes (b)-(d). The key contributions are (b) zone-center  $B_{2g}$  soft phonon mode above  $T_c$  (blue), and  $A_g$  mode (green) interpreted as amplitude modulation of the order parameter deriving from the unstable  $B_{2g}$  mode. In addition (c) a broad spectral weight represents as a part of the electronic continuum [194, 195]. The continuum appears across the phase transition with its intensity becoming dominant at  $T_c$ . For comparison the dynamics of the 2-THz mode in  $\text{Ta}_2\text{NiS}_5$  are given which does not undergo any phase transition (grey) in (d).

sify the mode as the  $B_{2g}$  zone-center optical phonon mode as predicted by Subedi [174]. The inelastic x-ray study [173] did not find this unstable  $B_{2g}$  mode in the range of 328-400K since it already softened and broadened significantly. Also within our data we cannot resolve the mode below 400 K where the mode becomes buried under the strong response of a broad spectral feature that is discussed below. Remarkably, at 400 K, the  $A_g$  mode starts to appear at  $71 \text{ cm}^{-1}$  ( $\sim 2 \text{ THz}$ ) of the monoclinic phase below  $T_c$  (green) where the mode suddenly sharpens at the phase transition. In line with the interpretation of Subedi this new mode in the monoclinic phase corresponds to the amplitude modulation of the order parameter deriving from the unstable  $B_{2g}$  mode of the orthorhombic phase [174]. The most surprising feature in  $\text{Ta}_2\text{NiSe}_5$  is the anomalous electronic continuum component that dominates the weight in the temperature range around the phase transition (red). At very high temperatures, it clearly exists with a strong finite weight next to the soft mode (Figure 5.5 (c)). When cooling below 450 K its weight significantly increases and it becomes the dominant feature approaching  $T_c$ . Then its intensity significantly drops at  $T_c$  but remains comparable to other modes even below  $T_c$ , as seen e.g. at the 300 K data. Only when cooling further down the relative weight decreases further but still finite down to lowest temperatures. As mentioned this feature is fitted by using a super-Gaussian contribution so that it is difficult to assign. Possibilities are fluctuations that are small in the low-temperature ordered phase that significantly increase and peak at  $T_c$  and remain very prominent even for temperatures far above  $T_c$ . To gain additional information on the background feature we have performed the Raman measurement with different excitation conditions. With using high laser power in the Raman experiment, more significant changes appear than using a thermal heater (Figure 5.6). The result reveals that the electronic background is highly susceptible to the heating via laser fluence while the phononic system is not. This observation indicates an electronic or joint electronic-phononic origin of the feature that links to the proposed excitonic fluctuations. Important to note is that the soft mode behavior of the  $B_{2g}$  soft mode does not appear on laser heating. It is either fully buried in the electronic background or is suppressed. This

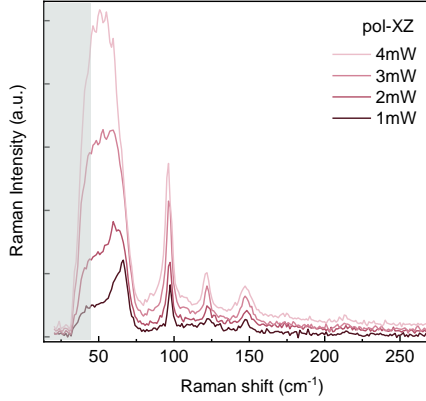


**Figure 5.6.:** Laser dependent low frequency Raman dynamics of  $\text{Ta}_2\text{NiSe}_5$ . Laser power dependent Raman spectra at 300K.

observation points towards the important role of the electronic contribution across the phase transition, that will be further identified by the fit of the sharp mode with electronic background below.

To contrast the soft mode instability and the strong electronic background feature likely jointly driving the phase transition and the appearance of a new mode in the monoclinic low-temperature phase of  $\text{Ta}_2\text{NiSe}_5$ , we show the phonon mode behavior in the sister compound  $\text{Ta}_2\text{NiS}_5$ ; a semiconductor that does neither show an excitonic nor a structural phase transition [148]. Its equivalent 2 THz mode (Figure 5.5 (d), grey) shows a roughly monotonic increase in intensity and only a slight red-shift on cooling across the measured temperature range. Also the mode stays always very sharp in the whole temperature range. Recently, comparable Raman studies showed the lower-energy Raman spectra covered down to  $10\text{cm}^{-1}$  [195, 194]. The low-energy Raman spectra reveal an incipient divergence near  $T_c$ . Since the anomalous feature on the low-energy lineshape is notably asymmetric, they described the line shape with the Fano model. In physics, a Fano resonance is a type of resonant scattering phenomenon that gives rise to an asymmetric lineshape, due to an interference between a background and a resonant

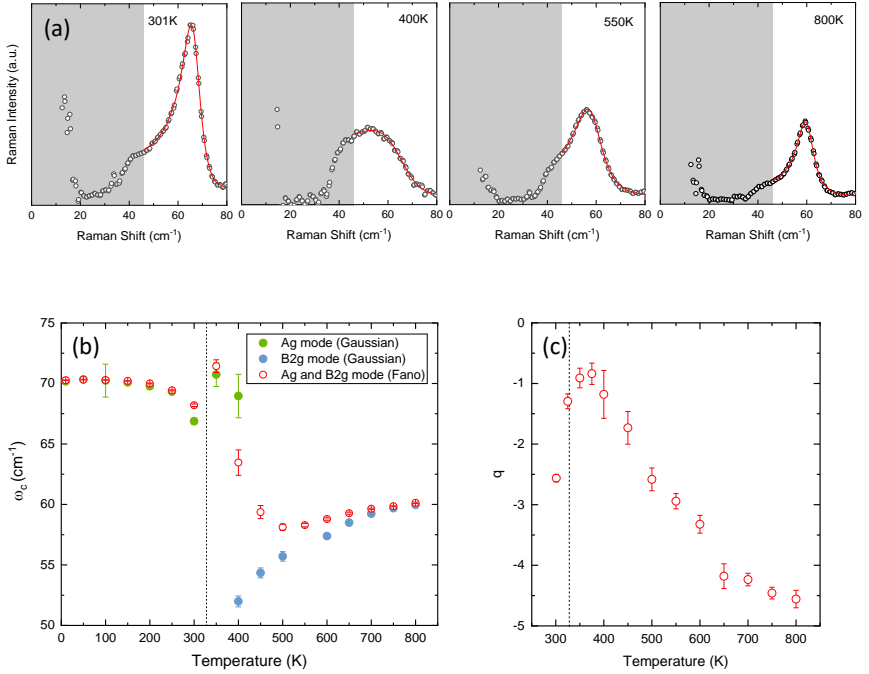


**Figure 5.7.:** (a)  $B_{2g}$  low-energy Raman spectra with the Fano lineshape. (b) Peak energy of the Fano fit as a function of temperature. The error bars represent the standard deviation in the fitting procedure. (c) Fano asymmetry  $q$  extracted from the fitting.

scattering process. They mainly investigated the  $B_{2g}$  optical phonon modes that become significantly asymmetric approaching to  $T_c$  from higher temperature. The incipient divergence towards the zero energy range is suggested as critical fluctuations of the excitonic order parameter give rise to quasi-elastic scattering of  $B_{2g}$  symmetry. The temperature dependent electronic background feature of the Gaussian analysis is comparable to the integrated incipient Raman susceptibility, which shows the cut off at  $T_c$  as temperature changes. If the  $B_{2g}$  phonon adjacent to this fluctuations couples, the phonon mode should be softened, while the phonon would not be affected in the

non-coupled state. To figure out the electron-phonon coupled state, we fit the asymmetric lineshape with a Fano model to demonstrate the entangled state of the electronic background and the optical phonon modes. Figure 5.7 (a) shows the Fano fit of the (XZ) polarization spectrum with Bose-corrected data. At 301 K, below  $T_c$ , the sharp  $A_g$  monoclinic phonon mode is already strongly asymmetric. At 400 K, above  $T_c$ , the mode disappears and the electronic background is dominant. Reaching the temperature above 550 K the  $B_{2g}$  optical phonon mode arises at lower energy than the  $A_g$  mode. As temperature increases up to further higher temperature above  $T_c$  (800 K), the contribution of the electronic background is reduced. The center of the peak extracted from the Fano fit is plotted as a function of temperature (closed black circle in Figure 5.7 (b)). From the highest temperature to 500K, the peak center energy  $\omega_c$  shows softening from  $60 \text{ cm}^{-1}$  to  $58 \text{ cm}^{-1}$ . As cooling the temperature from 500K to  $T_c$ , the peak starts to gain energy abruptly to  $65 \text{ cm}^{-1}$ . Comparably, the Gaussian fit represents a decrease of the  $B_{2g}$  center energy upon  $T_c$  (opened blue circle). Another peak emerges at  $68 \text{ cm}^{-1}$  at around  $T_c$  (opened green circle) that becomes the  $A_g$  mode below  $T_c$ . The  $A_g$  peak behavior below  $T_c$  is consistent in different fit methods, showing gradual hardening of the mode due to the thermal reduction of the lattice. The abrupt blue shift of the Fano coupled  $B_{2g}$  mode below 500 K to  $T_c$  suggests the electronic instabilities as a driving force. That is also evidenced by the Fano asymmetry being more asymmetric as shown by the asymmetric factor  $q \rightarrow 0$  (Figure 5.7 (c)). Therefore, on cooling the temperature from the above, the lattice instabilities emerge as shown in the  $B_{2g}$  mode softening. However, as electronic instabilities are driven, the electronic-phononic coupled state account for the hardening of the Fano peak across the phase transition. The low-temperature monoclinic phase transition happens near the most asymmetric line shape, indicating the strongest electron-phonon coupled state.

Notably, the asymmetry of the  $B_{2g}$  optical phonon mode remains far above  $T_c$ , up to 800 K in our study. It might indicate the electronic instabilities coupled to the  $B_{2g}$  mode far above the gap. One can speculate on a pseudogap in the system above  $T_c$  as observed in the ARPES study [136].

On the other hand, below  $T_c$ , the  $A_g$  mode seems no longer asymmetric. It means that when the phase transition to the monoclinic emerges, the electronic-phononic coupled state disappears. However in any case a strong coupling to the lattice is significantly involved. Therefore, an electronic-driven excitonic insulator transition cannot be fully ruled out.

### 5.3. Summary

We have performed a detailed study on the low-frequency lattice dynamics across the orthorhombic to monoclinic structural phase transition in  $\text{Ta}_2\text{NiSe}_5$ . We can clearly identify the softening of the  $B_{2g}$  zone-center optical phonon mode in the orthorhombic phase above  $T_c$ . This observation underlines a proposed mechanism by Subedi [174] that this instability could act as a prime cause for the structural phase transition, leading to the appearance of a new  $A_g$  mode in the monoclinic phase below  $T_c$ . However, there is an anomalous hardening of the  $B_{2g}$  mode from just above  $T_c$  to  $T_c$ . Interestingly, right in that regime, an asymmetric feature in the low-frequency regime dominates that trace fluctuating joint electronic and structural order that drive the transition.

In analogy to the other comparable studies, the Fano fit indicates that the overdamped excitonic fluctuations maximize at  $T_c$  on decreasing temperature from the above. It is in agreement with other studies in terms of the

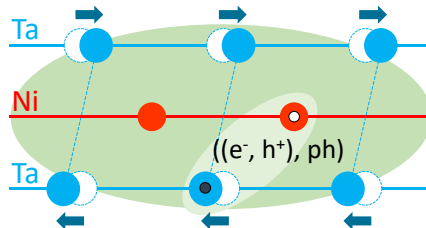


**Figure 5.8.:** Sketch of the charge-transfer exciton with self-localized via exciton dressing with a cloud of phonons. The loss of the mirror symmetry (arrows) drives the semiconductor-excitonic insulator phase transition

excitonic fluctuations near  $T_c$ , however the existence of the  $B_{2g}$  optical zone-center phonon soft mode additionally reveals that the phononic instabilities possibly correlate with the excitonic fluctuations. From this, we conclude that in  $\text{Ta}_2\text{NiSe}_5$  the phase transition is neither purely phononic [190, 184] nor purely or dominant electronic [195, 194, 183] as from contradicting conclusions in various studies. The present study rather points to an interplay of both electronic and structural order. A possible scenario could be self localized exciton polaron complexes as suggested in [147, 196]. Figure 5.8 shows an illustration of the proposed complex. Even though charge-transfer exciton is limited in small radii, it can span to entire crystal due to the exciton-phonon coupling. These may act as natural cavities for the excitonic system. This results in the observed high susceptibility of the electronic system to laser fluence by breaking the excitons and the only weakly affected lattice dynamics of the remaining polaronic distortion. This may also explain some of the contradicting conclusions drawn in the literature on the nature of the excitonic/structural phase transition in  $\text{Ta}_2\text{NiSe}_5$  so far. The clear softening-hardening behavior of the  $B_{2g}$  mode serves an experimental fingerprint describing a jointly driven transition and as a trigger to further theoretical and experimental studies to characterize the electronic and phononic interplay in  $\text{Ta}_2\text{NiSe}_5$ .



# COLLECTIVE EXCITATIONS OF EXCITON-LATTICE COUPLING IN $\text{Ta}_2\text{NiSe}_5$

As discussed in the static Raman spectroscopy in the previous chapter (Chapter 5), an electronic-lattice interplay takes place across the structural and excitonic insulator phase transition in  $\text{Ta}_2\text{NiSe}_5$ . Due to the absence of a charge-density wave (CDW) order in this material, the interaction between electrons (excitons) and lattice are ambiguous. As we will suggest, it can be realized to a new type of state which is a large exciton-phonon complexes spanned the entire crystal termed a polaronic complex. The picture of the large-radius exciton state in this material is in agreement with optical studies [147, 196] and a symmetry selective angle-resolved photoemission spectroscopy (ARPES) study [185].

However, since the electronic and lattice instabilities occur simultaneously, it cannot be disentangled by traditional experimental approaches or first-principles calculations. Here, we report ultrafast melting of the excitonic state

by photoexcitation by means of different probing schemes. We find a new collective mode that will identify as exciton-polaron complex that stabilizes the condensate order in  $\text{Ta}_2\text{NiSe}_5$ . The complex state will be characterized by phononic, electronic and current response using optical pump-probe, time- and angle- resolved photoemission spectroscopy (trARPES) and terahertz (THz) experiments, respectively.

## 6.1. Phononic response of the polaronic complex

To investigate the phononic responses of exciton-polaron complexes, we performed an optical pump-probe study in the excitonic insulator  $\text{Ta}_2\text{NiSe}_5$  below  $T_c$ , using an ultrafast pump laser pulse at 1.5 eV (800nm), 130 fs (see Appendix A.5). For an anisotropic material like  $\text{Ta}_2\text{NiSe}_5$ , which strongly depends on the transition matrix element, laser polarization dependent electronic excitations are expected. Figure 6.1 (a,e) shows the time-dependent photo-induced reflectivity changes ( $\Delta R/R$ ) with different light polarization parallel and perpendicular to the  $a$ -axis of the crystal as a function of pump fluence. The temporal reflectivity shows a superposition of coherent oscillations and the nonoscillatory part of the signal. The latter one represents the electronic contribution, namely the excitation of quasiparticles across the gap and their subsequent recombination. The oscillatory part, in contrast, corresponds to coherent phonons and possibly also collective excitations of the order parameter in the system. Looking at the electronic contribution, the excitation dynamics are highly dependent on the light polarization with respect to the sample orientation. The  $E \parallel a$  scheme shows a large coherent oscillation dominantly at the early pump-probe time delay, (Figure 6.1 (a)), while the  $E \perp a$  configuration shows a clear decaying signal (Figure 6.1 (e)). This strong anisotropy was recently observed by an ARPES study [185] as well. The anisotropy of the material will give rise to different collective oscillations depending on the polarization of the light.

To characterize the coherent oscillations a suitable fit function was applied to model the electronic component (Eq. 3.1). In the fit process, the  $E \parallel a$

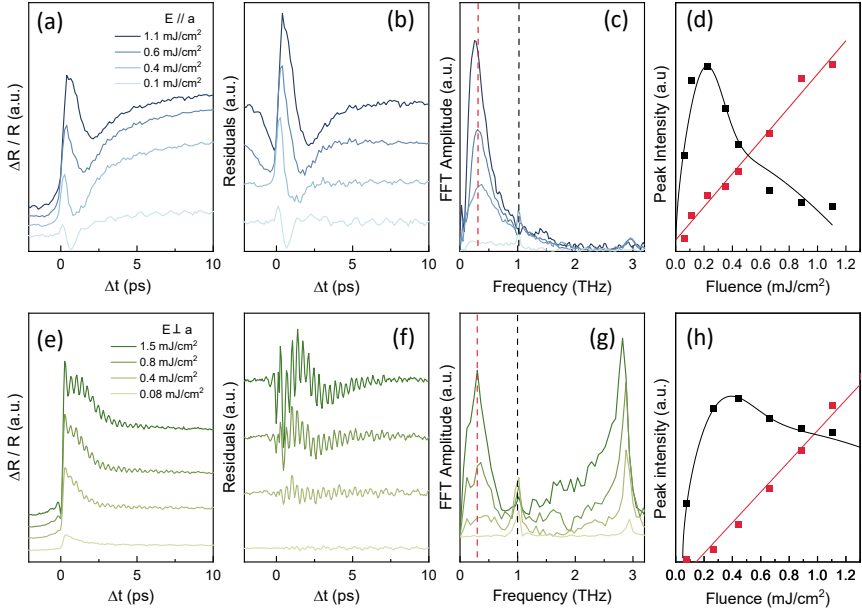


**Figure 6.1.:** Dynamics of the photo-induced change in reflectivity  $\Delta R/R$  in  $\text{Ta}_2\text{NiSe}_5$  single crystal ( $T_c = 328$  K). Pump and probe polarizations are parallel and perpendicular to the  $a$ -axis chain direction in (a-d) and (e-h), respectively. The recorded temperatures are 200 K and 250 K in (a-d) and (e-h), respectively. (a),(e) Temporal evolution of the reflectivity of  $\text{Ta}_2\text{NiSe}_5$  as a function of optical pump fluences. (b),(f) The extracted coherent oscillations by the fits in (a),(e). (c),(g) The corresponding Fourier transform amplitude of the curves shown in panels (b),(f). The red and black dashed lines indicate a new broad phonon mode and a 1-THz phonon mode, respectively. (d),(h) The peak intensity extracted by peak heights of the phonon modes in (c),(g). Red and black solid lines show the linear fit and depletion fit (Eq.6.1) of the new mode and the 1-THz mode, respectively.

scheme was accounted for by the exponential growth instead of the exponential decay as applied in the  $E \perp a$  scheme [61]. Subtracting the measured pump-probe signal by the fit gives the coherent oscillations (Figure 6.1 (b,f)). Interestingly, both experimental configurations show similar coherent oscillations with a quasi-single cycle low frequency transient. One different feature is that the higher frequency components are more clearly seen in the  $E \perp a$  scheme (Figure 6.1 (f)). A Fourier transform of the spectra revealed the collective modes at 0.3, 1, and 3 THz (Figure 6.1 (c,g)). The driven collective modes at 1 and 3 THz were assigned to the  $A_g$  optical phonon mode as shown in the previous chapter 5. In the pump-probe study, the 3-THz phonon mode is prominent in  $E \perp a$  configuration while the other polarization is not, due to the strong anisotropy of the lattice. Comparably, the 1-THz mode emerges in both configurations similarly, in line with its amplitude character of a hybrid Higgs-phonon mode [12]. That is also in agreement with the direct current (dc) resistivity study that showed isotropic charge transport along the  $a$ -axis and  $c$ -axis in the excitonic insulating phase [148].

In the previous pump-probe experiment as shown in Chapter 4 [12], the coherent oscillations were evaluated for long-lived coherent phonon oscillations clearly (grey shade area in Figure A.7). However, an additional feature arises at the early pump-probe time delay. This new phononic response is clearly seen in the single-cycle like signal in the time-domain in both polarization configurations (Figure 6.1 (b,f)) and the broad peak feature at  $\sim 0.3$  THz in the frequency-domain (Figure 6.1 (c,g)). To characterize the appearing coherent oscillation, their amplitude is analyzed as a function of excitation density (Figure 6.1 (d,h)). As reported [12], the 1-THz mode (black square) shows an order parameter characteristic: as the pump fluence increases, the mode intensity increases but decreases above  $0.2 \text{ mJ/cm}^2$  where the exciton condensate starts to deplete. It is well fitted with the convolution of the square-root growth and linear decreases (sold lines),

$$A \cdot (F - F_c)^{1/2} - h \cdot \text{erf}((F - F_c)/\delta F) \cdot (F - F_c) \quad (6.1)$$

where  $A, h$  are constants and  $F_c$  is a critical fluence, representing the deple-

tion of excitonic condensation as a function of pump fluence [12]. Contrarily, the new broad peak increases linearly (red square) in both polarization schemes. It means that the new peak behaves as a typical coherent phonon mode (as same behavior as 3-THz mode [12, 61]). Moreover, the center frequency of the mode decreases from 0.35 THz to 0.25 THz on increasing pump fluence, that is a coherent phonon characteristic [197]. Therefore, the new coherent oscillation is suggested as a phonon mode which is strongly damped. Recently, at the very low frequency regime, a quasi-elastic peak at  $\sim 0.01\text{meV}$  was reported, suggesting an acoustic mode in the system [195, 194]. In the exciton-phonon complex picture, the strongly overlapping exciton complexes span the entire crystal. They propagate as low-energy excitations akin to acoustic phonon modes [147]. Furthermore, a possible phase mode of the condensation was measured by a non-local impulsive Raman experiment [13].

The strongly damped waveform can be understood as the electronic background broadened in the complex state due to the strong coupling to lattice. Therefore, the 0.3-THz mode in the current study is identified as low-energy phonon excitation of an exciton-polaron complex. However, the phononic response alone does not provide a direct access to the complex dynamics. For the full information, its transient electronic response must be probed. To measure the electronic excitations, the transient electronic band structure of the system was observed using trARPES. A coherently excited phonon modulates internuclear distances in the lattice, leading to modulations in the electronic band structure. Therefore, the band dispersion dynamics also allow observing the coherent phonons of a material in addition to the electronic response.

## 6.2. Excitonic gap dynamics

Indeed, the trARPES measurement has revealed the coherent phonon oscillations [184, 182] of  $\text{Ta}_2\text{NiSe}_5$ . As shown in Chapter 4 the recent trARPES experiment revealed the semimetallic phase transition [181, 179].

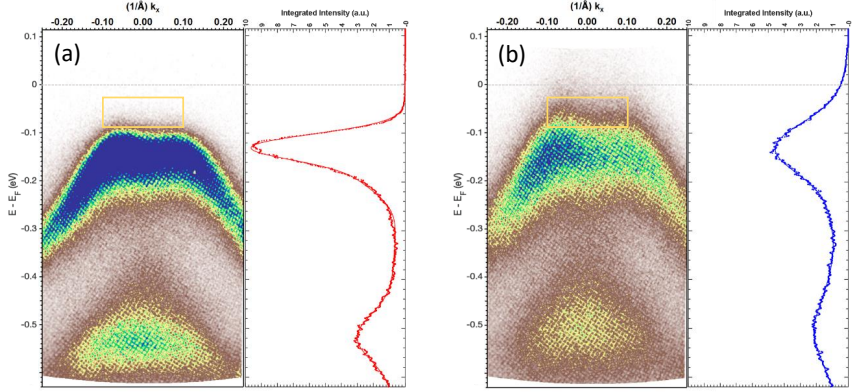


**Figure 6.2.:** Time-resolved transient population of the valence band (VB) at  $\Gamma$  before (a) and after (b) the optical pumping in  $(E - k)$  distribution. The measured temperature is at  $T = 95$  K.

We investigate the relaxation dynamics of the flat top band to observe the collective excitations of the exciton-phonon complex. Since the top valence band (VB) of the excitonic insulator shows the characteristic flat shape 4.2, the transient excitonic state can be directly observed in this range. We perform a trARPES measurement using an infrared laser pulse ( $h\nu = 1.5$  eV) with a pulse duration of 150 fs. Similarly, as in our optical pulse experiments, the pump pulse is polarized parallel to the Ta and Ni chains in this study (experimental details in Appendix A.6). At equilibrium of the excitonic insulating state at 95 K ( $T_c = 328$  K), i.e. without laser excitation, the characteristic flat band of the excitonic insulator shows up in the energy-momentum (Energy ( $E$ ) - momentum ( $k$ )) map (Figure 6.2 (a)), as shown in previous studies [170, 136, 198].

After the pump pulse arrives, the band spectral weight is scattered and pushed into the gap (Figure 6.2 (b)). In other words, two VBs maxima at  $E - E_F \sim -0.16$  eV and  $-0.52$  eV show a massive suppression of photoemission intensity at the photoexcited state  $\Delta t = 0.3$  ps, illustrated clearly by the energy distribution curves (EDC) (red curve in the equilibrium state and

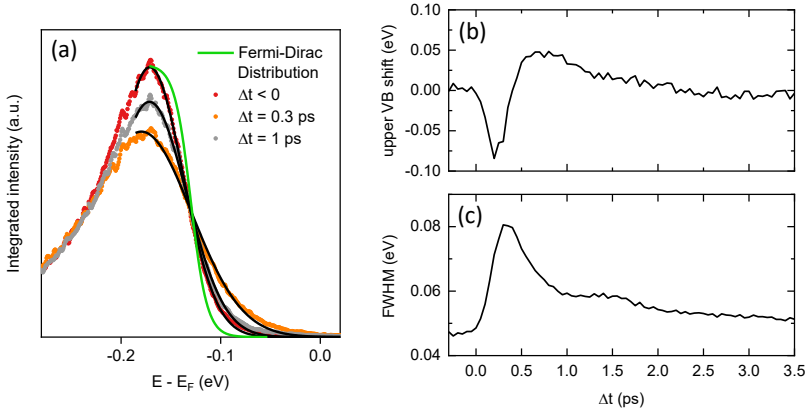


**Figure 6.3.:** Ultrafast upper VB changes at  $\Gamma$ . (a) EDC in integration momentum range at  $[-0.1, 0.1] \text{ \AA}^{-1}$  as a function of pump-probe time delay  $\Delta t$  with a pump fluence  $40 \mu\text{J}/\text{cm}^2$ . The solid lines represent a single Gaussian fit to the data. The time-evolution upper VB shift and a broadening of the band are extracted by the Gaussian fit parameters in (b) and (c) respectively.

blue curve in the nonequilibrium state) integrated at the momentum range of  $[-0.1, 0.1] \text{ \AA}^{-1}$ . For a quantitative analysis of the monitored electronic structure dynamics, specifically near the gap range, the EDCs are fit at various pump-probe time delays with the energy range  $E - E_F$  limited from 0 eV to  $-0.28 \text{ eV}$  (Figure 6.3 (a)). In the equilibrium state the flat band appears as the strongest peak at  $E - E_F \sim -0.16 \text{ eV}$ . When the pump arrives ( $\Delta t = 0.3 \text{ ps}$ ), the flat band collapses and shows a remarkable decrease in peak intensity and broadening. That is well in agreement with previous studies [179, 182] that show semimetallic behavior under photoexcitation.

Further, the band gap at the gamma point seems to be enhanced during the excitation as claimed in ref. [181]. However, as we will show, the gap indeed closes with fills of spectral weight into the gap. To reproduce the previous observation of the putative gap enhancement we fit the EDCs of the flat top VB with a single Gaussian function to extract the VB shifts (solid black line in Figure 6.3 (a)). Figure 6.3 (b) represents the time evolution of the peak position denoting a shift of the VB. At the early pump-probe time

delay, it lowers with  $\sim 80$  meV and relaxes back to the quasi-equilibrium state. Thus, it exhibits a similar gap enhancement behavior as shown in the previous experiment, even though the used the pump fluence is  $\sim 40 \mu\text{J}/\text{cm}^2$  in the current study, which is lower than the previous study [181].

However, the band gap enhancement regarding a rigid band shift must be carefully considered since the band is remarkably broadened. The superior resolution of the current experiment reveals that the flat top VB does not fit well with a single peak function at equilibrium and nonequilibrium states. In fact, the strong exciton-phonon coupling already affects the line shape of the flat top VB at equilibrium. As shown by a green solid line in Figure 6.3 (a), the equilibrium band is significantly broader than the expected Fermi-Dirac distribution. Such a broad band feature occurs due to the electron-phonon coupled state as known by a similar polaron lineshape in cuprates under Franck-Condon broadening [199].

As seen in Figure 6.4 (a), the best fit of the band was applied with two Gaussian peaks which are named Peak 1 (near the Fermi level colored in blue) and peak 2 (at higher energy colored in red). In the nonequilibrium state ( $0 \leq \Delta t$ ), the peak 1 area is clearly suppressed. However, the peak 2 changes are relatively small. The time evolution of the fit properties of the two peaks are plotted in Figure 6.4 (b). The peak 1 area (green curve) is clearly suppressed for  $\sim 0.3$  ps while the peak 2 area (orange curve) shows only a small offset. Due to the suppression of the Peak 1, the maximum of the VB band seems sliding to the peak 2. These joint responses in the VB can not imply the rigid bandgap enhancement as reported in [181].

On the other hand, there is a contradicting study that showed a fill-in spectral weight in the gap [179]. The fill-in spectral weight results the transient semimetallic transition of the material. In analogy to this, we also look into the in-gap state. Figure 6.3 (c) shows the transient width of the flat top VB as a function of pump-probe time delay. The band is broadened and subsequently restored to its quasi-equilibrium value within a couple of picoseconds. We found the fill-in spectral weight in agreement with the semimetallic transition.

Interestingly, the transient VB broadening shows an oscillatory behavior

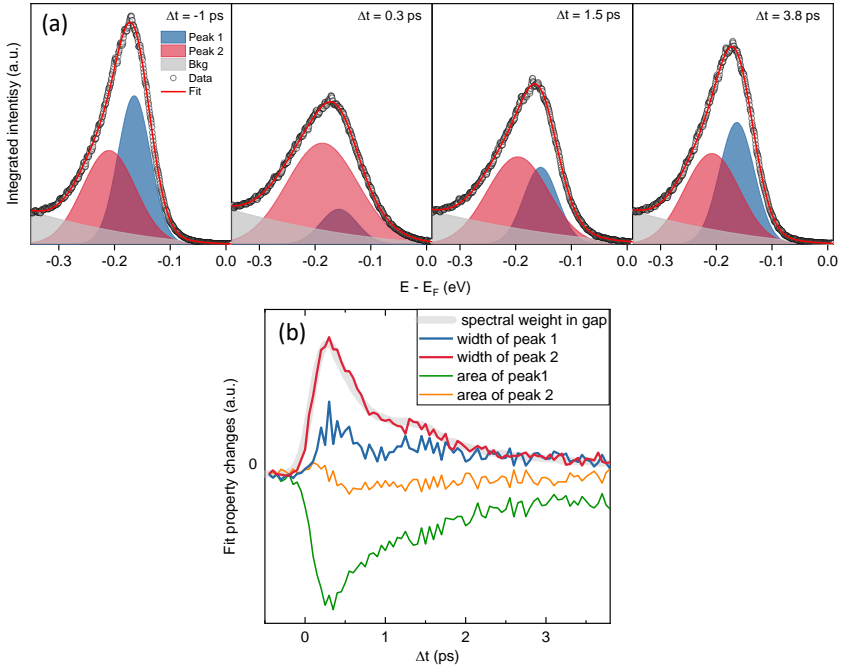


**Figure 6.4.:** Time evolution of EDC spectra at the upper VB with two Gaussian peaks fit. The grey shaded area represents a fixed background with a quadratic function. (b) Time evolution of the area of the two Gaussian peaks in normalized values.

during the recovery time. The period of the oscillation is well in agreement with the transient width of the Peak 1 and the Peak 2 (blue and red curves in Figure 6.4 (b)). Remarkably, the dynamics of the peak 2's width is well overlapped with the dynamics of the VB broadening (grey shaded line in Figure 6.4 (b)). To characterize the gap recovery more quantitatively, we extract the time evolution of in-gap spectral weight (Figure 6.5 (a)) integrating the intensity over an energy window above  $E - E_F = -0.1$  eV and a momentum window range  $[0.1, 0.1] \text{ \AA}^{-1}$  (squared area in Figure 6.2). As shown in the optical pump-probe experiment in the previous section, the different pump fluences are applied to control the depletion of the excitonic condensation. As the pump arrives, the spectral weight in the gap increases for  $\sim 0.3$  ps and

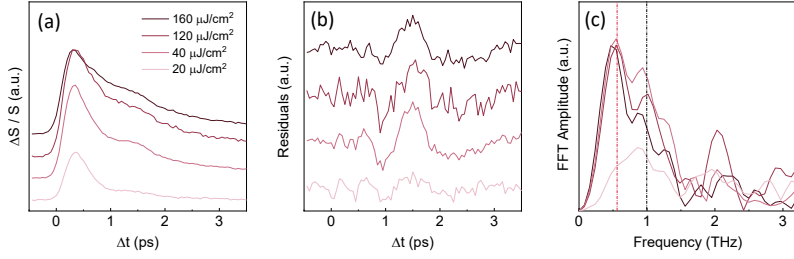


**Figure 6.5.:** Time-resolved transient population of the VB at  $\Gamma$ . (a) Excitation density dependent transient population at the upper VB at  $\Gamma$ . The integrated range is marked with yellow rectangular in Figure 6.2. (b) The populated spectral weight after removing the incoherent background excitation. (c) The corresponding Fourier transform amplitudes of the oscillatory signal of (b).

relaxes back into the quasi-equilibrium state in the shown pump-probe time range. An oscillatory behavior appears on top of the relaxation background dynamics as expected by the broadening of the VB band (Figure 6.3 (c)). The oscillatory signals were extracted by subtracting the non-oscillatory background dynamics. This process can be done by fit of the transient signal with the convolution of Gaussian and exponential decay functions (Eq. 3.1) and the residual of the fit exhibits coherent oscillations only (Figure 6.5 (b)). For all excitation densities, the sub-picosecond quasi-single-cycle oscillations are clearly revealed. Furthermore, amplitudes and phases of the oscillations seem to be similar to each other, except for the smallest excitation density. Applying a Fourier transform shows that frequencies of the oscillations are at 0.5 THz and 1 THz (Figure 6.5 (c)). Since the electronic band dynamics reflect a phononic state as well, the peak at 1 THz can be identified as the  $A_g$  exciton-phonon coupled amplitude mode [12].

However, the peak at 0.5 THz can not be identified as a simple phonon mode since it has not reported in phonon spectra so far [191, 194, 195]. As shown in the time-domain signal (6.5 (b)), the 0.5-THz peak corresponds to the quasi-single cycle waveform with  $\sim 1$  ps duration. This is reminiscent to the phononic mode of the polaronic complex shown in the optical pump-probe study (Section 6.1). Comparably, the shown phononic response

emerges at 0.3 THz. This is not consistent with the peak at 0.5 THz of the electronic band dynamics. By excluding the coherent phonons, the new oscillatory feature can be identified as a coherent charge modulation. If so, the energy difference between the polaronic and electronic coherent dynamics can be realized since the restoring force is higher in electronic than phononic dynamics. Therefore the 0.5-THz electronic modulations would be determined as an electronic response of the exciton-polaron complex. To verify the coherent nature of the signal, we are going to measure an actual electronic response. Probing in THz range would allow for a direct observation of the coherent electronic dynamics revealing a coherent current.

### 6.3. Electronic response of the polaronic complex

Observations of the new transient collective excitations in both the phononic and electronic channel would evidence to the exciton-polaron complex in  $\text{Ta}_2\text{NiSe}_5$ . To substantiate our claim of a coherent current as interpretation of the single-cycle response in trARPES, we are going to directly probe the current response via time resolved THz probes.

Probing the intraband carrier motion as a function of pump-probe time delay can be realized by the 1D pump scan (see Chapter 3). Since the technique provides time-gated detection, it enables probing the changes of selected THz pulse. Thus the measurement provides useful information about the average THz absorption of the sample. The experimental details can be found in Appendix A.7. Figure 6.6 (a) shows the measured THz pulse transmitted through the sample at 40 K without optical excitation. The THz probe polarization is parallel to the Ni-Ta chain direction. After the photoexcitation, the selected THz field (orange dashed line) shows the timescale associated with the onset of photoconductivity and the lifetime of that conductivity (Figure 6.6 (b)).

Remarkably, there is a small oscillatory behavior at the very early pump-probe time delay  $0 \leq \Delta t \leq 2$  ps. This oscillation is extracted by the fit of the excitation-recovery background dynamics (red curve in Figure 6.6

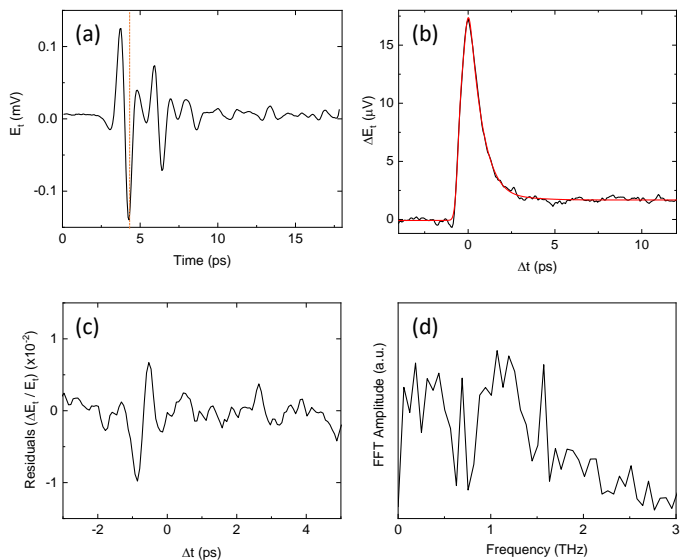


**Figure 6.6.:** Photoinduced change in the transmitted THz electric field in  $\text{Ta}_2\text{NiSe}_5$ . (a) The transient transmitted THz field through the  $\text{Ta}_2\text{NiSe}_5$  at 40 K. (b) The change of the THz field under the photoexcitation where the marked field position with dashed line of (a). The exponential decay fit is represented with red solid line. (c) The extracted coherent oscillation by fit of (b). (d) Corresponding FFT amplitude of coherent oscillation of the transient photoexcited THz field. The probe THz field and optical pump pulse are polarized by parallel and perpendicular to the Ta-Ni chain, respectively. The used pump fluence is  $\sim 0.1 \text{ mJ/cm}^2$ .

(b)). See fit equation 3.1. The residual of the fit (Figure 6.6 (c)) shows a clear quasi-single cycle waveform for  $\sim 1 \text{ ps}$ . Applying the Fourier transform exhibits the corresponding broad bandwidth of the generated THz field up to  $\sim 1.6 \text{ THz}$  (Figure 6.6 (d)). This feature may indicate an existence of coherent current as we expected in polaronic complex in this material.

However, we can not identify the coherent oscillations itself as possibly occurs in processed signals that was extracted by the fits. To confirm the coherent current signal, we performed the experiment in reflection geometry that shows a background free transient signal. Figure 6.7 (a) shows the THz

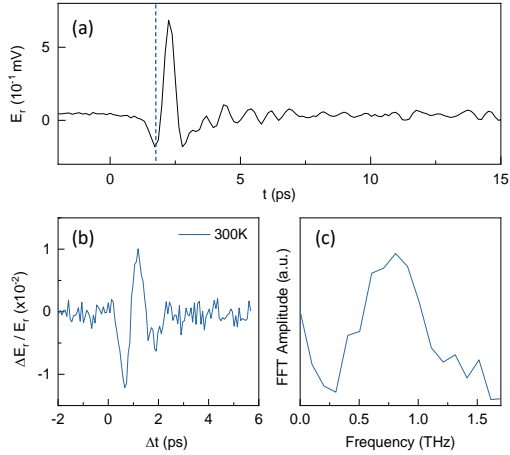


**Figure 6.7.:** Photoinduced change in the reflected THz electric field in  $\text{Ta}_2\text{NiSe}_5$ . (a) The transient reflected THz field through  $\text{Ta}_2\text{NiSe}_5$  at room temperature. (b) The change of the THz field under the photoexcitation, where the dashed line is marked in (a). (c) The corresponding Fourier transform amplitudes of the transient THz field change. The excitation optical pulse fluence is  $0.1 \text{ mJ}/\text{cm}^2$ . A polarization of the THz probe beam and optical pump beam are perpendicular to the Ta-Ni chain.

field reflected by the sample at room temperature. We fixed gate beam to one of the THz peaks (dashed line) that would give the clear change of the THz field  $\Delta R/R$ . After the photoexcitation the time evolution of the reflectivity exhibits a completely background free picosecond single-cycle-like waveform (Figure 6.7 (b)). The generated field in frequency is from 0.3 THz to 1.5 THz (Figure 6.7 (c)). Therefore, we proved the emergence of coherent current in this material in THz reflection configuration. This result indicates that the 1-ps coherent oscillatory feature of electronic band gap dynamics in trARPES experiment is realized as the polaronic current.

## 6.4. Discussion

To emphasize that the resulting signal of the present chapter is indeed a coherent polaronic current, we rule out of the other potential excitations. In

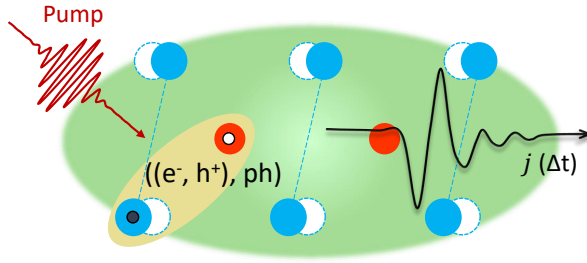


**Figure 6.8.:** Schematic of the coherent current emergence from the polaronic complexes under photoexcitation.

general, a THz pulse could be generated from semiconductor surfaces by other origins such as the optical rectification in the nonlinear medium [200, 201] or the photo-Dember effect [202, 203, 204]. Firstly, we can exclude the optical rectification effect. Since there is no second-order nonlinear susceptibility in the material and the coherent current does not reveal a pump polarization dependency. Secondly, photo-Dember effect cannot be in the role of the current feature. Since electron and hole mobilities of  $\text{Ta}_2\text{NiSe}_5$  are almost equal [205]. We also exclude a photocurrent generation by the Schottky barrier effect induced by the surface bending due to the material's surface or in the depletion area at a metal-semiconductor interface [206]. In our study, the  $\text{Ta}_2\text{NiSe}_5$  crystal is cleaved parallel to the atomic planes, and thus the weak inter-plane electronic coupling strongly reduces the charge transport perpendicular to the surface. If, for instance, a downward surface band bending is developed upon photoexcitation, the whole electronic band structure would transiently shift to higher energy at the sample surface due to the electric field generated by the separation of the charges.

A similar low-energy excitation was introduced in a hybrid metal halide perovskite [193]. The performed time-resolved multi-THz spectroscopy showed the coherent motion of charge carriers correlated with the motion of the polar lattice in a single crystal  $\text{CH}_3\text{NH}_3\text{PbI}_3$ . It results intraband quantum beats arising from the coherent displacement of charges from the coupled phonon cloud. Polarons can be formed on a time scale commensurate with

the longitudinal optical phonon period after band-edge excitation.

In analogy to the polaron study, the coherent current response of  $\text{Ta}_2\text{NiSe}_5$  can be understood with the coupling of charge carriers to a phonon mode. If so, the phonon mode would be the possible low energy excitation of the exciton-polaron complex. In the polaronic complex picture, the strongly overlapped large exciton-phonon complexes spanned the entire crystal can propagate in low-energy excitations akin to acoustic phonon modes [147]. Figure 6.8 shows a schematic of the photoexcitation process in the polaronic complex state of  $\text{Ta}_2\text{NiSe}_5$ . When a pump pulse excites the system, the exciton state is temporally quenched as measured by trARPES. During the recovery, electrons can access the phonon bath, revealing the 1-THz phonon coupled hybrid mode as shown in ref. [12]. Besides, the new collective excitations of the polaronic complex (illustrated in green area) arise with a strongly damped phononic response and coherent charge modulations ( $j(\Delta t)$ ). Notably, the excited charge carriers under the photoexcitation in the excitonic insulator could possibly be not only electrons and holes but also charged excitons (trions).

The observation of the low-energy excitations in  $\text{Ta}_2\text{NiSe}_5$  has not appeared in the other studies so far [207, 195]. To observe this excitations, the early excitation delay time should be taken into account. The key finding of this study is an observation of polaronic current that indicates the existence of an exciton-polaron complex in  $\text{Ta}_2\text{NiSe}_5$ .

Normally free exciton recombination is extremely fast as shown in another excitonic insulator candidate 1T-TiSe<sub>2</sub> with ~20 fs timescale [176]. But here, it seems longer as long as 300-400 ps [179, 184]. This implies a contribution of lattice to the electronic order to stabilize excitons. Here, the polaronic complex is suitable to understand the phenomena: excitons can be stabilized by lattice distortion that may correspond to the shear motion of Ta chains (see atomic displacement in Figure 6.8. In this picture, long-living excitons can span entire crystal and exhibits large radius as examined by optics [147, 196] and ARPES [185] studies. Our results of highly damped phononic response and also electronic response with the emergence of coherent current give an crucial evidence of the polaronic complex in  $\text{Ta}_2\text{NiSe}_5$ .



# CONCLUSIONS

In this thesis, I investigated the collective excitations in quantum materials and their light-induced transient state on ultrafast timescales. Collective behavior in complex quantum materials reveals from cooperative phenomena such as spontaneous symmetry breaking. Probing the dynamics of collective excitation provides important information on the collective quantum state and the dynamics of the ground state.

In particular, I studied two types of quantum materials, high- $T_c$  cuprate superconductor and excitonic insulator. These systems are very close to each other. As like a superconductor is characterized by a condensate of paired electrons, the Cooper pair, stable excitons in a solid state can lead a charge neutral condensate in a so called excitonic insulator.

## **Higgs mode in cuprate superconductors**

Firstly, I investigated the amplitude (Higgs) oscillations of the order parameter in unconventional cuprate high- $T_c$  superconductors. In equilibrium they reveal important information about the nature of the ground state based on the symmetry of the complex order parameter and newly found external couplings of other orders (reported in Chapter 2). In an extension to light driven superconducting states in non-equilibrium I show the transient

properties of the Higgs oscillations on ultrafast timescales and how they give information on the pair-breaking dynamics (reported in Chapter 3).

A key result of the thesis is that it establishes Higgs spectroscopy. That means going beyond the pure observation of the Higgs mode itself but to fully characterize it and use it as a spectroscopic probe for the ground state properties and their dynamics. This can be compared e.g. to the phonon spectroscopy via Raman to gain information on the crystal lattice. Here the Higgs oscillations reveal insight into the condensate of high- $T_c$  superconductivity. Such a direct probe of order parameter dynamics gives us novel and so far unprecedented insights into the multiple unknown mechanisms at play in unconventional superconductors and may help in the future to realize details on the pairing glue.

The Higgs oscillations are more complex for cuprate superconductors than conventional superconductors due to the complex d-wave gap symmetry, particularly its nodes. The existence of non-superconducting quasiparticles on all energy scales leads to strong damping of the Higgs oscillations. Therefore, experimentally I did drive Higgs oscillation using a strong multicycle high-field THz pulse. This leads to a characteristic TH generation due to a resonance of the driving field and the driven Higgs modes. I could show a universal behavior in several families of high- $T_c$  cuprate thin films. In addition to the strong damping of the Higgs mode uncovered a collective mode which is coupled to the superconducting order parameter, a possible pseudogap order above  $T_c$ .

Besides a broad and featureless onset of TH, indicating the driven Higgs oscillations, below  $T_c$  these manifest themselves in a universal jump in the phase of the driven Higgs oscillation. A detailed analysis shows that this phase jump describes an antiresonance of an external, non-damped mode that couples to the heavily damped Higgs mode. The latest measurements (performed already outside the framework of this thesis) hint at a Fano resonance between phonon mediated charge order fluctuations and the Higgs mode itself.

Furthermore, I also revealed a non-vanishing TH response, I above  $T_c$  that extends all the way up to temperatures for which fluctuations due to the

Nernst effect are reported in the normal state [208]. This would indicate a finite pairing amplitude. If so, that may evidence to preformed Cooper pairs without global phase coherence above  $T_c$ . Also it can be a result of enforced phase coherence due to the intense THz field [69]. As proposed pseudogap state in cuprate superconductors, the finite TH field above  $T_c$  may be caused by an unusual form of electron organization such as charge-density wave [40, 93].

As a key extension I have brought Higgs spectroscopy into the time domain to investigate transient states of matter in a proof of principle experiment. I investigated the photoinduced dynamics of pair breaking in a high  $T_c$  cuprate superconductor. I report suppression of the Higgs mode under the photoexcitation with a pump pulse (eV) far above the gap and its amplitude highly dependent on the pump intensity. That points to the pairing amplitude characteristics that manifest the hierarchy of pairing and phase coherence under the photoexcitation [110]. On top of this pair-breaking dynamics sits a complicated interplay of quasiparticles interacting with the superconducting condensate and the pump photons. In the first step towards 2D THz-THG spectroscopy I show ways to disentangle these interactions. A key finding I present is a new feature of coherent response in the linear probe regime that emerges as a driven ac current of the charges in the driving THz field. It opens a way for a THz-eV protocol to generate higher harmonics of the THz light in future studies.

In the future, it will be interesting to prove further the complex interplay of competing or coexisting orders and phases in unconventional superconductors. For that Higgs spectroscopy could be performed under extreme conditions like high magnetic fields, pressure, strain, etc. in order to tune the interplay of complex orders in the cuprates. An additional interesting aspect would be THz Higgs driven modes probed by tr-ARPES to extend Higgs spectroscopy even into momentum space giving rise to multiple Higgs modes depending on the quench symmetry [70]. An application to superconductors of unknown symmetry could benefit by its identification via the Higgs spectrum in this way. As for the transient Higgs spectroscopy a key goal would be proving light induced superconductivity by showing a light induced Higgs

mode. This would be equivalent to a light induced Meissner effect. Besides a pure proof of induced coherence that may also reveal information about the so far unknown mechanism of light induced superconductivity [97, 209, 210].

## **Exciton-lattice coupled state in the excitonic insulator $\text{Ta}_2\text{NiSe}_5$**

On the second complex I extended order parameter studies to the collective dynamics in the potential excitonic insulator  $\text{Ta}_2\text{NiSe}_5$ . An excitonic insulator is a condensate of excitons that may appear in narrow bandwidth semimetals or small band-gap semiconductors if the exciton binding energy exceeds the bandwidth or the band gap of the system [8, 9, 10, 11].

$\text{Ta}_2\text{NiSe}_5$  has been shown as a potential excitonic insulator as evidenced by optics [172, 147, 196], ARPES [136, 170, 185] and resistivity measurements together with the expected phase diagram [148, 173].

However, the origin of the gap is under debate due to a structural phase transition that happens simultaneously at  $T_c$ . Furthermore, even if the excitonic gap is a ground state of this material, it is difficult to understand how excitons can condense at equilibrium since the intrinsic lifetime of the excitons is supposedly too small for them to reach thermal equilibrium. Another important question is how typically small charge transfer excitons present in  $\text{Ta}_2\text{NiSe}_5$  overlap to form a condensate.

Many studies describe the corresponding phase transition as a condensation of excitons breaking a continuous symmetry. This view was challenged recently, pointing out the importance of the loss of two mirror symmetries at a structural phase transition with the semiconductor—excitonic insulator transition [189, 198].

For such a scenario an unstable  $B_{2g}$  optical zone-center phonon at low energy is proposed to drive the transition. To reveal such a soft mode behavior I measured Raman spectroscopy (reported in Chapter 5). This clearly identifies the crucial mode whose energy is softening for temperatures

far above  $T_c$ .

In addition, I found a novel spectral feature, likely of electronic origin, that is distinct from the lattice dynamics and that becomes dominant at  $T_c$ . A joint Fano-fit of the two features phonon and broad electronic background suggests a picture of joint structural and electronic orders driving the phase transition. The phononic softening in this case is not present around  $T_c$  suggesting the excitonic instability as a driver in the transition.

Therefore I conclude that in  $\text{Ta}_2\text{NiSe}_5$  the phase transition is neither purely phononic [198, 184] nor purely or dominant electronic [195, 194, 183] as from contradicting conclusions in various studies.

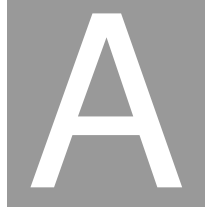
A possible scenario for the joint electronic-phononic state I propose self-localized exciton-polaron complexes, in agreement with the optical response [147, 196]. These may act as natural cavities for the excitonic system resulting in an enhanced lifetime of the excitons and they effectively enlarge the exciton radii so that neighboring exciton-polaron complexes can overlap.

To prove the existence of such exciton-polaron complexes and to investigate the details of the internal interplay of electronic and phononic degrees of freedom one needs to control these separately. Therefore I measured the nonequilibrium behavior of the material by means of a rich set of time-resolved spectroscopic studies (reported in Chapter 6). Intrinsic interactions, more specifically the electron-hole Coulomb attraction and the electron-phonon coupling, are found to govern the ultrafast carrier, exciton and lattice dynamics launched by near-infrared photons.

Most strikingly, in agreement with the proposed scenario above, I found and characterized the ultrafast coherent dynamics of a polaronic complex in  $\text{Ta}_2\text{NiSe}_5$ . Upon photoexcitation impulsive stimulated Raman scattering revealed the coherent phononic dynamics of the complex together with a slow incoherent electronic excitation dynamics (compared to a free electronic response). However, most significantly I measured a picosecond electronic coherent response on top of this electronic dynamics by means of trARPES and THz probe that I can identify as coherent polaronic current.

These results reveal the first proof of a polaronic complex state in  $\text{Ta}_2\text{NiSe}_5$

and solve the mystery on the stabilization of the excitonic state in equilibrium and the overlap of charge transfer like excitons in  $\text{Ta}_2\text{NiSe}_5$ . Based on these results detailed studies on stable excitons and their many-body interactions will become possible and allow microscopic investigations of the excitonic insulator hypothesis in the solid state.



# EXPERIMENTAL METHODS

In this appendix, we summarize the relevant experimental details and methods for the measurements shown in this thesis. Following the order of chapters, we initially introduce a THz-driven nonlinear third harmonic (TH) generation in cuprate superconductors and its extended method adding an optical pump pulse described in Chapter 2 and Chapter 3, respectively. The next part describes the experimental techniques used in the optical excitation of the phononic and electronic dynamics in  $\text{Ta}_2\text{NiSe}_5$ , with a particular focus on optical pump-probe spectroscopy, time- and angle- resolved photoemission spectroscopy and terahertz (THz) time resolved spectroscopy related in Chapter 6. The last part shows the method of Raman spectroscopy reported in Chapter 5.

## A.1. Experimental setup for THz-driven third harmonic generation

For driving Higgs oscillations in our study (Chapter 2), a multicycle, carrier-envelope phase-stable THz source with a narrow bandwidth and high electric field strength was used by the TELBE superradiant undulator source

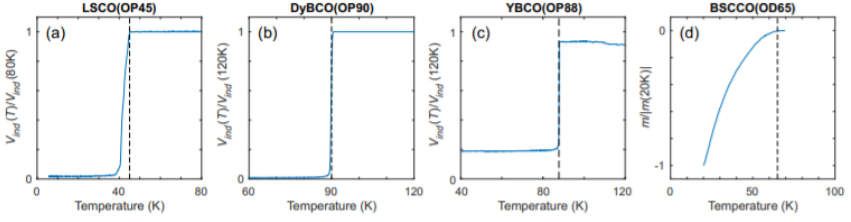


**Figure A.1.:** Experimental determination of  $T_c$  in (a) LSCO (b) DyBCO and (c) YBCO by mutual inductance measurements and in (d) BSCCO by SQUID measurement. The mutual inductance results are normalized to their value above  $T_c$ . In BSCCO, the magnetic moment of the sample starts to drop at  $T_c$ . The drop is normalized to the magnetic moment at 20K. Dotted line indicates  $T_c$ . Figure from [76].

at HZDR [77]. Using this facility, we investigate the TH response of optimally doped  $\text{La}_{1.84}\text{Sr}_{0.16}\text{CuO}_4$  ( $T_c = 45\text{K}$ ),  $\text{DyBa}_2\text{Cu}_3\text{O}_{7-x}$  ( $T_c = 90\text{K}$ ),  $\text{YBa}_2\text{Cu}_3\text{O}_{7-x}$  ( $T_c = 88\text{K}$ ), and overdoped  $\text{Bi}_2\text{Sr}_2\text{CaCu}_2\text{O}_{8+x}$  ( $T_c = 65\text{K}$ ) thin films. The LSCO and DyBCO samples were grown by molecular beam epitaxy (MBE), and the YBCO sample was grown by pulsed laser deposition (PLD) at the Max Planck Institute for Solid State Research. The LSCO sample is 80 nm-thick on a  $\text{LaSrAlO}_4$  (LSAO) substrate. The DyBCO sample is 70 nm-thick on a  $(\text{LaAlO}_3)_{0.3}(\text{Sr}_2\text{TaAlO}_6)_{0.7}$  (LSAT) substrate. The YBCO(OP88) sample is 200 nm-thick on a  $\text{NdGaO}_3$  (NGO) substrate. The BSCCO(OD65) sample was grown by sputtering technique at Laboratoire de Physique des Solides. The BSCCO(OD65) sample is 160 nm thick on a MgO substrate. As shown in Figure A.1,  $T_c$  is determined from mutual inductance measurement for LSCO, DyBCO and YBCO.  $T_c$  of BSCCO is determined from the drop in magnetic moment from SQUID measurement under zero-field cooling. We define  $T_c$  as the onset of the drop in mutual inductance and magnetic moment during cooling. Single crystals of  $\text{Ta}_2\text{NiSe}_5$  were grown by chemical vapor transport reaction described in [148]. Our experiment is performed with 0.7 THz driving frequency, with an electric field up to  $50\text{ kVcm}^{-1}$ . The majority of the data presented in this study are measured using the experimental setup shown in Figure A.2. For fluence dependence measurements, we add an

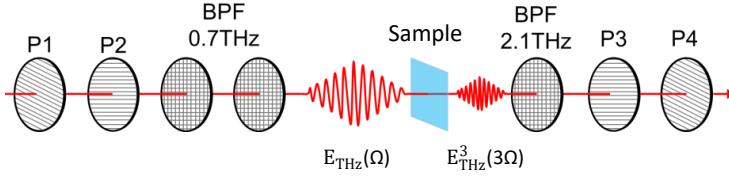


**Figure A.2.:** Schematic illustration of the THz-drive third harmonic (TH) generation. BPF: bandpass filter. Figure from [76]

additional 1.93 THz BPF before P3 to suppress the fundamental harmonic (FH). For temperature dependence of third harmonic (TH) in BSCCO, we also add an additional 1.9 THz BPF before P3. For electro-optical sampling we used a 2 mm ZnTe crystal and 100 fs gate pulse (sampling pulse) with 800 nm central wavelength. Accelerator-based THz pulse and the laser gating pulse have a timing jitter characterized by a standard deviation of 20 fs. Synchronization was achieved through pulse-resolved detection ([211]).

## A.2. Experimental setup for the optical pump-THz drive measurement

We performed near-infrared (NIR) pump-THz drive experiment with THz sources based on a femtosecond laser system. For the former, broadband THz radiation was generated through tilted pulse front scheme utilizing lithium niobate crystal [212, 213, 214]. With initial laser pulse energy around 1.5 mJ at 800 nm central wavelength and 100 fs pulse duration broadband (single-cycle) THz radiation with up to  $3\mu\text{J}$  pulse energy was generated. The spectral distribution of the THz pulses had maximum around 0.7 THz. To reproduce narrow band radiation two BPFs with central frequency of 0.7 THz as same as the schematic of Figure A.2.

In the photoexcitation measurement with a NIR pump pulse, we used two experimental protocols: a one-dimensional (1D) pump scan and a two-dimensional (2D) scan. The 1D scan was performed by fixing the timing of the gate pulse and sweeping the arrival time of the pump pulse (Figure A.3

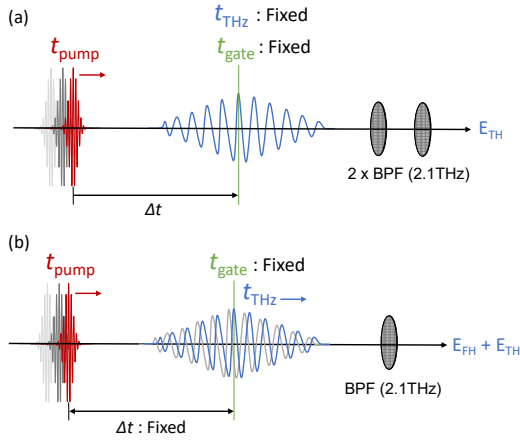


**Figure A.3.:** Experimental scheme for the optical pump-TH drive measurements. (a) a 1D pump scan sweeps the pump pulse  $t_{pump}$  to later times and the delay time  $\Delta t$  is set by the pump and the fixed gate pulse  $t_{gate}$  and THz pulse  $t_{THz}$  spacing. (b) a 2D scan sweeps the pump pulse  $t_{pump}$  and THz pulse  $t_{THz}$  simultaneously while the gap time  $t_{gate}$  is fixed. The pump-probe delay times  $\Delta t$  are obtained by moving the time delay between the pump pulse  $t_{pump}$  and the THz pulse  $t_{THz}$ . BPF: band pass filter.

(a)). To suppress the FH field fully, two BPF with center frequency of TH field (2.1THz) were applied in the THz beam path. In 2D scan measurements (Figure A.3 (b)), time-domain waveforms of THz pulse are obtained by fixing the gate pulse  $t_{gate}$  and sweeping the THz pulse  $t_{THz}$  and the pump pulse  $t_{pump}$ . While the 1D pump scan exhibits the TH dynamics selectively, the full spectrum dynamics can be obtained using the 2D scan technique. To get the full spectrum, a single TH bandpass filter (2.1THz) was used not to suppress all the FH field. Figure A.4 shows the result of the 2D experiment. An excitation feature of 45° to the pump delay time axis  $\Delta t$  indicates the result of the different pump arriving times. On the right, several THz waveforms of selected time delays are shown.

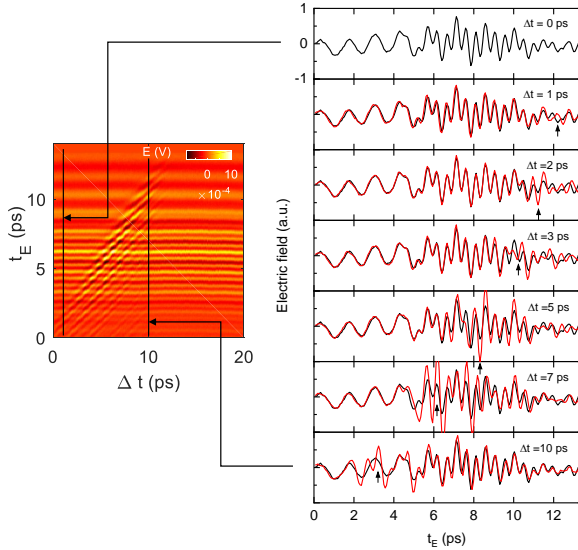


**Figure A.4.:** 2D plot of the observed THz waveforms in the  $(\Delta t, t_E)$  plane (left in the panel).  $\Delta t$  is set by the pump and the gate spacing.  $t_E$  is set by the THz pulse and the gate spacing. On the right panel, THz waveforms of selected pump pulse time delays from  $\Delta t = 0ps$  to  $\Delta t = 10ps$  are shown. The greatest excited position is guided by black arrows.

### A.3. Sample preparation of $Ta_2NiSe_5$

Single crystals of  $Ta_2NiSe_5$  were grown by chemical vapor transport reaction. Elemental powders of Ta, Ni, and Se were mixed with a stoichiometric ratio and sealed into an evacuated quartz tube ( $110^{-3}Pa$ ) with small amount of  $I_2$  as transport agent. The mixture was sintered in a two-zone furnace under a temperature gradient of  $900^\circ/850^\circ C$  for a week. Thin strip-shaped crystals spreading in the  $ac$  plane were grown at the cold end of tube. The crystals were characterized by x-ray diffraction and resistivity measurements.

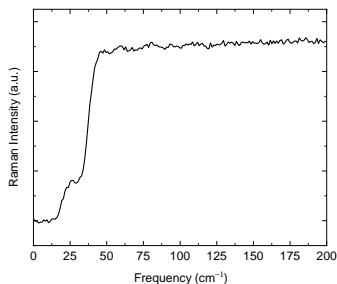


**Figure A.5.:** Raman spectra with a reference sample with a white light lamp.

#### A.4. Raman spectroscopy of $\text{Ta}_2\text{NiSe}_5$

The linear Raman spectrum was measured using a Jobin Yvon Typ V 010 LabRAM single grating spectrometer, equipped with a double super razor edge filter and a Peltier-cooled charge-coupled device camera. The resolution of the spectrometer (grating, 1800 lines/mm) was  $1\text{cm}^{-1}$ . The spectra were taken in a quasi-backscattering geometry using the linearly polarized 632.817-nm line of a He/Ne gas laser. The power was lower than 1 mW, and the spot size was  $20\ \mu\text{m}$ . The scattered signal was filtered and analyzed using an additional polarizer before the spectrometer. The experimental configurations  $Y(XX)\bar{Y}$  and  $Y(XZ)\bar{Y}$  probe only  $A_g$  representations in the monoclinic phase ( $C2/c$ ) and  $A_g$ ,  $B_{2g}$  channel respectively in the orthorhombic phase ( $\text{cmcm}$ ) of  $\text{Ta}_2\text{NiSe}_5$ . The  $Z(YX)\bar{Z}$  configuration accesses the  $B_g$  channel in the monoclinic phase and  $B_{1g}$  channel in the orthorhombic phase. Figure A.5 is a Raman spectra of a reference sample simulated underground by a white light lamp. The instrumental frequency filter at the low frequency suppressed the Raman spectra below  $47\text{cm}^{-1}$  as shown in Chapter 5.

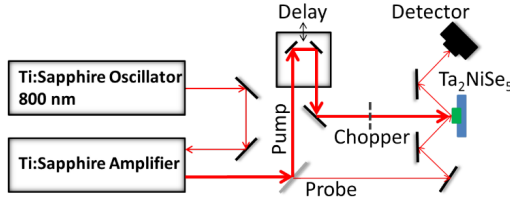


**Figure A.6.:** Experimental setup: Pulses from an oscillator were amplified in a regenerative amplifier. The amplified pulses were divided into a pump and probe beams. The time delay between the pulses was varied using a stage. The reflection of the probe beam from the sample was aligned into a diode. The pump beam was modulated by a chopper and the pump induced reflectivity changes were measured with a lock-in amplifier. Figure from [61].

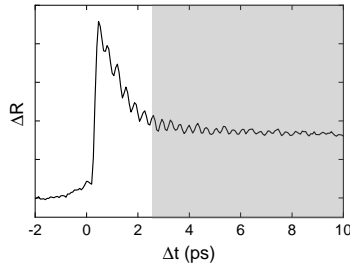


**Figure A.7.:** Transient reflectivity change in  $\text{Ta}_2\text{NiSe}_5$  at 300K. The polarization is perpendicular to the  $a$ -axis of the crystal. The grey shaded area indicates the fast Fourier transform (FFT) range for a coherent phonon analysis [61].

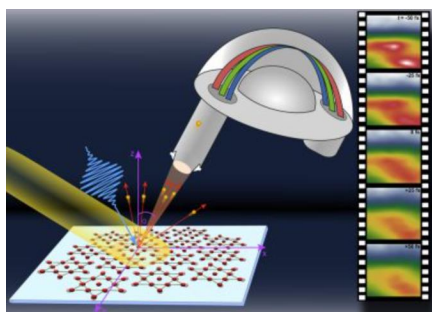
## A.5. Near-infrared pump-probe experiment

Figure A.6 shows a scheme of the setup of near-infrared pump-probe measurement of  $\text{Ta}_2\text{NiSe}_5$  (Chapter 6). A regenerative Ti:Sa amplifier delivering  $6 \mu\text{J}$  pulses at 800 nm with a pulse duration of 130 fs was used as a source. The time-resolved reflectivity changes were measured in a degenerate pump-probe experiment at this wavelength. The pump was attenuated to obtain the desired excitation density. The size of the pump spot was 300  $\mu\text{m}$ , and excitation densities of up to  $1.6 \text{ mJ}/\text{cm}^2$  were used. Higher excitation densities irreversibly damaged the samples. Systematic temperature and

excitation density dependent measurements were carried out on the sample at both perpendicular and parallel polarization to the Ta-Ni chains of the system (Figure 4.6). The measured optical pump-probe is shown in Figure A.7. While the coherent phonon oscillations are long-lived and thus analysed with FFT at quasi-stable state (grey shaded area), a polaronic dynamics is clearly seen at the beginning of the excitation (no shaded area) as shown in this thesis. More details about the experimental setup can be found in [61].

## A.6. Time- and angle- resolved photoemission experiment

The time-resolved ARPES (trARPES) measurements were performed at the UBC-Moore Center for Ultrafast Quantum Matter. A regenerative Ti:Sa amplifier delivering  $6 \mu\text{J}$  pulses at 800 nm was used as a source. The UV probe (6.2 eV) beam is generated through a cascade of nonlinear processes. The trARPES measurements are conducted in an ultrahigh vacuum with a base pressure lower than  $5 \times 10^{-11}$  torr, at a base temperature of 95 K. Both pump and probe beams were polarized parallel to the Ta-Ni chain direction, and the overall time, and energy, resolution of the system were 250 fs, and 11 meV, respectively. The more detail of the system can be found in ref. [110].



**Figure A.8.:** Principle scheme of the trARPES experiment. Photoemission maps are recorded at different temporal delays between the femtosecond pump and probe laser pulse. From this image series pump-probe correlation traces for each pixel can be extracted. Figure by Jörg M Harms / MPSD Hamburg.

## A.7. Time-domain THz spectroscopy

The optical pump-THz probe experiment in this study (Chapter 6) was performed in both reflection and transmission geometry as sketched in Figure A.9. The optical pump-THz probe measurements were performed in a high-sensitivity pump-THz probe setup utilizing a 250 KHz regenerative Ti:sapphire amplifier, with a pulse duration  $\sim 150$  fs at 800 nm (1.5 eV). The light source is split to an optical pump and the THz-time domain spectroscopy setup. In the THz setup, the beam is split again into a THz generation and a probe beam. The phase-locked THz pulses are generated by a large-area LT-GaAs-based photoconductive emitter with spectrum 0.2-2.5 THz range. The THz pulse can be detected by the delayed probe beam (adjusted by beam path length) through an electro-optic sampling in a nonlinear crystal (ZnTe crystal in this study).

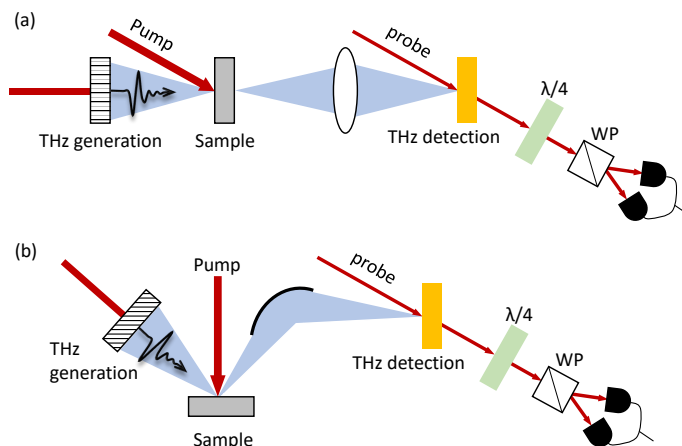


**Figure A.9.:** Experimental scheme for the optical pump-TH probe measurement in (a) transmission geometry and (b) reflection geometry. Red lines represent light at 800 nm (1.55 eV) and the THz light is colored in blue. Cigar shape in (a) represents a lens and the black arc in (b) is a parabolic mirror. The rectangular with black grid is a THz generation material, a large-area LT-GaAs-based photoconductive emitter in our study. Orange colored rectangular is a THz detection material, ZnTe crystal in our study. Semicirculars with black colored represent photodiodes.  $\lambda/4$ : Quarter waveplat, WP: Wollaston prism.

# BIBLIOGRAPHY

- [1] L. N. Cooper. ‘Bound Electron Pairs in a Degenerate Fermi Gas’. *Physical Review* 104.4 (Nov. 1956), pp. 1189–1190. URL: <https://link.aps.org/doi/10.1103/PhysRev.104.1189> (cit. on p. 13).
- [2] J. Bardeen et al. ‘Theory of Superconductivity’. *Physical Review* 108.5 (Dec. 1957), pp. 1175–1204. URL: <https://link.aps.org/doi/10.1103/PhysRev.108.1175> (cit. on pp. 13, 26).
- [3] J. Bardeen et al. ‘Microscopic Theory of Superconductivity’. *Physical Review* 106.1 (Apr. 1957), pp. 162–164. URL: <https://link.aps.org/doi/10.1103/PhysRev.106.162> (cit. on pp. 13, 26).
- [4] A. Beekman et al. ‘An introduction to spontaneous symmetry breaking’. *SciPost Physics Lecture Notes* (Dec. 2019), p. 11. URL: <https://scipost.org/10.21468/SciPostPhysLectNotes.11> (cit. on p. 13).
- [5] R. Matsunaga et al. ‘Higgs amplitude mode in the bcs superconductors Nb<sub>1-x</sub>Ti<sub>x</sub>N induced by terahertz pulse excitation’. *Physical Review Letters* 111.5 (July 2013) (cit. on pp. 14, 34, 35).
- [6] R. Matsunaga et al. ‘Light-induced collective pseudospin precession resonating with Higgs mode in a superconductor’. *Science* 345.6201 (Sept. 2014), p. 1145. URL: <http://science.sciencemag.org/content/345/6201/1145.abstract> (cit. on pp. 14, 29, 36–38).
- [7] ‘Das Higgs-Teilchen und die Supraleitung Neue Form der Spektroskopie liefert Erkenntnisse für die Entwicklung von widerstandslosen Stromtransportern bei Raumtemperatur’ (2020), pp. 1–4 (cit. on p. 15).

- [8] D. Jérôme et al. ‘Excitonic Insulator’. *Physical Review* 158.2 (June 1967) (cit. on pp. 16, 81, 85, 132).
- [9] N. F. Mott. ‘The transition to the metallic state’. *Philosophical Magazine* 6.62 (1961), pp. 287–309 (cit. on pp. 16, 81, 132).
- [10] R. S. Knox. ‘Solid state physics, suppl. 5: Theory of excitons’. *New York : Academic Press* (1963) (cit. on pp. 16, 81, 132).
- [11] Keldysh L. V. et al. ‘Possible instability of semimetallic state toward Coulomb interaction’. *Sov. Phys. – Solid State* 6.9 (1965), p. 2219 (cit. on pp. 16, 81, 132).
- [12] D. Werdehausen et al. *Coherent order parameter oscillations in the ground state of the excitonic insulator Ta<sub>2</sub>NiSe<sub>5</sub>*. Tech. rep. 2018. URL: <http://advances.sciencemag.org/> (cit. on pp. 17, 55, 95, 96, 98, 102, 116, 117, 122, 127).
- [13] H. M. Bretscher et al. ‘Imaging the coherent propagation of collective modes in the excitonic insulator Ta<sub>2</sub>NiSe<sub>5</sub> at room temperature’. *Science Advances* 7.28 (2021) (cit. on pp. 17, 97, 117).
- [14] S. Chatrchyan et al. ‘Observation of a new boson at a mass of 125 GeV with the CMS experiment at the LHC’. *Physics Letters B* 716.1 (2012), pp. 30–61. URL: <https://www.sciencedirect.com/science/article/pii/S0370269312008581> (cit. on pp. 19, 25).
- [15] G. Aad et al. ‘Observation of a new particle in the search for the Standard Model Higgs boson with the ATLAS detector at the LHC’. *Physics Letters B* 716.1 (2012), pp. 1–29. URL: <https://www.sciencedirect.com/science/article/pii/S037026931200857X> (cit. on pp. 19, 25).
- [16] Y. Nambu. ‘Quasi-Particles and Gauge Invariance in the Theory of Superconductivity’. *Physical Review* 117.3 (Feb. 1960) (cit. on pp. 19, 25).
- [17] P. W. Anderson. ‘Random-Phase Approximation in the Theory of Superconductivity’. *Physical Review* 112.6 (Dec. 1958), pp. 1900–1916. URL: <https://link.aps.org/doi/10.1103/PhysRev.112.1900> (cit. on pp. 19, 23, 25, 26, 37).

- [18] Y. Nambu et al. ‘Dynamical Model of Elementary Particles Based on an Analogy with Superconductivity. I’. *Physical Review* 122.1 (Apr. 1961), pp. 345–358. URL: <https://link.aps.org/doi/10.1103/PhysRev.122.345> (cit. on p. 20).
- [19] P. W. Anderson. ‘Plasmons, Gauge Invariance, and Mass’. *Physical Review* 130.1 (Apr. 1963), pp. 439–442. URL: <https://link.aps.org/doi/10.1103/PhysRev.130.439> (cit. on pp. 20, 25).
- [20] P. B. Littlewood et al. ‘Amplitude collective modes in superconductors and their coupling to charge-density waves’. *Physical Review B* 26.9 (Nov. 1982), pp. 4883–4893. URL: <https://link.aps.org/doi/10.1103/PhysRevB.26.4883> (cit. on pp. 20, 23, 32, 51).
- [21] P. W. Anderson. ‘Higgs, Anderson and all that’. *Nature Physics* 11.2 (Feb. 2015), pp. 93–93. URL: <http://www.nature.com/articles/nphys3247> (cit. on p. 20).
- [22] R. Shimano et al. ‘Higgs Mode in Superconductors’. *The Annual Review of Condensed Matter Physics is Annu. Rev. Condens. Matter Phys.* 2020 11 (2020), pp. 103–124. URL: <https://doi.org/10.1146/annurev-conmatphys-> (cit. on pp. 20, 31).
- [23] D. Pekker et al. ‘Amplitude/higgs modes in condensed matter physics’. *Annual Review of Condensed Matter Physics* 6.1 (2015), pp. 269–297 (cit. on pp. 20, 24, 44).
- [24] R. Sooryakumar et al. ‘Raman Scattering by Superconducting-Gap Excitations and Their Coupling to Charge-Density Waves’. *Physical Review Letters* 45.8 (Aug. 1980), pp. 660–662. URL: <https://link.aps.org/doi/10.1103/PhysRevLett.45.660> (cit. on pp. 21, 32).
- [25] R. Sooryakumar et al. ‘Raman scattering from superconducting gap excitations in the presence of a magnetic field’. *Physical Review B* 23.7 (Apr. 1981), pp. 3213–3221. URL: <https://link.aps.org/doi/10.1103/PhysRevB.23.3213> (cit. on pp. 21, 32).
- [26] M. Tinkham. *Introduction to Superconductivity*. Dover Books on Physics Series. Dover Publications, 2004 (cit. on p. 21).

- [27] M. Cyrot. ‘Ginzburg-Landau theory for superconductors’. *Reports on Progress in Physics* 36.2 (Feb. 1973), pp. 103–158. URL: <https://iopscience.iop.org/article/10.1088/0034-4885/36/2/001> (cit. on p. 21).
- [28] A. F. Volkov et al. ‘Collisionless relaxation of the energy gap in superconductors’. *Zh. Eksp. Teor. Fiz.* 65 (1973), p. 2038 (cit. on p. 23).
- [29] I. O. Kulik et al. ‘Pair susceptibility and mode propagation in superconductors: A microscopic approach’. *Journal of Low Temperature Physics* 43.5-6 (June 1981), pp. 591–620. URL: <http://link.springer.com/10.1007/BF00115617> (cit. on p. 23).
- [30] P. B. Littlewood et al. ‘Gauge-Invariant Theory of the Dynamical Interaction of Charge Density Waves and Superconductivity’. *Physical Review Letters* 47.11 (Sept. 1981), pp. 811–814. URL: <https://link.aps.org/doi/10.1103/PhysRevLett.47.811> (cit. on pp. 23, 32).
- [31] Y. Nambu. ‘Fermion-Boson relations in BCS-type theories’. *Physica D: Nonlinear Phenomena* 15.1-2 (Feb. 1985), pp. 147–151. URL: <https://linkinghub.elsevier.com/retrieve/pii/0167278985901575> (cit. on pp. 23, 26).
- [32] E. Abrahams et al. ‘Time Variation of the Ginzburg-Landau Order Parameter’. *Physical Review* 152.1 (Dec. 1966), pp. 416–432. URL: <https://link.aps.org/doi/10.1103/PhysRev.152.416> (cit. on p. 24).
- [33] A. Schmid. ‘A Time Dependent Ginzburg-Landau Equation and its Application to the Problem of Resistivity in the Mixed State’. *Phys. Kond. Mater.* 5 (1966), p. 302 (cit. on p. 24).
- [34] C. Caroli et al. ‘Fluctuations of the Order Parameter in Type-II Superconductors. I. Dirty Limit’. *Physical Review* 159.2 (July 1967), pp. 306–315. URL: <https://link.aps.org/doi/10.1103/PhysRev.159.306> (cit. on p. 24).
- [35] H. Ebisawa et al. ‘Wave Character of the Time Dependent Ginzburg Landau Equation and the Fluctuating Pair Propagator in Superconductors’. *Progress of Theoretical Physics* 46.4 (Oct. 1971), pp. 1042–1053. URL: <https://academic.oup.com/ptp/article-lookup/doi/10.1143/PTP.46.1042> (cit. on p. 24).

- [36] C. A. R. Sá de Melo et al. ‘Crossover from BCS to Bose superconductivity: Transition temperature and time-dependent Ginzburg-Landau theory’. *Physical Review Letters* 71.19 (Nov. 1993), pp. 3202–3205. URL: <https://link.aps.org/doi/10.1103/PhysRevLett.71.3202> (cit. on p. 24).
- [37] C.M.Varma. ‘Higgs Boson in Superconductors’. *Journal of Low Temperature Physics* 126 (2002), p. 901 (cit. on p. 24).
- [38] S. Tsuchiya et al. ‘Higgs mode in a superfluid of Dirac fermions’. *Physical Review B* 88.1 (July 2013), p. 014527. URL: <https://link.aps.org/doi/10.1103/PhysRevB.88.014527> (cit. on p. 24).
- [39] J.R. Engelbrecht et al. ‘BCS to Bose crossover: Broken-symmetry state’. *Physical Review B* 55.22 (June 1997), pp. 15153–15156. URL: <https://link.aps.org/doi/10.1103/PhysRevB.55.15153> (cit. on p. 24).
- [40] T. Cea et al. ‘Nonrelativistic Dynamics of the Amplitude (Higgs) Mode in Superconductors’. *Physical Review Letters* 115.15 (Oct. 2015), p. 157002. URL: <https://link.aps.org/doi/10.1103/PhysRevLett.115.157002> (cit. on pp. 24, 55, 131).
- [41] F. Englert et al. ‘Broken Symmetry and the Mass of Gauge Vector Mesons’. *Physical Review Letters* 13.9 (Aug. 1964), pp. 321–323. URL: <https://link.aps.org/doi/10.1103/PhysRevLett.13.321> (cit. on p. 25).
- [42] P. W. Higgs. ‘Broken Symmetries and the Masses of Gauge Bosons’. *Physical Review Letters* 13.16 (Oct. 1964), pp. 508–509. URL: <https://link.aps.org/doi/10.1103/PhysRevLett.13.508> (cit. on p. 25).
- [43] P. Higgs. ‘Broken symmetries, massless particles and gauge fields’. *Physics Letters* 12.2 (Sept. 1964), pp. 132–133. URL: <https://linkinghub.elsevier.com/retrieve/pii/0031916364911369> (cit. on p. 25).
- [44] G. E. Volovik et al. ‘Nambu sum rule and the relation between the masses of composite Higgs bosons’. *Physical Review D* 87.7 (Apr. 2013), p. 075016. URL: <https://link.aps.org/doi/10.1103/PhysRevD.87.075016> (cit. on p. 26).
- [45] N. Tsuji et al. ‘Theory of Anderson pseudospin resonance with Higgs mode in superconductors’. *Physical Review B - Condensed Matter and Materials Physics* 92.6 (Aug. 2015) (cit. on pp. 26, 35, 51, 54).

- [46] K. E. Kihlstrom et al. ‘Tunneling  $\alpha$   $2 F(\omega)$  from sputtered thin-film NbN’. *Physical Review B* 32.3 (Aug. 1985), pp. 1843–1845. URL: <https://link.aps.org/doi/10.1103/PhysRevB.32.1843> (cit. on p. 31).
- [47] S. D. Brorson et al. ‘Femtosecond room-temperature measurement of the electron-phonon coupling constant  $\gamma$  in metallic superconductors’. *Physical Review Letters* 64.18 (Apr. 1990), pp. 2172–2175. URL: <https://link.aps.org/doi/10.1103/PhysRevLett.64.2172> (cit. on p. 31).
- [48] S. P. Chockalingam et al. ‘Superconducting properties and Hall effect of epitaxial NbN thin films’. *Physical Review B* 77.21 (June 2008), p. 214503. URL: <https://link.aps.org/doi/10.1103/PhysRevB.77.214503> (cit. on p. 31).
- [49] H. Aoki et al. ‘Nonequilibrium dynamical mean-field theory and its applications’. *Reviews of Modern Physics* 86.2 (June 2014), pp. 779–837. URL: <https://link.aps.org/doi/10.1103/RevModPhys.86.779> (cit. on p. 31).
- [50] N. Tsuji et al. ‘Nonlinear light–Higgs coupling in superconductors beyond BCS: Effects of the retarded phonon-mediated interaction’. *Physical Review B* 94.22 (Dec. 2016), p. 224519. URL: <https://link.aps.org/doi/10.1103/PhysRevB.94.224519> (cit. on pp. 31, 38, 68).
- [51] T. Jujo. ‘Two-Photon Absorption by Impurity Scattering and Amplitude Mode in Conventional Superconductors’. *Journal of the Physical Society of Japan* 84.11 (Nov. 2015), p. 114711. URL: <https://journals.jps.jp/doi/10.7566/JPSJ.84.114711> (cit. on pp. 31, 38, 68).
- [52] Y. Murotani et al. ‘Nonlinear optical response of collective modes in multiband superconductors assisted by nonmagnetic impurities’. *Physical Review B* 99.22 (June 2019), p. 224510. URL: <https://link.aps.org/doi/10.1103/PhysRevB.99.224510> (cit. on pp. 31, 38, 68).
- [53] M. Silaev. ‘Nonlinear electromagnetic response and Higgs-mode excitation in BCS superconductors with impurities’. *Physical Review B* 99.22 (June 2019), p. 224511. URL: <https://link.aps.org/doi/10.1103/PhysRevB.99.224511> (cit. on pp. 31, 38, 68).
- [54] R. Haenel et al. ‘Time-resolved optical conductivity and Higgs oscillations in two-band dirty superconductors’ (Dec. 2020). URL: <http://arxiv.org/abs/2012.07674> (cit. on p. 31).

- [55] N. Tsuji et al. ‘Higgs-mode resonance in third harmonic generation in NbN superconductors: Multiband electron-phonon coupling, impurity scattering, and polarization-angle dependence’. *Physical Review Research* 2.4 (Oct. 2020), p. 043029. URL: <https://link.aps.org/doi/10.1103/PhysRevResearch.2.043029> (cit. on pp. 31, 38, 68).
- [56] L. Schwarz. *Higgs Spectroscopy of Superconductors in Nonequilibrium*. Tech. rep. (cit. on p. 31).
- [57] R. Grasset et al. ‘Higgs-mode radiance and charge-density-wave order in 2H-NbSe<sub>2</sub>’. *Physical Review B* 97.9 (Mar. 2018), p. 094502. URL: <https://link.aps.org/doi/10.1103/PhysRevB.97.094502> (cit. on p. 32).
- [58] M.-A. Méasson et al. ‘Amplitude Higgs mode in the 2 H NbSe 2 superconductor’. *Physical Review B* 89.6 (Feb. 2014), p. 060503. URL: <https://link.aps.org/doi/10.1103/PhysRevB.89.060503> (cit. on p. 32).
- [59] R. Grasset et al. ‘Pressure-Induced Collapse of the Charge Density Wave and Higgs Mode Visibility in 2H-TaS<sub>2</sub>’. *Physical Review Letters* 122.12 (Mar. 2019), p. 127001. URL: <https://link.aps.org/doi/10.1103/PhysRevLett.122.127001> (cit. on pp. 32, 51).
- [60] A. F. Volkov et al. ‘Collisionless relaxation of the energy gap in superconductors’. *Soviet Journal of Experimental and Theoretical Physics* 38 (May 1974), p. 1018 (cit. on p. 33).
- [61] D. Werdehausen et al. *Nonequilibrium Higgs-Phonon Coupling in the Excitonic Insulator Ta 2 NiSe 5*. Tech. rep. 2016 (cit. on pp. 33, 70, 116, 117, 141, 142).
- [62] T. E. Stevens et al. ‘Coherent phonon generation and the two stimulated Raman tensors’. *Physical Review B* 65.14 (Mar. 2002), p. 144304. URL: <https://link.aps.org/doi/10.1103/PhysRevB.65.144304> (cit. on p. 34).
- [63] T. Papenkort et al. ‘Coherent dynamics and pump-probe spectra of BCS superconductors’. *Physical Review B - Condensed Matter and Materials Physics* 76.22 (Dec. 2007) (cit. on p. 35).
- [64] R. Matsunaga et al. ‘Nonequilibrium BCS State Dynamics Induced by Intense Terahertz Pulses in a Superconducting NbN Film’. *Physical Review Letters* 109.18 (Oct. 2012), p. 187002. URL: <https://link.aps.org/doi/10.1103/PhysRevLett.109.187002> (cit. on p. 37).

- [65] T. Cea et al. ‘Nonlinear optical effects and third-harmonic generation in superconductors: Cooper pairs versus Higgs mode contribution’. *Physical Review B* 93.18 (May 2016), p. 180507. URL: <https://link.aps.org/doi/10.1103/PhysRevB.93.180507> (cit. on pp. 38, 44, 45, 68).
- [66] T. Cea et al. ‘Polarization dependence of the third-harmonic generation in multiband superconductors’. *Physical Review B* 97.9 (Mar. 2018), p. 094516. URL: <https://link.aps.org/doi/10.1103/PhysRevB.97.094516> (cit. on pp. 38, 68).
- [67] Y. Murotani et al. ‘Theory of light-induced resonances with collective Higgs and Leggett modes in multiband superconductors’. *Physical Review B* 95.10 (Mar. 2017), p. 104503. URL: <https://link.aps.org/doi/10.1103/PhysRevB.95.104503> (cit. on pp. 38, 68).
- [68] T. Jujo. ‘Quasiclassical Theory on Third-Harmonic Generation in Conventional Superconductors with Paramagnetic Impurities’. *Journal of the Physical Society of Japan* 87.2 (Feb. 2018), p. 024704. URL: <http://journals.jps.jp/doi/10.7566/JPSJ.87.024704> (cit. on pp. 38, 68).
- [69] X. Yang et al. ‘Lightwave-driven gapless superconductivity and forbidden quantum beats by terahertz symmetry breaking’. *Nature Photonics* 13.10 (Oct. 2019), pp. 707–713 (cit. on pp. 38, 53, 55, 68, 77, 131).
- [70] L. Schwarz et al. ‘Classification and characterization of nonequilibrium Higgs modes in unconventional superconductors’. *Nature Communications* 11.1 (Dec. 2020), p. 287. URL: <http://www.nature.com/articles/s41467-019-13763-5> (cit. on pp. 39, 40, 45, 53, 131).
- [71] Y. Barlas et al. ‘Amplitude or higgs modes in d-wave superconductors’. *Physical Review B - Condensed Matter and Materials Physics* 87.5 (Feb. 2013) (cit. on pp. 40, 53).
- [72] H. Krull et al. ‘Coupling of Higgs and Leggett modes in non-equilibrium superconductors’. *Nature Communications* 7 (June 2016) (cit. on p. 40).
- [73] K. Katsumi et al. ‘Higgs Mode in the d-Wave Superconductor Bi 2 Sr 2 CaCu 2 O 8 + x Driven by an Intense Terahertz Pulse’. *Physical Review Letters* 120.11 (Mar. 2018), p. 117001. URL: <https://link.aps.org/doi/10.1103/PhysRevLett.120.117001> (cit. on pp. 40, 45).

- [74] K. Katsumi et al. ‘Superconducting fluctuations probed by the Higgs mode in  $\text{Bi}_2\text{Sr}_2\text{CaCu}_2\text{O}_{8+x}$  thin films’. *Physical Review B* 102.5 (Aug. 2020), p. 054510. URL: <https://link.aps.org/doi/10.1103/PhysRevB.102.054510> (cit. on pp. 40, 45, 75).
- [75] F. Peronaci et al. ‘Transient Dynamics of d-Wave Superconductors after a Sudden Excitation’. *Physical Review Letters* 115.25 (Dec. 2015) (cit. on p. 43).
- [76] H. Chu et al. ‘Phase-resolved Higgs response in superconducting cuprates’. *Nature Communications* 11.1 (Dec. 2020) (cit. on pp. 44–48, 50, 52, 53, 64, 66, 72, 73, 75, 136, 137).
- [77] B. Green et al. ‘High-field high-repetition-rate sources for the coherent THz control of matter’. *Scientific Reports* 6 (2016) (cit. on pp. 44, 136).
- [78] S.-C. Lee et al. ‘Doping-dependent nonlinear Meissner effect and spontaneous currents in high-  $T_c$  superconductors’. *Physical Review B* 71.1 (Jan. 2005), p. 014507. URL: <https://link.aps.org/doi/10.1103/PhysRevB.71.014507> (cit. on p. 44).
- [79] D. I. Mircea et al. ‘Phase-sensitive harmonic measurements of microwave nonlinearities in cuprate thin films’. *Physical Review B* 80.14 (Oct. 2009), p. 144505. URL: <https://link.aps.org/doi/10.1103/PhysRevB.80.144505> (cit. on p. 44).
- [80] R. Matsunaga et al. ‘Polarization-resolved terahertz third-harmonic generation in a single-crystal superconductor  $\text{NbN}$ : Dominance of the Higgs mode beyond the BCS approximation’. *Physical Review B* 96.2 (July 2017), p. 020505. URL: <https://link.aps.org/doi/10.1103/PhysRevB.96.020505> (cit. on p. 45).
- [81] A. I. Vistnes. ‘Forced Oscillations and Resonance’. *Physics of Oscillations and Waves: With use of Matlab and Python*. Cham: Springer International Publishing, 2018, pp. 31–57. URL: [https://doi.org/10.1007/978-3-319-72314-3\\_3](https://doi.org/10.1007/978-3-319-72314-3_3) (cit. on p. 49).
- [82] B. Loret et al. ‘Intimate link between charge density wave, pseudogap and superconducting energy scales in cuprates’. *Nature Physics* 15.8 (Aug. 2019), pp. 771–775. URL: <http://www.nature.com/articles/s41567-019-0509-5> (cit. on p. 51).

- [83] R. Arpaia et al. ‘Dynamical charge density fluctuations pervading the phase diagram of a Cu-based high-  $T_c$  superconductor’. *Science* 365.6456 (Aug. 2019), pp. 906–910. URL: <https://www.sciencemag.org/lookup/doi/10.1126/science.aav1315> (cit. on p. 53).
- [84] H. F. Fong et al. ‘Polarized and unpolarized neutron-scattering study of the dynamical spin susceptibility of Y BCO’. *Physical Review B* 54.9 (Sept. 1996), pp. 6708–6720. URL: <https://link.aps.org/doi/10.1103/PhysRevB.54.6708> (cit. on p. 53).
- [85] Y. Murakami et al. ‘Multiple amplitude modes in strongly coupled phonon-mediated superconductors’. *Physical Review B* 93.9 (Mar. 2016) (cit. on pp. 53, 91, 99).
- [86] A. Bardasis et al. ‘Excitons and Plasmons in Superconductors’. *Physical Review* 121.4 (Feb. 1961), pp. 1050–1062. URL: <https://link.aps.org/doi/10.1103/PhysRev.121.1050> (cit. on p. 53).
- [87] M. A. Müller et al. ‘Collective modes in pumped unconventional superconductors with competing ground states’. *Physical Review B* 100.14 (Oct. 2019), p. 140501. URL: <https://link.aps.org/doi/10.1103/PhysRevB.100.140501> (cit. on p. 53).
- [88] L. Schwarz et al. ‘Theory of driven Higgs oscillations and third-harmonic generation in unconventional superconductors’. *Physical Review B* 101.18 (May 2020), p. 184519. URL: <https://link.aps.org/doi/10.1103/PhysRevB.101.184519> (cit. on p. 53).
- [89] L. S. Billbro et al. ‘Temporal correlations of superconductivity above the transition temperature in  $\text{La}_{2-x}\text{Sr}_x\text{CuO}_4$  probed by terahertz spectroscopy’. *Nature Physics* 7.4 (2011), pp. 298–302 (cit. on pp. 54, 72, 74).
- [90] J. Chang et al. ‘Nernst effect in the cuprate superconductor  $\text{YBa}_2\text{Cu}_3\text{O}_y$ : Broken rotational and translational symmetries’. *Physical Review B* 84.1 (July 2011), p. 014507. URL: <https://link.aps.org/doi/10.1103/PhysRevB.84.014507> (cit. on p. 54).
- [91] Y. Wang et al. ‘Nernst effect in high-  $T_c$  superconductors’. *Physical Review B* 73.2 (Jan. 2006), p. 024510. URL: <https://link.aps.org/doi/10.1103/PhysRevB.73.024510> (cit. on p. 54).

- [92] V. J. Emery et al. ‘Importance of phase fluctuations in superconductors with small superfluid density’. *Nature* 374.6521 (Mar. 1995), pp. 434–437. URL: <http://www.nature.com/articles/374434a0> (cit. on p. 55).
- [93] C. Pépin et al. ‘Fluctuations and the Higgs Mechanism in Underdoped Cuprates’. *Annual Review of Condensed Matter Physics* 11.1 (Mar. 2020), pp. 301–323. URL: <https://www.annualreviews.org/doi/10.1146/annurev-conmatphys-031218-013125> (cit. on pp. 55, 131).
- [94] G. Seibold et al. ‘Third harmonic generation from collective modes in disordered superconductors’. *Physical Review B* 103.1 (Jan. 2021) (cit. on p. 55).
- [95] H. Chu et al. ‘Fano interference of the Higgs mode in cuprate high-Tc superconductors’ (Sept. 2021). URL: <https://arxiv.org/abs/2109.09971> (cit. on p. 55).
- [96] M. Mitrano et al. ‘Possible light-induced superconductivity in K3 C60 at high temperature’. *Nature* 530.7591 (2016), pp. 461–464 (cit. on p. 55).
- [97] D. Fausti et al. ‘Light-Induced Superconductivity in a Stripe-Ordered Cuprate’. *Science* 331.6014 (Jan. 2011), pp. 189–191. URL: <https://www.sciencemag.org/lookup/doi/10.1126/science.1197294> (cit. on pp. 55, 132).
- [98] A. Jain et al. ‘Higgs mode and its decay in a two-dimensional antiferromagnet’. *Nature Physics* 13.7 (July 2017), pp. 633–637. URL: <http://www.nature.com/articles/nphys4077> (cit. on p. 55).
- [99] B. Mansart et al. ‘Coupling of a high-energy excitation to superconducting quasiparticles in a cuprate from coherent charge fluctuation spectroscopy’. *Proceedings of the National Academy of Sciences of the United States of America* 110.12 (Mar. 2013), pp. 4539–4544 (cit. on p. 55).
- [100] D. Mihailovic et al. ‘Time-Resolved Optical Studies of Quasiparticle Dynamics in High-Temperature Superconductors: Experiments and theory’ (Feb. 1999). URL: <https://arxiv.org/abs/cond-mat/9902243> (cit. on p. 57).
- [101] R. D. Averitt et al. ‘Nonequilibrium superconductivity and quasiparticle dynamics in YBa<sub>2</sub>Cu<sub>3</sub>O<sub>7-d</sub>’. *Physical Review B* 63.14 (Mar. 2001), p. 140502. URL: <https://link.aps.org/doi/10.1103/PhysRevB.63.140502> (cit. on pp. 58, 70).
- [102] R. D. Averitt et al. *Conductivity artifacts in optical-pump THz-probe measurements of YBa<sub>2</sub>Cu<sub>3</sub>O<sub>7</sub>*. Tech. rep. 2000 (cit. on pp. 58, 59).

- [103] S. Kaiser. *Light-induced superconductivity in high-T<sub>c</sub> cuprates*. Aug. 2017 (cit. on pp. 58, 64).
- [104] J. Demsar et al. ‘Superconducting Gap  $\Delta_c$ , the Pseudogap  $\Delta_p$ , and Pair Fluctuations above T<sub>c</sub> in Overdoped Y<sub>1-x</sub>Ca<sub>x</sub>Ba<sub>2</sub>Cu<sub>3</sub>O<sub>7- $\delta$</sub>  from Femto-second Time-Domain Spectroscopy’. *Physical Review Letters* 82.24 (June 1999), pp. 4918–4921. URL: <https://link.aps.org/doi/10.1103/PhysRevLett.82.4918> (cit. on p. 58).
- [105] R. A. Kaindl. ‘Ultrafast Mid-Infrared Response of YBa<sub>2</sub>Cu<sub>3</sub>O<sub>7- $\delta$</sub> ’. *Science* 287.5452 (Jan. 2000), pp. 470–473. URL: <https://www.sciencemag.org/lookup/doi/10.1126/science.287.5452.470> (cit. on pp. 58, 68, 70).
- [106] V. V. Kabanov et al. ‘Quasiparticle relaxation dynamics in superconductors with different gap structures: Theory and experiments on YBa<sub>2</sub>Cu<sub>3</sub>O<sub>7- $\delta$</sub> ’. *Physical Review B* 59.2 (Jan. 1999), pp. 1497–1506. URL: <https://link.aps.org/doi/10.1103/PhysRevB.59.1497> (cit. on p. 58).
- [107] J. P. Hinton et al. ‘The rate of quasiparticle recombination probes the onset of coherence in cuprate superconductors’. *Scientific Reports* 6.1 (Apr. 2016), p. 23610. URL: <http://www.nature.com/articles/srep23610> (cit. on p. 58).
- [108] A. Pashkin et al. ‘Femtosecond response of quasiparticles and phonons in superconducting YBa<sub>2</sub>Cu<sub>3</sub>O<sub>7- $\delta$</sub>  studied by wideband terahertz spectroscopy’. *Physical Review Letters* 105.6 (Aug. 2010) (cit. on p. 59).
- [109] L. Perfetti et al. ‘Ultrafast electron relaxation in superconducting Bi<sub>2</sub>Sr<sub>2</sub>CaCu<sub>2</sub>O<sub>8+ $\delta$</sub>  by time-resolved photoelectron spectroscopy’. *Physical Review Letters* 99.19 (Nov. 2007) (cit. on p. 60).
- [110] F. Boschini et al. ‘Collapse of superconductivity in cuprates via ultrafast quenching of phase coherence’. *Nature Materials* 17.5 (May 2018), pp. 416–420 (cit. on pp. 61, 62, 67, 68, 70, 77, 131, 142).
- [111] C. Giannetti et al. ‘Ultrafast optical spectroscopy of strongly correlated materials and high-temperature superconductors: a non-equilibrium approach’. *Advances in Physics* 65.2 (Mar. 2016), pp. 58–238 (cit. on pp. 61, 64).
- [112] T. Kondo et al. ‘Point nodes persisting far beyond T<sub>c</sub> in Bi<sub>2</sub>Tl<sub>2</sub>’. *Nature Communications* 6 (July 2015) (cit. on p. 61).

- [113] T. J. Reber et al. 'Preparing and the "filling" gap in the cuprates from the tomographic density of states'. *Physical Review B - Condensed Matter and Materials Physics* 87.6 (Feb. 2013) (cit. on p. 61).
- [114] P. Kusar et al. 'A systematic study of femtosecond quasiparticle relaxation processes in La<sub>2-x</sub>Sr<sub>x</sub>CuO<sub>4</sub>'. *Physical Review B - Condensed Matter and Materials Physics* 72.1 (2005) (cit. on pp. 63, 68).
- [115] M. Beyer et al. 'Photoinduced melting of superconductivity in the high-Tc superconductor La<sub>2-x</sub>Sr<sub>x</sub>CuO<sub>4</sub> probed by time-resolved optical and terahertz techniques'. *Physical Review B - Condensed Matter and Materials Physics* 83.21 (June 2011) (cit. on pp. 63, 66–70, 77).
- [116] J. Demsar et al. 'Pair-breaking and superconducting state recovery dynamics in [formula presented]'. *Physical Review Letters* 91.26 (2003) (cit. on pp. 63, 66).
- [117] J. Demsar. 'Non-equilibrium Phenomena in Superconductors Probed by Femtosecond Time-Domain Spectroscopy'. *Journal of Low Temperature Physics* 201.5-6 (Dec. 2020), pp. 676–709 (cit. on p. 64).
- [118] K. Terashima et al. 'Anomalous momentum dependence of the superconducting coherence peak and its relation to the pseudogap of La<sub>1.85</sub>Sr<sub>0.15</sub>CuO<sub>4</sub>'. *Physical Review Letters* 99.1 (2007), pp. 1–4 (cit. on p. 66).
- [119] C. L. Smallwood et al. 'Tracking Cooper pairs in a cuprate superconductor by ultrafast angle-resolved photoemission'. *Science* 336.6085 (2012), pp. 1137–1139 (cit. on p. 67).
- [120] W. Zhang et al. 'Stimulated emission of Cooper pairs in a high-temperature cuprate superconductor'. *Scientific Reports* 6 (July 2016) (cit. on pp. 67, 70).
- [121] C. L. Smallwood et al. 'Time- and momentum-resolved gap dynamics in Bi<sub>2</sub>Sr<sub>2</sub>CaCu<sub>2</sub>O<sub>8+δ</sub>'. *Physical Review B - Condensed Matter and Materials Physics* 89.11 (2014), pp. 1–8 (cit. on p. 67).
- [122] J. Demsar et al. 'Dynamics of photoexcited quasiparticles in heavy electron compounds'. *Journal of Physics: Condensed Matter* 18.16 (Apr. 2006), R281–R314. URL: <https://iopscience.iop.org/article/10.1088/0953-8984/18/16/R01> (cit. on p. 68).

- [123] T. Mertelj et al. ‘Quasiparticle relaxation dynamics in spin-density-wave and superconducting  $\text{SmFeAsO}_{1-x}\text{F}_x$  single crystals’. *Physical Review B* 81.22 (June 2010), p. 224504. URL: <https://link.aps.org/doi/10.1103/PhysRevB.81.224504> (cit. on p. 68).
- [124] T. Mertelj et al. ‘Normal state bottleneck and nematic fluctuations from femtosecond quasiparticle relaxation dynamics in  $\text{Sm}(\text{Fe},\text{Co})\text{AsO}$ ’. *Physical Review B* 87.17 (May 2013), p. 174525. URL: <https://link.aps.org/doi/10.1103/PhysRevB.87.174525> (cit. on p. 68).
- [125] L. Stojchevska et al. ‘Doping dependence of femtosecond quasiparticle relaxation dynamics in  $\text{Ba}(\text{Fe},\text{Co})_2\text{As}_2$  single crystals: Evidence for normal-state nematic fluctuations’. *Physical Review B* 86.2 (July 2012), p. 024519. URL: <https://link.aps.org/doi/10.1103/PhysRevB.86.024519> (cit. on p. 68).
- [126] V.V. Kabanov et al. ‘Carrier-relaxation dynamics in intragap states: The case of the superconductor  $\text{YBa}_2\text{Cu}_3\text{O}_{7-\delta}$  and the charge-density-wave semiconductor  $\text{K}_{0.3}\text{MoO}_3$ ’. *Physical Review B* 61.2 (Jan. 2000), pp. 1477–1482. URL: <https://link.aps.org/doi/10.1103/PhysRevB.61.1477> (cit. on p. 69).
- [127] A. Rothwarf et al. ‘Measurement of Recombination Lifetimes in Superconductors’. *Physical Review Letters* 19.1 (July 1967), pp. 27–30. URL: <https://link.aps.org/doi/10.1103/PhysRevLett.19.27> (cit. on p. 69).
- [128] B.I. HALPERIN et al. ‘Possible Anomalies at a Semimetal-Semiconductor Transistion’. *Reviews of Modern Physics* 40.4 (Oct. 1968) (cit. on pp. 72, 81, 84).
- [129] K. Isoyama et al. ‘Light-induced enhancement of superconductivity in iron-based superconductor  $\text{FeSe}_{0.5}\text{Te}_{0.5}$ ’. *Communications Physics* 4.1 (Dec. 2021) (cit. on p. 75).
- [130] J.P. Revelle et al. ‘Theory of Time-Resolved Optical Conductivity of Superconductors: Comparing Two Methods for Its Evaluation’. *Condensed Matter* 4.3 (Aug. 2019), p. 79 (cit. on p. 76).

- [131] A. Govorov et al. ‘Theoretical Approaches: Exciton Theory, Coulomb Interactions and Fluctuation-Dissipation Theorem’. *Understanding and Modeling Förster-type Resonance Energy Transfer (FRET): Introduction to FRET, Vol. 1*. Singapore: Springer Singapore, 2016, pp. 41–51. URL: [https://doi.org/10.1007/978-981-287-378-1\\_5](https://doi.org/10.1007/978-981-287-378-1_5) (cit. on p. 81).
- [132] J. Frenkel. ‘On the Transformation of light into Heat in Solids. I’. *Physical Review* 37.1 (Jan. 1931), pp. 17–44. URL: <https://link.aps.org/doi/10.1103/PhysRev.37.17> (cit. on p. 81).
- [133] G. H. Wannier. ‘The Structure of Electronic Excitation Levels in Insulating Crystals’. *Physical Review* 52.3 (Aug. 1937), pp. 191–197. URL: <https://link.aps.org/doi/10.1103/PhysRev.52.191> (cit. on p. 81).
- [134] J. D. Wright. *Molecular Crystals*. 2nd ed. Cambridge University Press, 1995, p. 108 (cit. on p. 81).
- [135] G. Lanzani. *The Photophysics Behind Photovoltaics and Photonics*. Wiley-VCH Verlag., 2012, p. 82 (cit. on p. 81).
- [136] K. Seki et al. ‘Excitonic Bose-Einstein condensation in Ta<sub>2</sub>NiSe<sub>5</sub> above room temperature’. *Physical Review B - Condensed Matter and Materials Physics* 90.15 (2014), pp. 1–7 (cit. on pp. 82, 90, 109, 118, 132).
- [137] L. V. Keldysh et al. ‘Collective Properties of Excitons in Semiconductors’. *Soviet Journal of Experimental and Theoretical Physics* 27 (Sept. 1968), p. 521 (cit. on pp. 81, 83).
- [138] R. S. Knox. ‘Introduction to Exciton Physics’. *Collective Excitations in Solids*. Ed. by B. Di Bartolo. Boston, MA: Springer US, 1983, pp. 183–245. URL: [https://doi.org/10.1007/978-1-4684-8878-4\\_5](https://doi.org/10.1007/978-1-4684-8878-4_5) (cit. on p. 83).
- [139] J. Zittartz. ‘Anisotropy Effects in the Excitonic Insulator’. *Physical Review* 162.3 (Oct. 1967) (cit. on p. 83).
- [140] J. Zittartz. ‘Transport Properties of the "Excitonic Insulator": Electrical Conductivity’. *Physical Review* 165.2 (Jan. 1968) (cit. on p. 83).
- [141] F. X. Bronold et al. ‘Possibility of an excitonic insulator at the semiconductor-semimetal transition’. *Physical Review B - Condensed Matter and Materials Physics* 74.16 (2006) (cit. on pp. 83, 84).

- [142] B. Zenker et al. 'Fate of the excitonic insulator in the presence of phonons'. *Physical Review B* 90.19 (Nov. 2014), p. 195118. URL: <https://link.aps.org/doi/10.1103/PhysRevB.90.195118> (cit. on pp. 83, 84).
- [143] A. Einstein. 'Sitzungsber'. *Preuss. Akad. Wiss.* 1 (1925), p. 3 (cit. on pp. 83, 84).
- [144] L. TISZA. 'Transport Phenomena in Helium II'. *Nature* 141.3577 (May 1938) (cit. on p. 84).
- [145] F. London. 'On the Bose-Einstein Condensation'. *Physical Review* 54.11 (Dec. 1938), pp. 947–954. URL: <https://link.aps.org/doi/10.1103/PhysRev.54.947> (cit. on p. 84).
- [146] C. C. Homes et al. 'Sum rules and energy scales in the high-temperature superconductor  $\text{YBa}_2\text{Cu}_3\text{O}_{6+x}$ '. *Physical Review B - Condensed Matter and Materials Physics* 69.2 (2004), pp. 1–9 (cit. on p. 85).
- [147] T. I. Larkin et al. 'Giant exciton Fano resonance in quasi-one-dimensional  $\text{Ta}_2\text{NiSe}_5$ '. *Physical Review B* 95.19 (May 2017) (cit. on pp. 84, 85, 92, 111, 113, 117, 127, 132, 133).
- [148] Y. F. Lu et al. 'Zero-gap semiconductor to excitonic insulator transition in  $\text{Ta}_2\text{NiSe}_5$ '. *Nature Communications* 8 (Feb. 2017) (cit. on pp. 84, 85, 89, 91, 92, 100, 107, 116, 132, 136).
- [149] B. Bucher et al. *Kxcitonic Insulator Phase in  $\text{TmSeO}_4$* . Tech. rep. 1991 (cit. on p. 86).
- [150] F. J. Di Salvo et al. 'Electronic properties and superlattice formation in the semimetal  $\text{TiSe}_2$ '. *Physical Review B* 14.10 (Nov. 1976), pp. 4321–4328. URL: <https://link.aps.org/doi/10.1103/PhysRevB.14.4321> (cit. on p. 86).
- [151] A. Kozlov et al. 'Possibility of super-thermal conductivity in semiconductors' (1966) (cit. on p. 86).
- [152] J. Neuenschwander et al. 'Pressure-driven semiconductor-metal transition in intermediate-valence  $\text{TmSe}_{1-x}\text{Te}_x$  and the concept of an excitonic insulator'. *Physical Review B* 41.18 (1990), pp. 12693–12709 (cit. on p. 86).

- [153] Y. E. Lozovik et al. 'Feasibility of superfluidity of paired spatially separated electrons and holes; a new superconductivity mechanism'. *JETP Lett. (USSR) (Engl. Transl.); (United States)* (). URL: <https://www.osti.gov/biblio/7285279> (cit. on p. 86).
- [154] L. V. Butov et al. 'Towards Bose-Einstein condensation of excitons in potential traps'. *Nature* 417.6884 (2002), pp. 47–52 (cit. on p. 86).
- [155] A. A. High et al. 'Spontaneous coherence in a cold exciton gas'. *Nature* 483.7391 (2012), pp. 584–588. URL: <http://dx.doi.org/10.1038/nature10903> (cit. on p. 86).
- [156] R. Anankine et al. 'Quantized Vortices and Four-Component Superfluidity of Semiconductor Excitons'. *Physical Review Letters* 118.12 (2017), pp. 1–5 (cit. on p. 86).
- [157] T. Pillo et al. 'Photoemission of bands above the Fermi level: The excitonic insulator phase transition'. *Physical Review B - Condensed Matter and Materials Physics* 61.23 (2000), pp. 16213–16222 (cit. on p. 87).
- [158] H. Cercellier et al. 'Evidence for an excitonic insulator phase in 1T-TiSe<sub>2</sub>'. *Physical Review Letters* 99.14 (2007), pp. 1–4 (cit. on p. 87).
- [159] R. H. Friend et al. *Semimetallic character of TiSe<sub>2</sub> and semiconductor character of TiS<sub>2</sub> under pressure Related content High-pressure transport properties of TiS<sub>2</sub> and TiSe<sub>2</sub>*. Tech. rep. (cit. on p. 86).
- [160] J. A. Wilson. 'Concerning the semimetallic characters of TiS<sub>2</sub> and TiSe<sub>2</sub>'. *Solid State Communications* 22.9 (1977), pp. 551–553 (cit. on pp. 86, 88).
- [161] C. Monney et al. 'Probing the exciton condensate phase in 1T-TiSe<sub>2</sub> with photoemission'. *New Journal of Physics* 12 (2010) (cit. on p. 87).
- [162] C. Monney et al. 'Spontaneous exciton condensation in 1T-TiSe<sub>2</sub>: BCS-like approach'. *Physical Review B - Condensed Matter and Materials Physics* 79.4 (2009), pp. 1–11 (cit. on p. 88).
- [163] H. P. Hughes. 'Structural distortion in TiSe<sub>2</sub> and related materials—a possible Jahn-Teller effect?' *Journal of Physics C: Solid State Physics* 10.11 (June 1977), pp. L319–L323. URL: <https://iopscience.iop.org/article/10.1088/0022-3719/10/11/009> (cit. on p. 88).

- [164] C. Monney et al. ‘Revealing the role of electrons and phonons in the ultrafast recovery of charge density wave correlations in 1T- TiSe 2’. *Physical Review B* 94.16 (2016), pp. 1–9 (cit. on p. 88).
- [165] A. Kogar et al. ‘Signatures of exciton condensation in a transition metal dichalcogenide’. *Science* 358.6368 (Dec. 2017), pp. 1314–1317. URL: <https://www.sciencemag.org/lookup/doi/10.1126/science.aam6432> (cit. on p. 88).
- [166] M. Porer et al. ‘Non-thermal separation of electronic and structural orders in a persisting charge density wave’. *Nature Materials* 13.9 (2014), pp. 857–861 (cit. on pp. 88, 94).
- [167] Q.M. Liu et al. ‘Photoinduced multistage phase transitions in Ta<sub>2</sub>NiSe<sub>5</sub>’. *Nature Communications* 12.1 (2021), pp. 1–8 (cit. on p. 89).
- [168] T. Kaneko et al. ‘Orthorhombic-to-monoclinic phase transition of Ta<sub>2</sub> NiSe<sub>5</sub> induced by the Bose-Einstein condensation of excitons’. *Physical Review B* 87.3 (Jan. 2013), p. 035121. URL: <https://link.aps.org/doi/10.1103/PhysRevB.87.035121> (cit. on pp. 89–91, 99).
- [169] M. Greenblatt. ‘Molybdenum oxide bronzes with quasi-low-dimensional properties’. *Chemical Reviews* 88.1 (May 2002), pp. 31–53. URL: <https://pubs.acs.org/sharingguidelines> (cit. on p. 89).
- [170] Y. Wakisaka et al. ‘Excitonic Insulator State in Ta<sub>2</sub> NiSe<sub>5</sub> Probed by Photoemission Spectroscopy’. *Physical Review Letters* 103.2 (July 2009), p. 026402. URL: <https://link.aps.org/doi/10.1103/PhysRevLett.103.026402> (cit. on pp. 89, 118, 132).
- [171] S. Kaiser et al. ‘Ultrafast dynamics and coherent order parameter oscillations under photo-excitation in the excitonic insulator Ta<sub>2</sub>NiSe<sub>5</sub>’. *SPIE-Intl Soc Optical Eng*, May 2018, p. 2 (cit. on p. 90).
- [172] K. Sugimoto et al. ‘Strong Coupling Nature of the Excitonic Insulator State in Ta<sub>2</sub>NiSe<sub>5</sub>’. *Physical Review Letters* 120.24 (2018), p. 247602. URL: <https://doi.org/10.1103/PhysRevLett.120.247602> (cit. on pp. 91, 99, 132).
- [173] A. Nakano et al. ‘Antiferroelectric distortion with anomalous phonon softening in the excitonic insulator Ta<sub>2</sub>NiSe<sub>5</sub>’. *Physical Review B* 98.4 (2018), pp. 1–6 (cit. on pp. 93, 94, 100, 106, 132).

- [174] A. Subedi. ‘Orthorhombic-to-monoclinic transition in Ta<sub>2</sub>NiSe<sub>5</sub> due to a zone-center optical phonon instability’. *Physical Review Materials* 4.8 (Aug. 2020) (cit. on pp. 94, 100, 106, 110).
- [175] S. Hellmann et al. ‘Time-domain classification of charge-density-wave insulators’. *Nature Communications* 3 (2012) (cit. on p. 94).
- [176] T. Rohwer et al. ‘Collapse of long-range charge order tracked by time-resolved photoemission at high momenta’. *Nature* 471.7339 (Mar. 2011), pp. 490–493. URL: <http://www.nature.com/articles/nature09829> (cit. on pp. 94, 98, 127).
- [177] J.C. Petersen et al. ‘Clocking the Melting Transition of Charge and Lattice Order in 1 T TaS<sub>2</sub> with Ultrafast Extreme-Ultraviolet Angle-Resolved Photoemission Spectroscopy’. *Physical Review Letters* 107.17 (Oct. 2011), p. 177402. URL: <https://link.aps.org/doi/10.1103/PhysRevLett.107.177402> (cit. on pp. 94, 98).
- [178] M. Eichberger et al. ‘Snapshots of cooperative atomic motions in the optical suppression of charge density waves’. *Nature* 468.7325 (2010), pp. 799–802 (cit. on p. 94).
- [179] K. Okazaki et al. ‘Photo-induced semimetallic states realised in electron-hole coupled insulators’. *Nature Communications* 9.1 (Dec. 2018) (cit. on pp. 94, 95, 98, 117, 119, 120, 127).
- [180] S. Mor et al. ‘Inhibition of the photoinduced structural phase transition in the excitonic insulator Ta<sub>2</sub>NiSe<sub>5</sub>’. *Physical Review B* 97.11 (Mar. 2018) (cit. on pp. 94, 97).
- [181] S. Mor et al. ‘Ultrafast Electronic Band Gap Control in an Excitonic Insulator’. *Physical Review Letters* 119.8 (Aug. 2017) (cit. on pp. 94, 98, 117, 119, 120).
- [182] T. Tang et al. ‘Non-Coulomb strong electron-hole binding in Ta<sub>2</sub>NiSe<sub>5</sub> revealed by time- and angle-resolved photoemission spectroscopy’ (Mar. 2020). URL: <http://arxiv.org/abs/2003.00514><http://dx.doi.org/10.1103/PhysRevB.101.235148> (cit. on pp. 94, 97, 98, 117, 119).
- [183] H. M. Bretscher et al. ‘Ultrafast melting and recovery of collective order in the excitonic insulator Ta<sub>2</sub>NiSe<sub>5</sub>’. *Nature Communications* 12.1 (2021), pp. 1–8. URL: <http://dx.doi.org/10.1038/s41467-021-21929-3> (cit. on pp. 97, 111, 133).

- [184] E. Baldini et al. ‘The spontaneous symmetry breaking in Ta<sub>2</sub>NiSe<sub>5</sub> is structural in nature’ (July 2020). URL: <http://arxiv.org/abs/2007.02909> (cit. on pp. 97, 98, 111, 117, 127, 133).
- [185] K. Fukutani et al. ‘Detecting photoelectrons from spontaneously formed excitons’. *Nature Physics* 17.9 (2021), pp. 1024–1030. URL: <http://dx.doi.org/10.1038/s41567-021-01289-x> (cit. on pp. 97, 113, 114, 127, 132).
- [186] D. Golež et al. ‘Photoinduced gap closure in an excitonic insulator’. *Physical Review B* 94.3 (July 2016), p. 035121. URL: <https://link.aps.org/doi/10.1103/PhysRevB.94.035121> (cit. on p. 98).
- [187] Y. Murakami et al. ‘Photoinduced Enhancement of Excitonic Order’. *Physical Review Letters* 119.24 (Dec. 2017), p. 247601. URL: <https://link.aps.org/doi/10.1103/PhysRevLett.119.247601> (cit. on p. 98).
- [188] D. Werdehausen et al. ‘Photo-excited dynamics in the excitonic insulator Ta<sub>2</sub>NiSe<sub>5</sub>’. *Journal of Physics Condensed Matter* 30.30 (2018) (cit. on p. 98).
- [189] G. Mazza et al. ‘Nature of Symmetry Breaking at the Excitonic Insulator Transition: Ta<sub>2</sub>NiSe<sub>5</sub>’. *Physical Review Letters* 124.19 (May 2020) (cit. on pp. 100, 132).
- [190] M. D. Watson et al. ‘Band hybridization at the semimetal-semiconductor transition of Ta<sub>2</sub>NiSe<sub>5</sub> enabled by mirror-symmetry breaking’. *Physical Review Research* 2.1 (Mar. 2020) (cit. on pp. 100, 111).
- [191] M.-J. Kim et al. ‘Phononic soft mode behavior and a strong electronic background across the structural phase transition in the excitonic insulator Ta<sub>2</sub>NiSe<sub>5</sub>’. *Physical Review Research* 2.4 (2020), p. 42039. URL: <https://doi.org/10.1103/PhysRevResearch.2.042039> (cit. on pp. 100, 122).
- [192] S. Y. Kim et al. ‘Layer-Confined Excitonic Insulating Phase in Ultrathin Ta<sub>2</sub>NiSe<sub>5</sub> Crystals’. *ACS Nano* 10.9 (2016), pp. 8888–8894 (cit. on p. 100).
- [193] J. Yan et al. ‘Strong Electron-Phonon Coupling in the Excitonic Insulator Ta<sub>2</sub>NiSe<sub>5</sub>’. *Inorganic Chemistry* 58.14 (2019), pp. 9036–9042 (cit. on pp. 100, 102, 126).

- [194] K. Kim et al. ‘Direct observation of excitonic instability in Ta<sub>2</sub>NiSe<sub>5</sub>’. *Nature Communications* 12.1 (2021), pp. 1–8 (cit. on pp. 105, 107, 111, 117, 122, 133).
- [195] P. A. Volkov et al. ‘Critical charge fluctuations and emergent coherence in a strongly correlated excitonic insulator’. *npj Quantum Materials* 6.1 (2021), pp. 1–9. URL: <http://dx.doi.org/10.1038/s41535-021-00351-4> (cit. on pp. 105, 107, 111, 117, 122, 127, 133).
- [196] T. I. Larkin et al. ‘Infrared phonon spectra of quasi-one-dimensional TaNiSe<sub>5</sub> and Ta<sub>2</sub>Ni<sub>5</sub>S<sub>5</sub>’. *Physical Review B* 98.12 (2018), pp. 1–9 (cit. on pp. 111, 113, 127, 132, 133).
- [197] S. Hunsche et al. ‘Impulsive softening of coherent phonons in tellurium’. *Physical Review Letters* 75.9 (1995), pp. 1815–1818 (cit. on p. 117).
- [198] M. D. Watson et al. ‘Band hybridization at the semimetal-semiconductor transition of Ta<sub>2</sub>NiSe<sub>5</sub> enabled by mirror-symmetry breaking’. *Physical Review Research* 2.1 (Mar. 2020), p. 013236. URL: <https://link.aps.org/doi/10.1103/PhysRevResearch.2.013236> (cit. on pp. 118, 132, 133).
- [199] K. M. Shen et al. ‘Missing quasiparticles and the chemical potential puzzle in the doping evolution of the cuprate superconductors’. *Physical Review Letters* 93.26 (2004) (cit. on p. 120).
- [200] K. Reimann. ‘Table-top sources of ultrashort THz pulses’. *Reports on Progress in Physics* 70.10 (Oct. 2007), pp. 1597–1632. URL: <https://iopscience.iop.org/article/10.1088/0034-4885/70/10/R02> (cit. on p. 126).
- [201] M. C. Hoffmann et al. ‘Intense ultrashort terahertz pulses: generation and applications’. *Journal of Physics D: Applied Physics* 44.8 (Mar. 2011), p. 083001. URL: <https://iopscience.iop.org/article/10.1088/0022-3727/44/8/083001> (cit. on p. 126).
- [202] P. Gu et al. ‘Study of terahertz radiation from InAs and InSb’. *Journal of Applied Physics* 91.9 (May 2002), pp. 5533–5537. URL: <http://aip.scitation.org/doi/10.1063/1.1465507> (cit. on p. 126).
- [203] M. B. Johnston et al. ‘Simulation of terahertz generation at semiconductor surfaces’. *Physical Review B* 65.16 (Mar. 2002), p. 165301. URL: <https://link.aps.org/doi/10.1103/PhysRevB.65.165301> (cit. on p. 126).

- [204] G. Klatt et al. ‘Terahertz emission from lateral photo-Dember currents’. *Optics Express* 18.5 (Mar. 2010), p. 4939. URL: <https://www.osapublishing.org/oe/abstract.cfm?uri=oe-18-5-4939> (cit. on p. 126).
- [205] H. Arima et al. ‘High-Pressure Hall Effect Measurement on Ta<sub>2</sub>NiSe<sub>5</sub> as a Candidate for Excitonic Insulator’. *Proceedings of the International Conference on Strongly Correlated Electron Systems (SCES2019)*. Journal of the Physical Society of Japan, Mar. 2020. URL: <https://journals.jps.jp/doi/10.7566/JPSJP.30.011031> (cit. on p. 126).
- [206] M. H. Hecht. ‘Role of photocurrent in low-temperature photoemission studies of Schottky-barrier formation’. *Physical Review B* 41.11 (Apr. 1990), pp. 7918–7921. URL: <https://link.aps.org/doi/10.1103/PhysRevB.41.7918> (cit. on p. 126).
- [207] L. B. Tan et al. ‘Interacting Polaron-Polaritons’. *Physical Review X* 10.2 (June 2020) (cit. on p. 127).
- [208] Z. A. Xu et al. ‘Vortex-like excitations and the onset of superconducting phase fluctuation in underdoped La<sub>2-x</sub>Sr<sub>x</sub>CuO<sub>4</sub>’. *Nature* 406.6795 (Aug. 2000), pp. 486–488. URL: <http://www.nature.com/articles/35020016> (cit. on p. 131).
- [209] B. Liu et al. ‘Pump Frequency Resonances for Light-Induced Incipient Superconductivity in YBa<sub>2</sub>Cu<sub>3</sub>O<sub>6.5</sub>’. *Physical Review X* 10.1 (Mar. 2020), p. 011053. URL: <https://link.aps.org/doi/10.1103/PhysRevX.10.011053> (cit. on p. 132).
- [210] S. Kaiser et al. ‘Optically induced coherent transport far above T<sub>c</sub> in underdoped YBa<sub>2</sub>Cu<sub>3</sub>O<sub>6+δ</sub>’. *Physical Review B* 89.18 (May 2014), p. 184516. URL: <https://link.aps.org/doi/10.1103/PhysRevB.89.184516> (cit. on p. 132).
- [211] S. Kovalev et al. ‘Probing ultra-fast processes with high dynamic range at 4th-generation light sources: Arrival time and intensity binning at unprecedented repetition rates’. *Structural Dynamics* 4.2 (Mar. 2017), p. 024301. URL: <http://aca.scitation.org/doi/10.1063/1.4978042> (cit. on p. 137).
- [212] H. Hirori et al. ‘Single-cycle terahertz pulses with amplitudes exceeding 1 MV/cm generated by optical rectification in LiNbO<sub>3</sub>’. *Applied Physics Letters* 98.9 (Feb. 2011), p. 091106. URL: <http://aip.scitation.org/doi/10.1063/1.3560062> (cit. on p. 137).

- [213] K.-L. Yeh et al. ‘Generation of  $10\mu\text{J}$  ultrashort terahertz pulses by optical rectification’. *Applied Physics Letters* 90.17 (Apr. 2007), p. 171121. URL: <http://aip.scitation.org/doi/10.1063/1.2734374> (cit. on p. 137).
- [214] T. Kampfrath et al. ‘Resonant and nonresonant control over matter and light by intense terahertz transients’. *Nature Photonics* 7.9 (Sept. 2013), pp. 680–690. URL: <http://www.nature.com/articles/nphoton.2013.184> (cit. on p. 137).



# LIST OF FIGURES

0.1. The Higgs oscillations excited in a superconductor . . . . .	15
1.1. Mexican hat potential . . . . .	22
1.2. A schematic fluctuation spectrum of SSB state . . . . .	25
1.3. Anderson's pseudospin model and simulation with Bloch equation . . . . .	29
1.4. Raman spectra in $E_{2g}$ symmetry of 2H-NbSe <sub>2</sub> measured at various temperatures and pressures . . . . .	32
1.5. Excitation mechanisms for coherent phonons . . . . .	33
1.6. The schematic of the Higgs mode excitation and the resulted oscillation of quasiparticles in NbN induced by a monocycle THz pump . . . . .	34
1.7. Forced Higgs oscillation and third harmonic generation from a superconducting NbN film under the multicycle THz pump . . . . .	36
1.8. Third harmonic generation in THz transmission spectroscopy . . . . .	38
1.9. The sketch of superconducting order parameter symmetry . . . . .	39
1.10. Illustration of $d$ -wave condensate oscillation symmetries . . . . .	39
1.11. THz pump-optical probe measurement of the cuprate superconductor . . . . .	40
2.1. TH from driven Higgs oscillation in LSCO(OP45) . . . . .	45

2.2. Signature of the driven Higgs oscillations in transient response and polarization dependence . . . . .	46
2.3. Temperature dependence of TH intensity ( $I_{TH}$ ) and relative phase ( $\phi_{TH}$ ) from optimally-doped cuprates . . . . .	47
2.4. Temperature dependence of transmitted $I_{TH}$ . . . . .	47
2.5. Temperature dependence of $I_{TH}/I_{FH}^3$ . . . . .	48
2.6. The amplitude and the phase of a forced oscillation of a harmonic oscillator . . . . .	49
2.7. Procedure for extracting the relative phase between TH response and FH drive . . . . .	50
2.8. Driven coupled oscillators model and finite TH above $T_c$ . . . . .	52
2.9. Anderson-pseudospin model of $d$ -wave superconductor . . . . .	53
2.10. Phase diagram of cuprate superconductors . . . . .	54
3.1. Schematic representation of ultrafast nonequilibrium process in a superconductor . . . . .	58
3.2. Transient THz optical conductivity of underdoped YBCO . . . . .	58
3.3. Transient apex oxygen mode at 17.2 THz of optimally doped YBCO . . . . .	59
3.4. TrARPES experiment for cuprate superconductor . . . . .	60
3.5. Different processes governing the excitation dynamics of photo-excited quasiparticles in superconductor. . . . .	61
3.6. Temporal evolution of the spectral function of underdoped Bi2212 . . . . .	62
3.7. Photoinduced dynamics of LSCO via linear optical probes . . . . .	63
3.8. Photoinduced dynamics of LSCO via nonlinear THz probe . . . . .	65
3.9. 1D pump scans of TH field of LSCO . . . . .	67
3.10. Evolution of the TH changes in LSCO . . . . .	69
3.11. THz fluence dependent TH dynamics under the photoexcitation . . . . .	71
3.12. Transient dynamics of transmitted THz field through LSCO thin film in 2D plot . . . . .	73
3.13. Evolution of photoexcited interference in LSCO . . . . .	75
3.14. Transient and normalized TH dynamics by linear THz response . . . . .	76

4.1. Schematic of various types of exciton and corresponding simple band structure . . . . .	80
4.2. Schematic of the transition into the excitonic insulator . . . . .	82
4.3. The real part of the optical conductivity calculated for the superconductor and excitonic insulator. . . . .	85
4.4. Anomalous resistivity of excitonic insulator candidates . . . . .	86
4.5. Occurrence of an excitonic insulator phase in $1T$ -TiSe <sub>2</sub> . . . . .	87
4.6. Crystal structure and phase transition of Ta <sub>2</sub> NiSe <sub>5</sub> . . . . .	89
4.7. A characteristic flat band dispersion . . . . .	90
4.8. Charge-transfer exciton in Ta <sub>2</sub> NiSe <sub>5</sub> . . . . .	90
4.9. Phase diagram of the excitonic insulator phase in Ta <sub>2</sub> NiSe <sub>5</sub> mapping $T_c$ as a function of the gap state. . . . .	91
4.10. Optical conductivity and Giant Fano shape in Ta <sub>2</sub> NiSe <sub>5</sub> . . . . .	92
4.11. inelastic x-ray scattering measurements in Ta <sub>2</sub> NiSe <sub>5</sub> . . . . .	93
4.12. tr-ARPES spectra of Ta <sub>2</sub> NiSe <sub>5</sub> . . . . .	95
4.13. NIR pump-probe measurement in Ta <sub>2</sub> NiSe <sub>5</sub> . . . . .	96
4.14. The gap response of Ta <sub>2</sub> NiSe <sub>5</sub> . . . . .	97
5.1. Raman spectra of Ta <sub>2</sub> NiSe <sub>5</sub> . . . . .	101
5.2. $36\text{cm}_1$ mode in Ta <sub>2</sub> NiSe <sub>5</sub> . . . . .	101
5.3. Polarized Raman spectra of Ta <sub>2</sub> NiSe <sub>5</sub> . . . . .	103
5.4. Temperature-dependent Raman spectra in the (XZ) geometry	103
5.5. Gaussian fit analysis of the low energy Raman spectra . . . . .	105
5.6. Laser dependent low frequency Raman dynamics of Ta <sub>2</sub> NiSe <sub>5</sub>	107
5.7. Fano fit analysis of the low energy Raman spectra . . . . .	108
5.8. Sketch of the dynamics driving the semiconductor-excitonic insulator phase transition in Ta <sub>2</sub> NiSe <sub>5</sub> . . . . .	110
6.1. Dynamics of the photo-induced change in reflectivity $\Delta R/R$ in Ta <sub>2</sub> NiSe <sub>5</sub> . . . . .	115
6.2. Time-resolved transient population of the valence band at $\Gamma$ .	118
6.3. Ultrafast upper VB changes at $\Gamma$ . . . . .	119

6.4. Time evolution of EDC spectra at the upper VB with two peaks fit . . . . .	121
6.5. Time-resolved transient population of the VB at $\Gamma$ . . . . .	122
6.6. Photoinduced change in the transmitted THz electric field in $\text{Ta}_2\text{NiSe}_5$ . . . . .	124
6.7. Photoinduced change in the reflected THz electric field in $\text{Ta}_2\text{NiSe}_5$ . . . . .	125
6.8. Schematic of the coherent current emergence from the polaronic complexes under photoexcitation . . . . .	126
A.1. Experimental determination of $T_c$ in cuprates . . . . .	136
A.2. Schematic illustration of the THz-drive third harmonic (TH) generation. . . . .	137
A.3. Experimental scheme for the optical pump-TH drive measurements . . . . .	138
A.4. 2D plot of the observed THz waveforms in the $(\Delta t, t_E)$ plane. . . . .	139
A.5. Raman spectra with a reference sample . . . . .	140
A.6. A scheme of Pump-probe experimental setup . . . . .	141
A.7. Transient reflectivity change in $\text{Ta}_2\text{NiSe}_5$ . . . . .	141
A.8. Illustration of trARPES . . . . .	142
A.9. Experimental scheme for the optical pump-TH probe measurement . . . . .	144

# DECLARATION OF AUTHORSHIP

I hereby certify that I am the sole author of this thesis entitled “Collective excitations and order parameter dynamics in quantum materials” and that I have not used any sources other than those listed in the bibliography and identified as references. I further declare that I have not submitted this thesis at any other institution in order to obtain a degree.

Min-Jae Kim

Stuttgart, November 30th, 2021



# ACKNOWLEDGEMENTS

My interest in the Universe in my childhood brings me up as a Ph.D. student in physics. I am so pleased that I could have experienced science research in my life. During this work, I met many people who supported me inside and also outside of science.

I would like first to thank my supervisor, Prof. Dr. Stefan Kaiser for the opportunity to work in his group at the Max Planck Institute for Solid State Research in Stuttgart. Even though i had no experience in optics, he trusted in me and my capabilities as an experimentalist. I have formulated all the steps of research from him with his invaluable expertise. I also highly appreciate the exciting research topics he introduced to me and all the support I received. Literally, he was a perfect supervisor for me.

I would like to thank Prof. Dr. Harald Giessen, who accepted me to enroll as a Ph.D. student at Universität Stuttgart. I highly appreciated many possibilities in optics with many experts in his group, including attending group workshops. I am also thankful to Dr. Christina Rekowski for her administrative support.

I was fortunate to have had the opportunity to work at both MPI and Uni Stuttgart with all its possibilities, ranging from the close connection to experimental and theory groups, many inter-seminars, conferences, and summer schools.

I would like to acknowledge Prof. Dr. Bernhard Keimer, Dr. Gennady Logvenov, Dr. Georg Christiani, Gideok Kim, David Dawson, and Daniel Putzky for cooperative research on cuprate superconductors with their invaluable scientific expertise.

I would like to acknowledge Prof. Dr. Hidenori Takagi and Dr. Masahiko Isobe for their all support in studying the excitonic insulator.

I want to thank Armin Shulz for his crucial experimental support for Raman spectroscopy.

I also would like to acknowledge our theory collaborators Prof. Dr. Dirk Manske and his group members Lukas Schwarz, Rafael Hänel. I enjoyed a lot of discussions with them in special group meetings about Higgs physics. Especially, I thank to Rafael for helping me to structure the knowledge of Higgs theory and for proofreading of the Higgs part.

I also had great opportunities to collaborate inside and outside of Germany. I would like to thank Prof. Dr. Michael Gensch, Dr. Sergey Kovalev and all the members of TELBE-Helmholz Zentrum Dresden, Dr. Jan-Christoph Deinert, Dr. Zhe Wang, Nilesh Awari, Min Chen. Most of my beam time work was done with them. Without this team, I could not accomplish half of this thesis. I am so pleased that I could work with them.

I would like to thank Prof. Dr. Andrea Damascelli and David Jones from the University British Columbia and their group members Dr. Sergey Zhdanovich, Dr. Fabio Boschini, Sydney Dufresne, Dr. Giorgio Levy, Dr. Evgeny Ostroumov, and MengXing Na for their all support for excitonic insulator study using time-resolved ARPES experiments and life in Vancouver as well. I am pleased that I had unforgettable memories working at UBC.

I would like to acknowledge Prof. Dr. Shimano and his group member Kota Katsumi. Their scientific experties on Higgs physics inspired me a lot during the collaborating work in Dresden and also at the UBC conference as well.

I would like to acknowledge my colleagues who spent almost all of my Ph.D. time. They are not only colleagues but, most importantly, people who shared a friendly relationship. In ultrafast spectroscopy group of MPI, Parmida Shabestari, Gelon Albrecht, Daniel Werdehausen, Steinn Ymir Agusts-

son, Amrit Pokharel, Desislava Daskalova, Syndey Seraphim, Kedar Eshwar Honasoge, Hao Chu, Le Phuong Hoang, Liwen Feng, Tim Prissnitz. I would especially like to thank Parmida who introduced me whole optical techniques at the beginning of my Ph.D. in this group. Because of her, I could really enjoy daily life in the office with a lot of laughing. I would like to particularly thank my current colleagues Liwen and Tim. They got through all the Corona situation with me. I was always relieved to work with them. More specially, I want to give deeply thank Tim for his time spending on proofreading and translating to German for Zusammenfassung of my thesis.

I would like to thank my external supervisor Dr. Rotraut Merkle for her warm advices and encouragements during my study.

I would like to thank people out of my group as well. Padma, she went through the same time of Ph.D. as me. Whenever we met, we could relate to each other and that makes me always encouraged. Also, I can not miss Korean colleagues in MPI Stuttgart. We had a lot of funny moments and supported each other when we faced any problem. I was happy to meet them in Germany and look forward to continuing the relationship.

I would like to leave special thanks to Soka family and my mentor Daisaku Ikeda. I have been encouraged my whole life by them. Daisaku Ikeda is my eternal mentor who continuously trusts in me and hopes for my happiness. During my Ph.D., I have learned the Nichiren Philosophy intensively as well for seeking real happiness. Thanks to this training, i could decide to live for other's happiness, that is for my happiness in the end.

Finally, I would like to thank my family. I deeply thank my parents for giving me this invaluable life and being the ones I can always lean on. Also, I thank my parents-in-law for their all support and warm hearts. I thank my siblings for loving me. For the last, I would say thank you, my best friend and husband Hyungyu for all his encouragement and support, and love.

I might be slow, but I did it. From now on, I look forward to go to the next stage of my life. Whenever, wherever I will be, I will create value and be happy.

Thanks all.



The format of this thesis manuscript is based on a LATEX template offered by and distributed under a MIT License (MIT) Copyright (c) 2013 Tammo van Lessen and others.